12-2012

ALTERNATIVE ENERGY SOURCES - INTEGRATION OF POWER GENERATION SYSTEMS INTO A MICROGRID AT CLEMSON UNIVERSITY AND AN ATMOSPHERIC THERMODYNAMIC DRIVEN MECHANICAL CLOCK

Shreyas Patel
Clemson University, smpatel@g.clemson.edu

ALTERNATIVE ENERGY SOURCES – INTEGRATION OF POWER GENERATION
SYSTEMS INTO A MICROGRID AT CLEMSON UNIVERSITY AND AN
ATMOSPHERIC THERMODYNAMIC DRIVEN MECHANICAL CLOCK

A Thesis
Presented to
the Graduate School of
Clemson University

In Partial Fulfillment
of the Requirements for the Degree
Master of Science
Mechanical Engineering

---

by
Shreyas Mohanbhai Patel
December 2012

Accepted by:
Dr. John Wagner, Committee Chair
Dr. Charles Gooding
Dr. Todd Schweisinger
Dr. Yue Wang

ABSTRACT

Non-renewable energy sources such as coal, crude oil, and natural gas are being consumed at a brisk pace which is promoting a worldwide energy crisis. The burning of fossil fuels produces greenhouse gases such as carbon dioxide and nitrous oxides as well as soot which contribute to atmospheric pollution. Although fossil fuels will continue to be available for many decades, the amount of petroleum remaining in the earth and its associated cost remains an open issue. The utilization of green energy such as solar and wind offer renewable and pollution free sources. A worldwide shift is slowly underway towards the inclusion of renewable energy sources to generate electrical and mechanical power. To meet this emerging societal demand, research into alternative energy sources such as solar, wind, and thermodynamic power generation is underway at Clemson University.

This research encompasses two renewable energy strategies: a solar-based electrical microgrid, and an atmospheric thermodynamic driven mechanical clock. The concept of an electrical microgrid at Clemson University has been investigated as it promotes a renewable energy source to help realize a "net zero" campus. For this case study, solar energy is harvested from the photovoltaic panels atop the Fluor Daniel Engineering Innovation Building which are capable of producing 15 kW of DC power at the full solar insolation rating. The electrical power produced varies throughout the day depending on the available solar irradiation and seasons. Next, compressed air energy storage has been evaluated using the generated electric power to operate an electric motor driven piston compressor. The compressed air is then stored under pressure and supplied to a natural

gas driven Capstone C30 microturbine with attached electric power generator. In this approach, the compressed air facilitates the turbine's rotor-blade operated compression stage resulting in direct energy savings. The compressed air energy storage mitigates the intermittency of solar power and provides a continuous energy input to the microturbine over selected time periods.

In this thesis, a series of mathematical models have been developed for the solar panels, an air compressor, the pneumatic storage tank, and the microturbine as they represent the key microgrid system components. An illustrative numerical analysis was then performed to evaluate the feasibility and energy efficiency improvements. The experimental and simulation results indicated that 127.75 watts of peak power were delivered at 17.5 volts and 7.3 amps from each solar panel. The average DC power generation over a 24-hour time period from 115 panels was 75 kW which is equivalent to 30 kW of AC power from the inverter which could run a 5.2 kW reciprocating compressor for approximately 5 hours storing 1,108 kg of air at a 1.2 MPa pressure. The operation of the Capstone C30 microturbine was then simulated using a 0.31 kg/s mass flow rate with 100 air/fuel ratio. A case study indicated that the microturbine, when operated without compressed air storage, consumed 11.16 kg of gaseous propane for 30 kW·hr of energy generation. In contrast, the microturbine operated in conjunction with solar supplied air storage could generate 50.84 kW·hr of electrical energy for similar amount of fuel consumption. The study indicated an 8.1% of efficiency improvement in energy generated for the system which utilized compressed air energy storage over the traditional approach.

An atmospheric driven mechanical Atmos clock manufactured by Jaeger LeCoultre has been investigated due to its capability to harvest energy based on climatic temperature and/or pressure changes to power the clock's mechanisms. The clock's bellows is the power unit which winds the on-board mainspring. The unwinding of this mainspring provides torque to run the gear train, the escapement, and the torsional pendulum. A detailed analysis of the Atmos 540 clock dynamics has been performed using a library of derived mathematical models which describe the bellows' power generation, potential energy of the mainspring, gear train, escapement, and torsional pendulum. Experimental data has been collected using multiple sensors synchronized within the LabVIEW environment from National Instruments.

For this thesis, the mathematical models have been simulated using Matlab/Simulink and validated with the gathered experimental results. The linear motion of the bellows was nearly 6 mm which winds the mainspring over a temperature range of 290-292K. The maximum potential energy of the mainspring was 57e-03J, or 0.67e-06 watts over a 24-hour time period. The minute hand rotation was observed to be 6 degrees/min. The captured crutch motion indicated a 'hold' position for a significant portion of the time (22 sec) and 'impulse' motion for a small portion of the time (8 sec) every 30 seconds in opposite directions. The findings indicated miniscule torque requirement to run the clock. In terms of green energy, the bellows motion is thermo-mechanical energy harvesting.

ACKNOWLEDGEMENTS

TABLE OF CONTENTS

Table of Contents (Continued)

LIST OF TABLES

List of Tables (Continued)

LIST OF FIGURES

List of Figures (Continued)

List of Figures (Continued)

List of Figures (Continued)

List of Figures (Continued)

List of Figures (Continued)

NOMENCLATURE

Symbol	Unit	Description
a	Bar	Ethyl chloride model parameter
A	-	Material dependent parameter
a_1	mm	Pallet fork x-coordinate
a_c	mm	Crank radius
A_d	-	Diode quality factor
A_f	-	Air/fuel ratio
a_p	mm^2	Bellows surface area
A_p	mm^2	Piston surface area
b	bar*K	Ethyl chloride model parameter
B	N*s/mm	Elinvar wire damping coefficient
b_1	mm	Pallet fork y-coordinate
b_{ms}	mm	Main spring cross section width
b_p	mm	Piston diameter
c	K	Ethyl chloride model parameter
C	N/mm	Elinvar wire stiffness constant
c_1	mm	Pallet fork z-coordinate
C_p	kg*m^2/N	Pneumatic capacitance
C_{pa}	KJ/kg*K	Heat capacity for air
C_{pg}	KJ/kg*K	Heat capacity for combustion gas
D	mm	Displacement

Symbol	Unit	Description
D	mm	Diameter
D_1	-	Diode
E	N/mm^2	Modulus of elasticity
E_e	kW·hr	Electrical energy generated at turbine end
E_g	eV	Band gap energy
f_a	N	Atmospheric force acting on bellows
f_b	N	Force acting on bellows surface area
f_c	N	Force of chain attached to bellows
F_c	kg	Fuel consumption
f_{click}	N	Force exerted by click
f_n	N	Normal force
f_{pallet}	N	Force exerted by pallets
f_{roller}	N	Force generated on impulse roller
f_s	N	Force of return spring
f_{tm}	N	Force exerted due to reciprocating mass
f_{tooth}	N	Force generated by escape wheel tooth
f_{tp}	N	Force exerted due to cylinder pressure
I	amp	Current output of solar cell
I_d	amp	Diode current
I_{gen}	amp	Photo generated current
I_{max}	amp	Maximum current

Symbol	Unit	Description
in	-	Input
I_r	W/m^2	Working solar irradiation
I_{r0}	W/m^2	Ideal solar irradiation
I_{rs}	amp	Reverse saturation current
I_s	amp	Saturation current for diode
I_{sc}	amp	Short circuit current
I_{sh}	amp	Current through shunt resistance
J	N*mm^2	Torsional pendulum inertia
K_0	-	Temperature coefficient
K_b	J/K	Boltzmann's constant
k_c	N/mm	Spring constant for chain spring
k_{ec}	N/mm	End cap spring constant
L	mm	Main spring length (unwound)
l	mm	Connecting rod length
m	kg	Torsional pendulum mass
M	g/mole	Molecular mass of C_2H_5Cl
m_b	kg	Mass of bellows end cap
m_g	g	Mass of C_2H_5Cl in bellows
$\dot{m}_a$	kg/sec	Air mass flow rate
$\dot{m}_c$	kg/sec	Air mass flow rate change
$\dot{m}_f$	kg/sec	Fuel mass flow rate

Symbol	Unit	Description
$\dot{m}_{g(in)}$	kg/sec	Combustion gas inlet mass flow rate
$\dot{m}_{g(out)}$	kg/sec	Combustion gas outlet mass flow rate
$\dot{m}_{in}$	kg/sec	Mass flow rate into piston cylinder
$\dot{m}_{out}$	kg/sec	Mass flow rate out of piston cylinder
$\dot{m}_{rec}$	kg	Reciprocating mass of piston cylinder assembly
N	mole	Number of gas moles
N	-	No. of gear teeth
n_p	-	Number of solar panels
N_d	-	Ideal factor for diode
Out	-	Output
P	bar	Instantaneous air pressure inside cylinder
P_a	bar	Atmospheric pressure
P_b	bar	Bellows pressure
P_e	kW	Electric power
$P_{g(in)}$	bar	Turbine inlet pressure
$P_{g(out)}$	bar	Turbine outlet pressure
P_i	bar	Air storage tank inlet pressure
P_{in}	bar	Air compressor inlet pressure
P_o	bar	Air storage tank inlet pressure
P_{out}	bar	Air compressor outlet pressure

Symbol	Unit	Description
Q	C	Electron charge
$Q_{g(in)}$	KJ/hr	Inlet heat rate for turbine
$Q_{g(out)}$	KJ/hr	Outlet heat rate for turbine
Q_{net}	KJ/hr	Net heat rate
R	J/mole*K	Ideal gas constant
r_{51}	mm	Escape wheel radius
r_{61}	mm	Radius of pallet rotation
r_{62}	mm	Distance from point 'P' to point 'Q'
r_7	mm	Impulse roller rotation radius
R_e	-	Escapement gear ratio
R_f	-	Gear ratio
R_g	N*m/kg*K	Ideal gas constant
R_h	-	Hour hand gear ratio
R_m	-	Minute hand gear ratio
r_p	mm	Winding pulley radius
r_r	mm	Ratchet radius
R_s	W/m^2	Solar insolation
R_{se}	ohm	Series resistance
R_{sh}	ohm	Shunt resistance
r_{tp}	mm	Pendulum radius
S	mm	Piston stroke distance

Symbol	Unit	Description
$\ddot{s}$	mm/s^2	Piston acceleration
Sgn	-	Sign function
T	sec	Time
T	K	Instantaneous air temperature
T_{cell}	K	Cell temperature
$T_{g(in)}$	K	Turbine inlet temperature
$T_{g(out)}$	K	Turbine outlet temperature
T_{in}	K	Air compressor inlet temperature
t_{ms}	mm	Main spring cross section thickness
T_{out}	K	Air compressor outlet temperature
T_{ref}	K	Reference temperature
V	volts	Voltage across diode
V_a	m^3	Air accumulator volume
v_b	m^3	Bellows gas volume
V_c	cm^3	Cylinder clearance volume
V_{cyl}	cm^3	Piston cylinder volume
V_{oc}	volts	Open circuit voltage
W_{01}	-	Ratchet wheel on arbor 0 with click
W_{02}	-	Pinion on arbor 0 interfaces to arbor 1
W_{11}	-	Great wheel on arbor 1 interfaces to arbor 2
W_{12}	-	Pinion on arbor 1 interfaces to arbor 0

Symbol	Unit	Description
W_{21}	-	Wheel on arbor 2 interfaces to arbor 3
W_{22}	-	Pinion on arbor 2 interfaces to arbor 1
W_{31}	-	Wheel on arbor 3 interfaces to arbor 4
W_{32}	-	Pinion on arbor 3 interfaces to arbor 2
W_{33}	-	Minute wheel on arbor 3 interfaces to arbor 4
W_{41}	-	Wheel on time arbor 4 interfaces to arbor 5
W_{42}	-	Pinion on time arbor 4 interfaces to arbor 3
W_{43}	-	Hour canon interfaces to arbor 3
W_{51}	-	Escape wheel on arbor 5
W_{52}	-	Pinion on arbor 5 interfaces to arbor 4
W_c	KJ	Air compressor energy consumption
W_{net}	KJ	Net work output
W_t	KJ	Turbine work output
Y	mm	Displacement of bellows end plate
Z	-	Air compressibility factor
γ	-	Heat capacity ratio for air
η	-	System efficiency
η_t	-	Air compressor isentropic efficiency
η_{tm}	-	Turbine mechanical efficiency
θ	rad	Angle between f_{pallet} and f_n
θ_0	rad	Angular rotation of arbor 0

Symbol	Unit	Description
θ_{10}	rad	Initial angular displacement of arbor 1
θ_c	rad	Crankshaft angular rotation
θ_{iR}	rad	Impulse roller angle of rotation
θ_p	rad	Pendulum rotational angle
P	kg/m^3	Air density
τ_{11}	N*mm	Main spring torque
τ_{51}	N*mm	Torque acting on arbor 5
τ_c	N*m	Crankshaft torque
τ_{roller}	N*mm	Torque acting on impulse roller
Ω	rad/s	Crankshaft rotation frequency

CHAPTER ONE

INTRODUCTION

The industrial countries of the 21st century are slowly heading towards an energy crisis and it requires thoughtful action (Friedrichs, 2010). Overall, energy demand is ascending due to rapidly increasing standards of living and manufacturing around the world (Barnham *et al.,* 2006). The significant use of electricity and transportation platforms has resulted in the rapid consumption of coal and petroleum reserves. Over the last decade, countries have begun to explore "green" energy sources such as solar, wind, geothermal, and hydro-electric. The adverse effects on the environment caused by the combustion of byproducts coal, oil, and natural gases are also reasons for the global shift towards renewable energy sources. The efficient use of available green technologies should make them more acceptable and marketable to society. Electric power generation from solar and wind sources have attracted a variety of researchers. The thesis objective is to explore two green concepts: an electrical microgrid at Clemson University campus, and an atmospheric driven clock with mechanical escapement controller.

The abundance of sustainable energy sources such as solar and wind brings several issues that must be solved using effective technologies. Principally, the intermittent nature and integration into the electric grid are two obstacles to the high utilization of solar and wind energy. In the case of solar energy, the photovoltaic (PV) panels vary their output throughout the day depending upon available solar irradiation. The output also varies according to the seasons throughout the year. Wind generated power is also variable because the amount of electricity produced depends on the wind speeds and

availability. A microgrid coupled with energy storage offers an answer to the above mentioned problems. The microgrid is a small, localized, power plant which can serve as a self-dependent and/or supplementary power supply to the conventional grid (El-Khattam and Salama, 2004). Microgrids are generally installed at industrial facilities, commercial complexes, and residential buildings.

Clemson University is planning to lower its greenhouse gas emissions by encouraging energy conservation and eliminating coal burning on campus. The central Building Automated Control System (BACS) keeps in check the operating schedules of power consumption devices. The new buildings on campus are required to obtain LEED (Leadership in Energy and Environmental Design) silver certification. The use of geothermal energy for Lee Hall (opened 2011) on campus provides an excellent sustainable design. During the heating season, the required room temperatures are allowed to drop to 55°F from 69°F when unoccupied. Similarly, during the air-conditioning season, the room temperatures are permitted to scale up to 85°F if unoccupied. An on campus biodiesel plant produces biofuel to operate Clemson University vehicles. Also, the Clemson University Restoration Institute (CURI) is installing a wind turbine testing facility in Charleston, South Carolina to investigate wind energy drive train systems. Finally, the use of public transportation is encouraged through the Clemson Area Transit (CAT) program.

The energy consumption and energy cost data available for Clemson University during the 2003-2011 is shown in Figure 1.1. The data shows a continuous reduction in energy consumption from 2006-2010 but an increase in 2011.
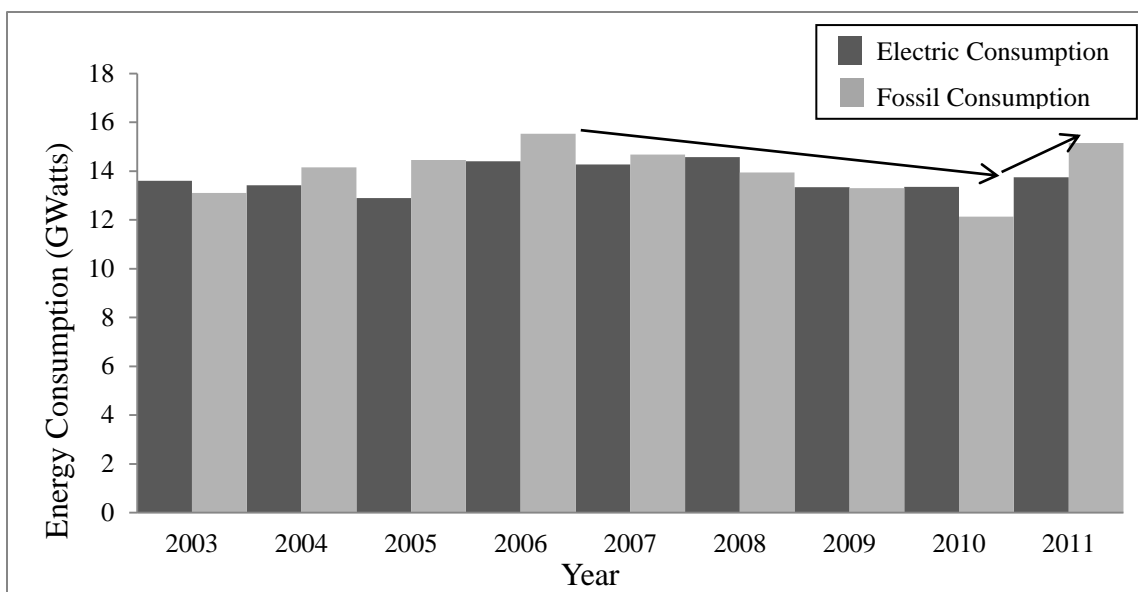
(a)
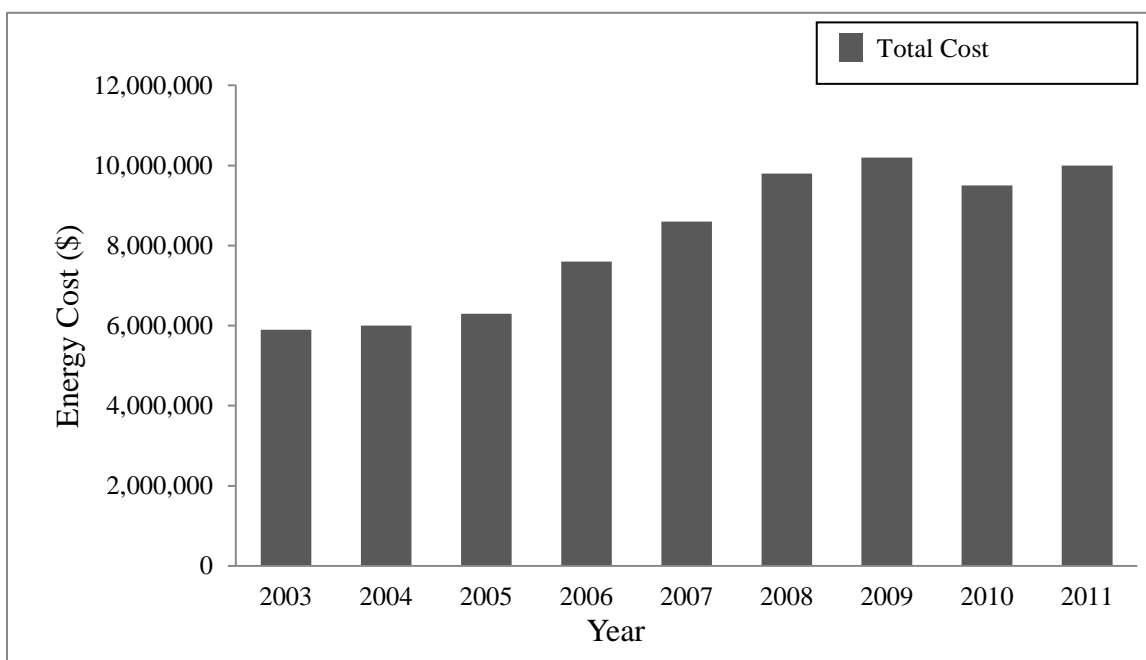
(b)

Figure 1.1: Clemson University (a) energy consumption, and (b) energy cost (Facilities, 2012)

1.1 Green Technologies

The term "green technology" can be defined as the use of science to balance sustainable energy sources and ecology concerns on the earth. The ecological impacts such as air pollution and water contamination can be traced back to the energy & transportation industries; hence, researchers have identified effective means of renewable energy and power generation. The terms solar, wind, geothermal, biofuel, and hydropower have become universal metaphors for environmentally friendly sources due to advancements in green technologies. Solar and wind assisted electric generation helps the production facilities which are independent of fossil fuels. In another novel approach, geothermal energy may be used for both electric power production as well as the heating of buildings. The CO_2 emission of geothermal power plants due to dissolved gases in the fluid is significantly less than that of conventional coal-based power plants (Armannsson *et al., 2005*). Finally, the transportation industry has been benefited due to the extraction of biofuel through a fermentation process of carbohydrate-based crops such as sugarcane and corn.

The solar energy reaching the earth's surface through the atmosphere is harvested mainly by three different methods. A widely popular method to generate electricity is semiconductor devices known as solar cells or photovoltaics modules. These modules are generally mounted on roofs or grounds at specific angles depending upon the geographical location of the installation site. The advanced solar panels are provided with a sun-tracking ability to utilize the maximum amount of photo energy imparted by the sun. Another method for solar energy harvesting is water heating using solar-collectors

4

for residential dwellings and swimming pools. The solar-collectors are transparent square or rectangular boxes positioned facing the sun. The solar heat is absorbed by the black painted surfaces inside these boxes, and tubes carrying water or other fluid transfer heat to the fluid which is ultimately collected in a storage tank. The third method uses heat energy released by the sun for passive heating. The building walls facing the south have maximum exposure to the sun, so these walls are made up of heat absorbing materials. The heat is released controllably to the other sections of the building throughout the day and night.

Energy Storage Methods

One major obstacle to the use of alternative energy sources such as solar and wind is their sporadic availability all round the clock; this problem can be averted with the use of energy storage facilities. Historically, each fuel-powered, traditional centralized power generation unit is designed to operate at maximum efficiency per the rated power output. In general, this power output varies according to changes in electrical demand which adversely affects the plant efficiency. Such a complication can be avoided using energy storage methods so that whenever the electricity requirement is lowered, the excess generated power can be diverted to an energy storage site. On the contrary, if the power requirement is raised, then the additional requirement can be fulfilled using stored power. The following section discusses several energy storage technologies currently incorporated within power plants.

Compressed Air Energy Storage (CAES)

CAES can be considered to be the most cost efficient energy storage technology compared to other methods (Cavallo, 2007). The CAES system has two major components: an air compressor, and an air reservoir or accumulator. A non-fossil based energy source (e.g., solar, fuel cell, etc.), or excess electricity, can be used to directly drive a compressor. Then compressed air can be stored in large tank-like vessels or in underground caverns if geographical contour permits. The stored air is injected into the turbine through the combustion chamber; turbines which are designed for air-assist are modified to achieve direct power savings through bypassing the built in air compressor. In 1949, Germany installed a CAES assisted 290MW power plant located in Huntorf, Germany, which was the first of its kind. The United States has also incorporated CAES technology into 110MW power plant operating in McIntosh, Alabama.
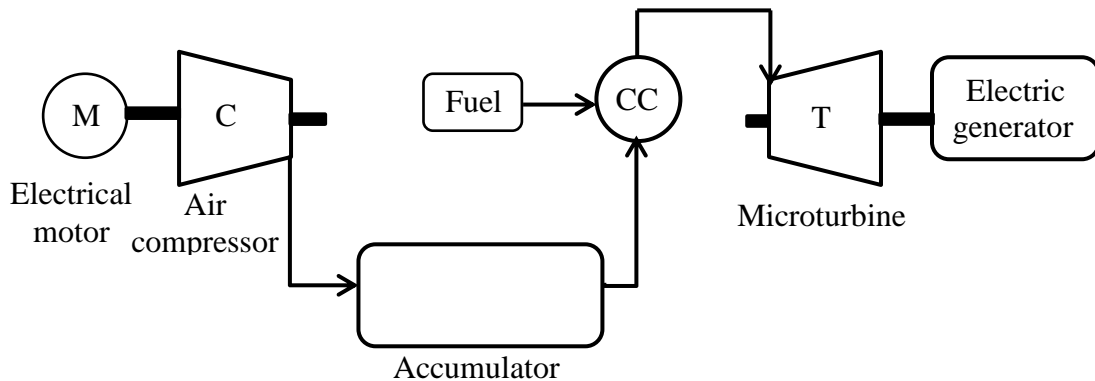
Figure 1.2: Compressed air energy storage schematic

Pumped Hydro Storage

During the off-peak time periods (time of excess power generation), electricity produced by low carbon power sources may be used to pump water from the lower reservoir to the upper reservoir where it is stored. In a pumped hydro storage approach, as

shown in Figure 1.3, at times of higher electricity demand, water flow is reversed through the same penstock, and the turbine can be run in conjunction with the electrical generator to produce electricity. Establishment of the pumped hydro storage facility requires favorable geography which is responsible for its limited worldwide use. Researchers have proposed such a storage facility for the Canarian Islands (Europe) due to geographical advantage and heavy dependency of the Islands on wind energy (Bueno and Carta, 2006). The capital costs involved for such a project are rather high, and there are ecological issues with reservoir creation such as an imbalance of the aquatic environment and damage to the existing wildlife.
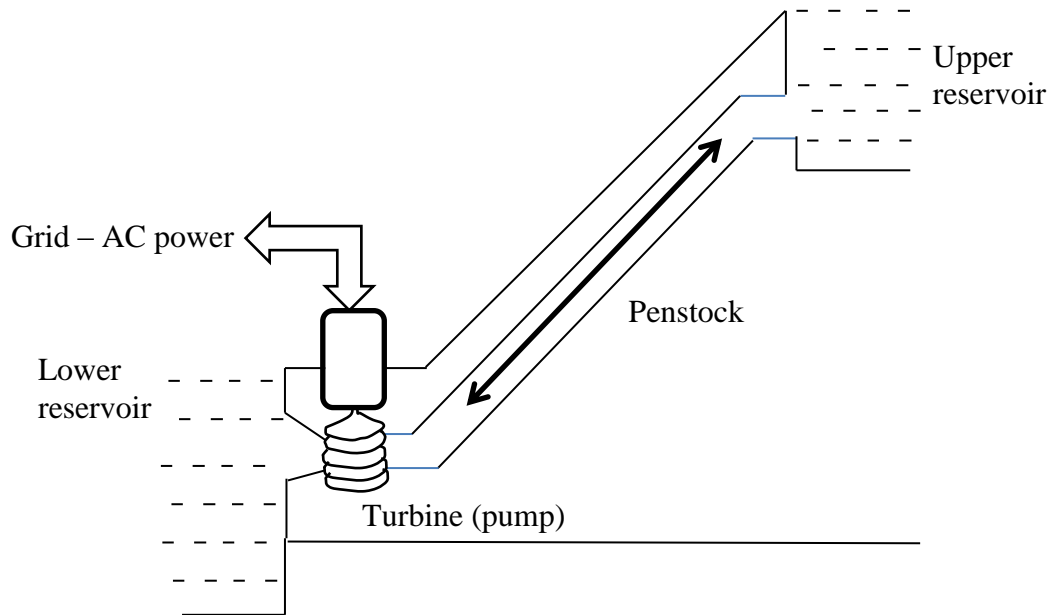
Figure 1.3: Pumped hydro storage schematic

Fuel Cells

Fuel cells contain a cathode, an anode, and a charge carrier medium called an electrolyte to generate electricity. Fuel cells function like batteries, in that the chemical reaction between the oxygen and hydrogen generates an electric charge flow from the

7

anode to cathode which produces direct current. The Fuel cells are replacing batteries in hybrid vehicles, but they have limited capability of energy storage as compared to CAES and pumped hydro storage. The fuel cells can be classified based on the electrolytes used in their construction and operating temperature. Proton Exchange Membrane Fuel Cell (PEMFC), Alkaline Fuel Cell (AFC), and Phosphoric Acid Fuel Cell (PAFC) have low operating temperatures while Solid Oxide Fuel Cell (SOFC) and Molten Carbonate Fuel Cell (MCFC) have high operating temperatures (Carrette *et al.,* 2000).

Batteries

Grid energy storage systems may utilize lead-acid and Lithium (Li) batteries for electric energy storage. The applications of batteries range from automobiles to building back up devices. For Li-ion batteries, the positive electrodes composed of Lithium based materials and the negative electrodes are usually made up of Graphite, Silicon, and Germanium. The electrochemical reactions occur between the anode and the cathode through a closed circuit to produce current. The chemical composition used in the battery construction ensures the amount of electrical energy delivered per mass or volume (Armand *et al.,* 2008). Batteries are generally expensive with limited life and require higher maintenance, so they are not necessarily an attractive option for a microgrid.

Flywheels

Flywheels have existed for many centuries. Flywheels take energy input and store it in the form of kinetic energy. The advancement in materials science has enabled the latest flywheel technology to use rotors made up of carbon-fibers in contrast to metal components used for many years. Typically a large wheel is connected to an electric

motor and/or generator to supply and/or extract energy from the system. The power output from the flywheels is controllable so they can be used as a backup power supply. The technology finds applications in transportation industry due to robustness and durability. A comparison of energy storage capability and capital cost per unit power has been provided in Table 1.1.

Table 1.1: Comparison of different energy storage technologies (Ibrahim *et al.,* 2008)

Technology	Energy Storage Range	Capital cost ($/kW)
Compressed Air Energy Storage	5KWh-10^4MWh	0.6 – 1.0
Pumped Hydro storage	10^2MWh-10^6MWh	0.7 - 2.0
Fuel Cells	1KWh-3MWh	0.7 - 3.0
Flow Batteries	1MWh-2000MWh	0.8 - 3.0
Electrochemical Batteries	1KWh-1MWh	0.4 - 5.0
Flywheels	2KWh-50KWh	0.28 - 10.0

1.2 Electrical Microgrid

A microgrid can be described as a small-scale distributed power generation facility that has become more popular with the power industry due to its advantages. Usage of renewable energy sources such as solar and wind helps to reduce greenhouse gas emission from traditional electrical grid system. Distributed generation supports usage of many exciting technologies such as photovoltaics, wind power, fuel cells, air compressor, microturbine, and internal combustion engine. Localized generation facilities can work in both grid-connected and stand-alone modes which makes the concept more flexible. Traditional electrical grids have higher transmission losses in the form of heat, and these losses can be reduced considerably through the local generation of electricity (Ackermann *et al., 2001*). During peak load periods, microgrids can reduce the load on a

utility grid and prevent it from failure. Further, in the event of disturbances, the loads can be separated from the generation facility to avoid harm to the system.

Microgrid subsystems can be divided into three categories: power generating units, energy storage mechanisms, and power regeneration components. Power generating units can be solar, wind and/or excess electricity generated by the main grids. Any of the energy storage mechanisms described earlier in this chapter can be selected depending upon technical feasibility and cost considerations. The stored energy can be extracted through power regenerating components such as turbines and reciprocating engines. For this project, available microgrid components at Clemson University have been analyzed and integrated to evaluate the feasibility of an updated microgrid system establishment on campus. The Fluor Daniel Engineering Innovation Building on campus has a solar array installed on its roof-top as shown in Figure 1.4. A maximum of 15 kW of DC power goes into the Sunny Boy inverter (SB6000U), which provides 6 kW of AC power output at its peak. A two stage reciprocating air compressor with 7 hp (5.2 kW) rating was selected based on inverter output. The air compressor converts available solar power into stored pneumatic power. The air can be stored in underground salt caverns if the project is significantly large; for the case study, a large cast iron storage tank was considered. The Capstone C30 microturbine has been investigated as a power regeneration facility which burns a mixture of gaseous propane and compressed air injected from the storage tank to produce 30kW of net power.

Figure 1.4: Solar array installed on Fluor Daniel Engineering Innovation Building (North-South view)

A solar array, KYOCERA (KC130GT), has been installed as a part of a grant from Santee Cooper Power in 2007. These types of solar modules are widely used for residential roof-top applications and also for commercial purposes. The panels are provided with a glass cover to withstand harsh climates. An aluminum frame ensures structural strength to these solar modules. According to the KC130GT product catalogue, several quality assurance tests such as a mechanical and wind twist test, water exposure test, thermal shock test, and an electrical isolation test have been carried out for the panel. Figure 1.5 (a) shows that 2,069 kWhr of energy was produced during the month of March, 2012 and approximately 65 kWhr of energy was generated on the 31st of March. The average value of 70kWh is considered for the study as the daily electricity generated from the solar panels. The selection of an AC/DC motor to run an air compressor depends on how the solar power is utilized within specific microgrid system.
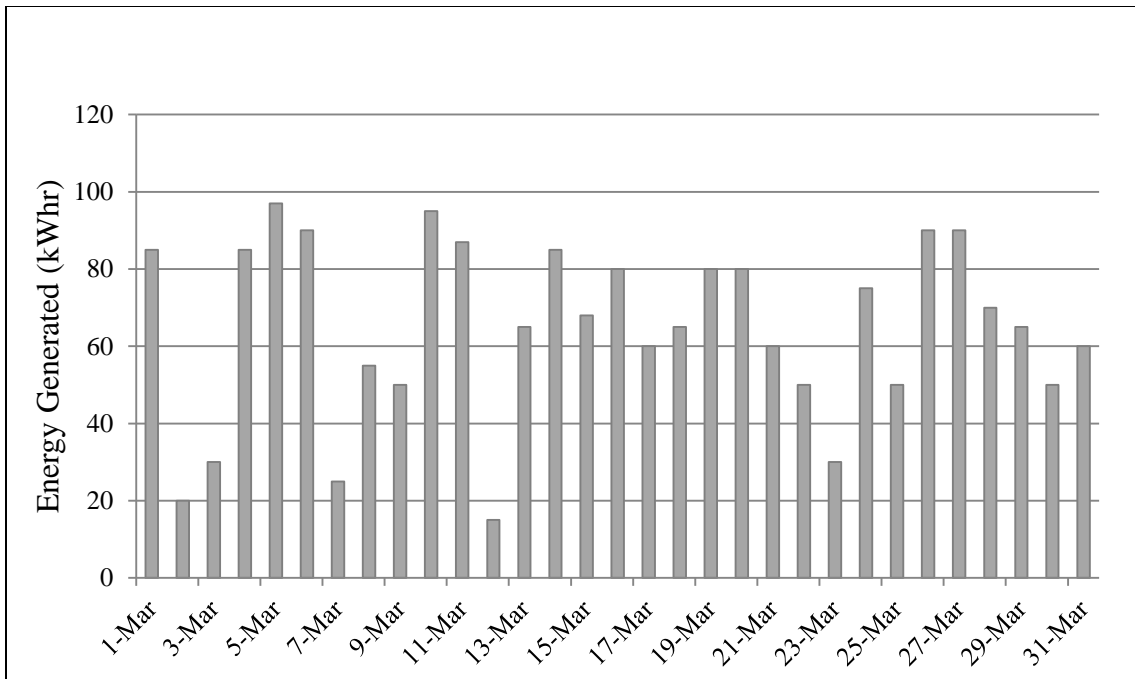
(a)
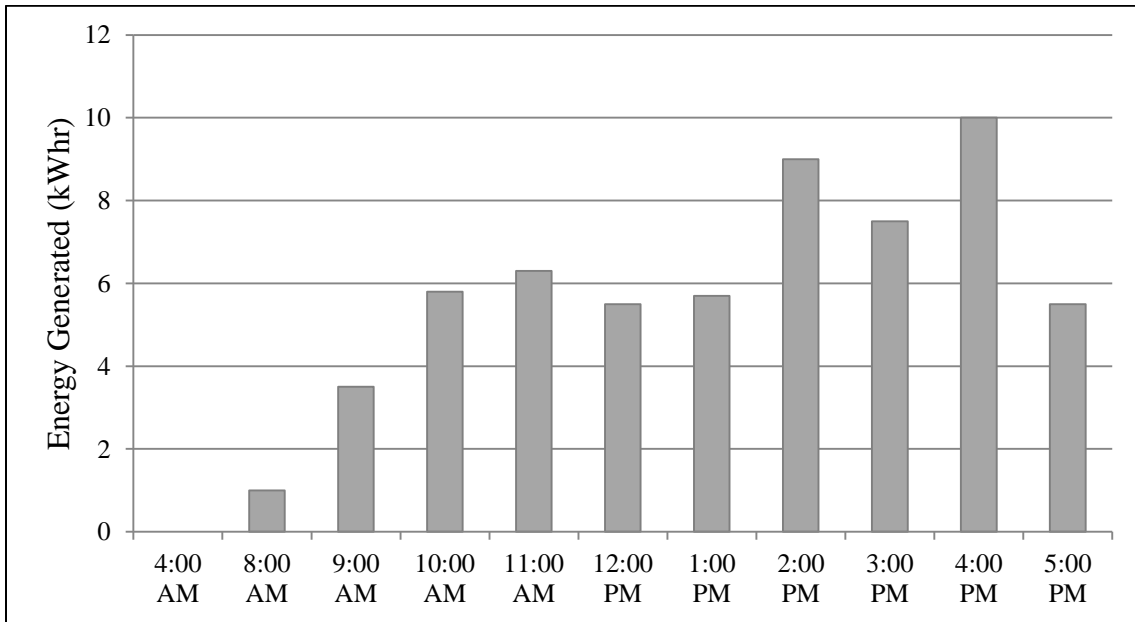
(b)

Figure 1.5: Energy generated by KYOCERA solar panels (a) during March, 2012, and (b) on 31st March, 2012 (Fatspaniel, 2012)

A number of microgrid projects have been implemented in developing, as well as developed, countries. The Santa Rita jail facility located in Dublin, CA has deployed its own microgrid assisted by solar panels, fuel cells, and wind turbines as shown in Figure 1.6 (a) with the help of the U.S. Department of Energy. The facility has 1.2 MW of solar panels integrated with batteries capable of storing up to 2 MW, so the jail can completely work off-grid. The Caribbean Islands have also implemented electrical microgrids. Figure 1.6 (b) represents one such project located in Over Yonder Cay, Bahamas, and this 2 MW project consists of solar and wind units, a battery storage facility, and a diesel based back up system. These examples prove the potential of the microgrid technology to accelerate sustainable growth of the energy sector.

<center>(a)   (b)</center>

Figure 1.6: Electrical microgrid installations (a) Santa Rita jail facility, CA (Chevron, 2012), and (b) Over Yonder Cay, Bahamas (Solar Group, 2012)

1.3 Energy Scavenging Technologies

Energy scavenging methods have existed for many decades and focused on energy sources like vibrations, solar, passive human power, and temperature variations. These small scale energy harvesting technologies have found their applications mainly in the

<center>13</center>

low power electronics industry. Structures which cause considerable vibrations or noise during their operating phase have been utilized to generate milliwatts (mW) of electric power with the help of the piezoelectric devices. Biomechanical energy harvesting technology converts human movements into useful power using magnetic or capacitive generators. Thermoelectric conversion has been used to power wireless sensor networks and miniaturized electronics while the thermo-mechanical conversion has been used to run mechanical clock movements (Paradiso and Starner, 2005). The self-winding wrist watches and mantle clocks have been around for decades, one is called the Atmos clock. The Atmos clock is a thermo-mechanical device which winds a mainspring in the system using forces generated by gas-filled bellows. In this thesis, the Atmos clock has been investigated in detail.

Atmos Clock

The Atmos clock has been considered to be a mechanism that possibly exhibits "perpetual motion". Perpetual motion refers to a system in which the work output is higher than the energy consumed by the system. The perpetual motion machine concept hopes to achieve infinite output with zero input, but it violates either the first and/or the second law of thermodynamics. History does not afford a single instance of ascertained success for perpetual motion. The Atmos clock also falls into a category of "green energy" as it consumes atmospheric thermal energy to fulfill its power need. Parts within the clock are very delicate and they minimize friction as much as possible to ensure small power consumption. The Atmos 540 clock mechanical system may be subdivided into

five subsystems including the winding energy produced by the bellows, potential energy of the mainspring, gear train, escapement and torsional pendulum.

A brief history of time keeping devices will be presented. Sundials and water clocks were the oldest time measurement devices according to written records. Water clocks are known to have existed in ancient civilizations such the Indus, Egyptians, Greeks and Romans around the 16th century BC. The first mechanical clocks appeared in Europe during the 13th century. In Medieval times, mechanical tower clocks were used to indicate the passage of time throughout the day for community prayers. During the 15th and 16th centuries, manufacturing of time keeping devices flourished particularly in the metal working centers in Europe. The evolution of clock mechanisms is shown in Figure 1.7. The time measurement accuracy of the clocks improved while the size of the clocks has been reduced.
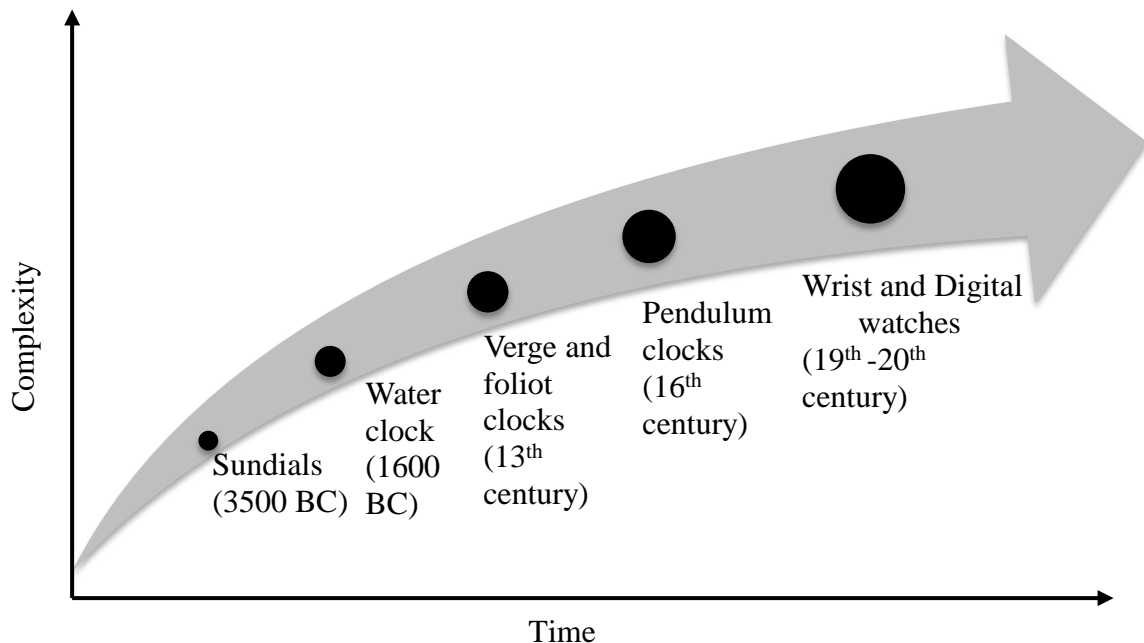
Figure 1.7: Clock evolution history timeline

The Atmos clock, studied in this thesis, provides an excellent example of mechanical energy harvesting with the help of atmospheric temperature and pressure changes. The hermitically sealed bellows in the atmos clock are filled with a gaseous and liquid form of Ethyl Chloride. As the surrounding temperature increases or decreases, the gas inside bellows expands or contracts causing the linear motion of the attached chain. The atmosphere's thermal energy is transferred into mechanical motion which is ultimately stored in the form of potential energy of the main spring. The controlled unwinding of the mainspring feeds power to the clock mechanisms such as the escapement and the clock hands. The thermo-mechanical conversion of energy generates microwatts (µW) of power which is sufficient to operate the clock for several days.

1.4 Thesis Organization

This research thesis is divided into four chapters. Chapter 1 introduces both the microgrid and the Atmos clock concepts. Chapter 2 provides detailed insight into the microgrid components and their accompanying mathematical models. It also covers the experimental and simulated results for the components. Chapter 3 describes an Atmos clock with its mechanical subsystems, energy flow through the clock, mathematical representation of each subsystem, and numerical/ experimental results. Chapter 4 concludes the thesis with a focus on the outcome of the research and also describes the scope of future research challenges and recommendations. The Appendices contain the Matlab/Simulink simulation block diagrams along with experimental results for the microgrid and the Atmos clock. It also presents Atmos clock component measurement tables and motion works models prepared in Solidworks.

CHAPTER TWO

MICROGRID AT CLEMSON UNIVERSITY: INTEGRATION OF SOLAR CELLS, COMPRESSED AIR STORAGE, AND MICRO-CAP GAS TURBINE TO GENERATE ELECTRIC POWER

The centralized large scale generation of electricity has been extensively used for the past century with much success. As electrical utilities and individuals consider green energy alternatives, a need exists to create small grid for power consumptions and connection to existing grid. Micro grids encompass electricity generation, power storage, and distribution. In this chapter, a hypothetical micro grid at Clemson University will be investigated which features solar panels, pneumatic energy storage, and gas turbine power assistance. A series of mathematical models will be prepared for solar cells, air compressor, air storage, and microturbine. Representative numerical results will be presented which show a 9-10% improvement in energy efficiency. The research project represents an important step towards a "net zero campus".

2.1 Introduction

The emerging worldwide energy crisis can be attributed to the growing demand for electric power and personal/commercial transportation on all continents. Although fossil fuels will continue to be available for many decades, the amount of petroleum remaining and its associated cost remain an open issue. To meet this critical societal need, research into alternative energy sources such as solar and wind for electric power generation is underway at Clemson University. One challenge with these two energy sources is their availability throughout a 24-hour time period as they rely upon nature to provide the sunshine and blowing winds which interact with the solar panels and wind turbines. In

17

this research project, energy storage will be investigated using compressed air so that electric power can be generated "on demand" during peak times based on consumer requirements and stored during "low demand" time periods.

For the case study, solar energy will be harvested on campus from the photovoltaic (PV) panels atop the Fluor Daniel Engineering Innovation Building. The electrical power produced varies throughout the day depending on the available solar irradiation and seasons. Next, compressed air energy storage (e.g., accumulator) will be evaluated using the generated electric power to operate an electric motor driven compressor. The compress air will be stored under pressure and supplied to a natural gas driven micro-cap turbine with attached electric generator. In this approach, the compressed air will facilitate the turbine's rotor-blade operated compression stage resulting in direct energy savings. The microturbine design is generally modified by removing in built centrifugal compressor rotors and the compressed air is given directly to the combustor of the turbine. Figure 2.1 represents power flow through the various components of the proposed lectrical microgrid.
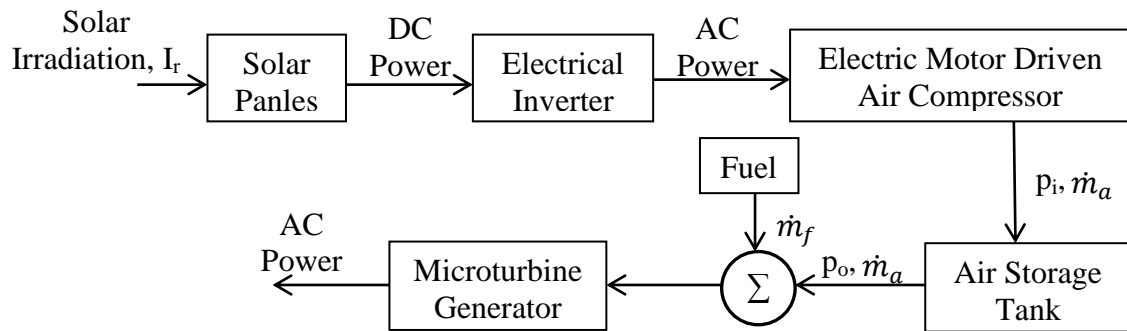
Figure 2.1: Power flow diagram for electrical microgrid at Clemson University

A considerable amount of research has been carried out in field of microgrid over the past two decades. Pepermans *et al.* (2005) identified benefits and issues related to

18

distributed generation. Lasseter and Piagi (2004) indicated that concept of on-site generation and local distribution makes microgrid more reliabl and highly effcient (reduced transmission losses). Suryanarayan *et al.* (2010) investigated use ofenergy storage assisted microgrid to achieve smart grid. Azab developed improved circuit model to represent photovoltaics. Tsai *et al.* (2008) presented generalized photovoltaic model using Matlab/Simulink. Al-Qattan *et al.* (2009) diagnosed angular speed and power for the single stage, double acting receiprocating compressor. Elhaj *et al.* (2008) performed numerical and experimental study on receiprocating compressor for condition monitoring. Venkatesan *et al.* (2009) developed mathematical model for water cooled automotive air compressor. Al-Hamdan and Ebaid (2006) explored gas turbine component synchronization through compressor and turbine performance characteristics and also simulated gas turbine system. Sekhon *et al.* (2006) developed a nonlinear dynamic model for solar mercury 50 stationary gas turbine in order to simulate transient and steady state operations of system. Shively *et al.* (2008) compared compressed air energy storage (CAES) and graviational potential method to store energy and analysed pros and cons for grid support.

In this chapter of the thesis, micro grid components with their working principles are described in Section 2.2 followed by mathematical modelling in Section 2.3 which covers models for the solar cells, air compressor, storage tank, and microturbine. Section 2.4 contains numerical analysis and discussion of results based on matlab/simulink and also a case study conducted. Finally, the summary is contained in Section 2.5.

2.2 Microgrid System Configuration

The micro grid facility can use solar, wind, and extra electricity produced during low demand times and stores it using energy storage methods available for the particular micro grid project. The micro grid system at Clemson University consists of solar panels for electricity generation, a sunny boy inverter, air compressor, compressed air storage, and Capstone C30 microturbine as shown in Figure 2.2. These components with their working principles will be described in this section of the chapter.
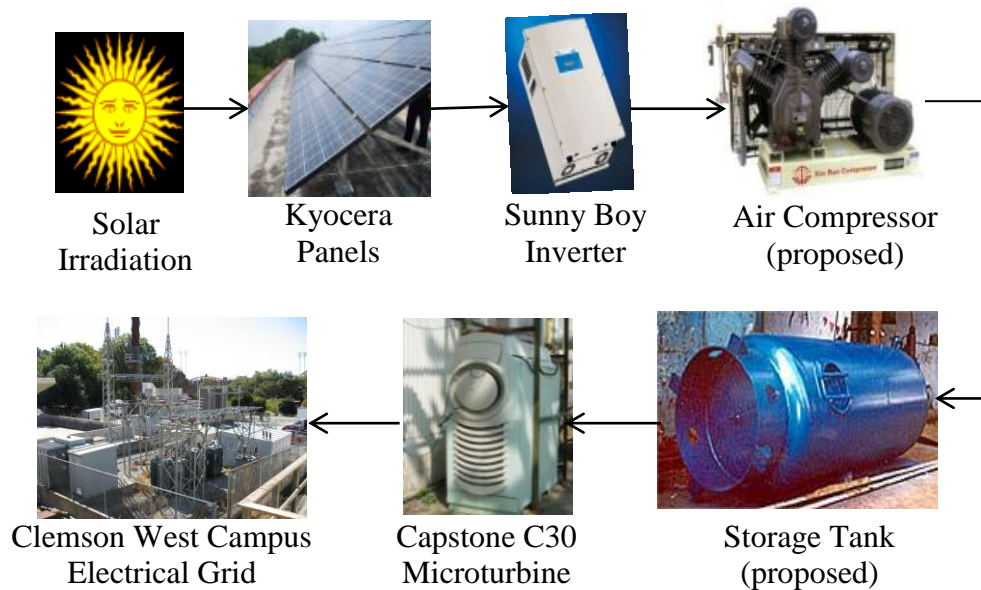
Figure 2.2: A microgrid for Clemson University electrical subsystem featuring solar panels, compressed air storage, and microturbine.

Solar Panel and Electrical Inverter

Solar cells work on a photovoltaic (PV) phenomenon. These cells encapsulated and connected in series or parallel as a module according to requirement of application forms solar panel. Solar cells are made up of semiconductor materials such as silicon (monocrystalline /polycrystalline), copper indium sulfide, cadmium telluride. To understand operation of a PV cell generalized circuit model has been developed by many

researchers as shown in Figure 2.3 (Tsai *et al.,* 2008). The intensity of solar spectrum observed on the earth's surface is termed as air mass 1. When sunlight imparts on solar cells, the absorbed photons help to create flow of current across the depletion region. At Clemson University, an inverter (Sunny Boy SB6000U) has been installed to convert solar panel generated DC current into AC current as shown in Figure 2.4. The output voltage of an inverter can be adjusted as per requirement with use of transformers. Microturbine generated AC power is delivered to local electrical loads.
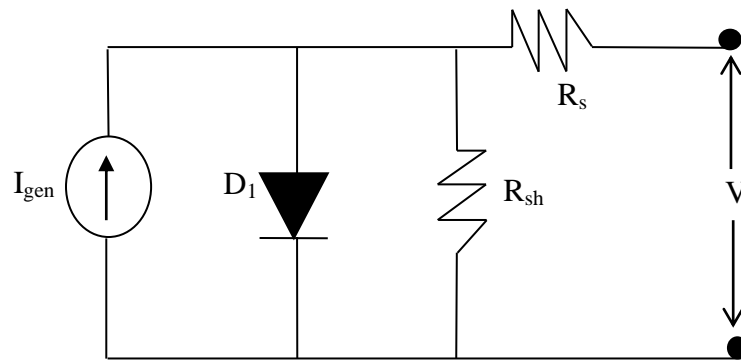
Figure 2.3: Solar cell equivalent circuit diagram featuring resistor and diode elements
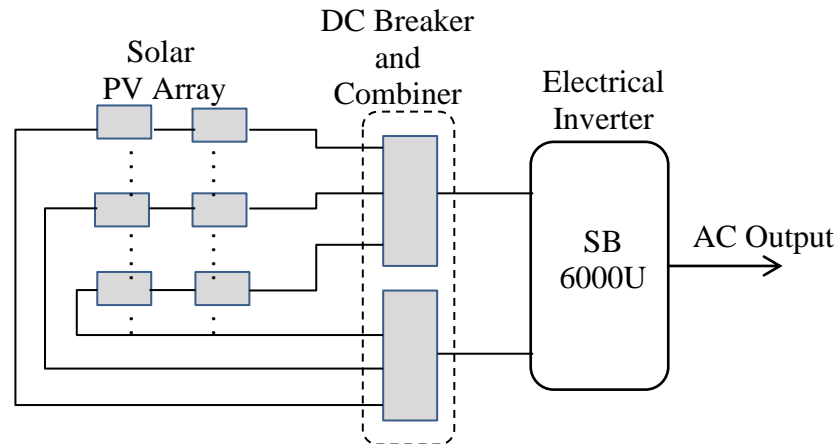
Figure 2.4: Electrical inverter connected to photovoltaic solar cell array with series panel assembly and DC breaker and combiner to prepare power feed

Air Compressor and Air Storage Tank

A two stage electric motor driven reciprocating air compressor with inline valve and air storage tank has been considered for this study as shown in Figure 2.5 due to its wide availability. The AC motor operated with the solar power generated electricity runs the air compressor. Thus solar power generated during off peak hours is converted in the form of compressed air. The selected air compressor for the study is capable of providing maximum of 175 psi at 17 scfm and 1725 rpm. The air compressor selection depends upon the requirement of the particular air storage facility.
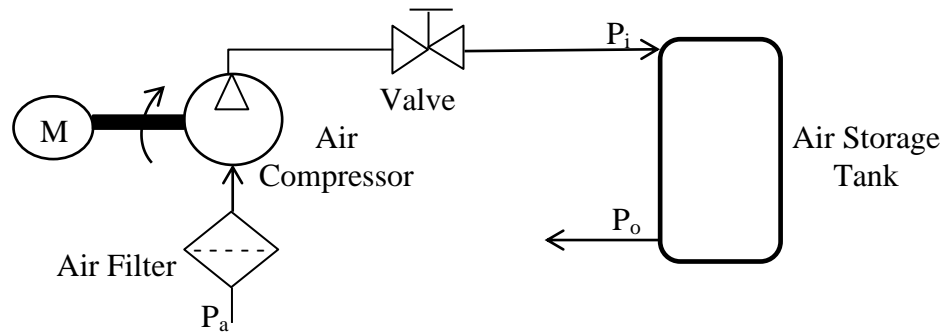
Figure 2.5: Electrical motor driven air compressor and compressed air storage tank

Compressed air is stored in a large "tank like vessel" at the required pressure. It is widely known as compressed air energy storage (CAES). For smaller projects, storage tanks are used while for a large scale power generation facility, underground caverns are typically used. The compressed air supplies the necessary air flow to the turbine as and when needed.

Microturbine with Electrical Generator

A smaller version of a traditional gas turbine is known as a microturbine and ranges between 1 kW to 4.5 MW. Their compact components provide a higher power to weight ratio and typically burns gaseous propane. In this study, a Capstone C30 microturbine at

Clemson University has been investigated with supplemental compressed air flow as displayed in Figure 2.6. The Capstone C30 microturbine can generate 30kW of AC power at its full capacity.
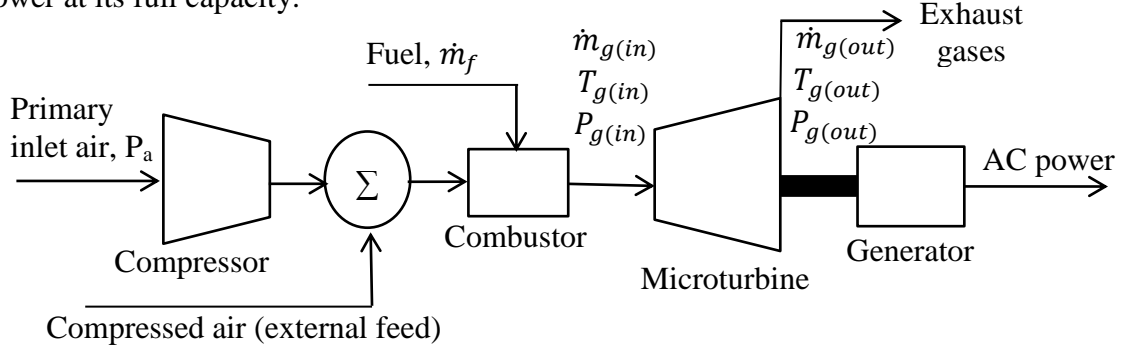
Figure 2.6: Capstone C30 microturbine with AC generator connected to air storage tank

2.3 Mathematical Model

The mathematical models representing solar cell, air compressor and microturbine dynamics will be presented in this section. The model parameter values have been considered for the available system components on the Clemson University campus.

Solar Cell

The solar cell models have been developed by many researchers. The authors have adopted prevalent mathematical representation of solar cell (Tsai *et al.,* 2008, Azab, 2009). As photons hit the cell surface some are absorbed which creates an electro motive force. When infinite resistance (open circuit) is provided, a voltmeter will show maximum value of voltage which is the open-circuit voltage V_{oc}. On the other hand, if the load resistance is set to zero (short circuit), then the solar cell draws a maximum amount of current, I_{sc}. The photon generated current, I_{gen}, relies on solar irradiation and the cell's working temperature, T_{cell}, so that

$$I_{gen} = I_{sc}\left(\frac{I_{r0}}{I_r}\right) + K_0(T_{cell} - T_{ref}) \tag{2.1}$$

where I_{r0} is the ideal solar irradiation, I_r is the working solar irradiation, T_{ref} is the reference temperature, and K_0 is the current temperature coefficient.

The saturation current, I_{sat}, for the cell highly depends on cell's working temperature and semiconductor material properties such that

$$I_{sat} = I_{rs}\left(\frac{T_{cell}}{T_{ref}}\right)^{3/n} exp\left[\frac{E_g q}{K_b N_d}\left(\frac{1}{T_{ref}} - \frac{1}{T_{cell}}\right)\right] \tag{2.2}$$

where I_{rs} is the reverse saturation current for the cell, n is the number of cells in series, E_g is the band gap energy for semiconductor material used, q is the electron charge, K_b is Boltzmann's constant, and A_d is the diode quality factor.

The reverse biased condition of solar cell produces leakage current due to amalgamation of the charge carriers. This reverse saturation current, I_{rs}, is given by the expression

$$I_{rs} = I_{sc}/[\exp\left(\frac{qV_{oc}}{K_b T_{cell} A_d}\right) - 1] \tag{2.3}$$

As shown in Figure 2.3, series resistor R_s indicate resistance provided by the depletion region against the flow of current across depletion layer. The voltage-current, V-I, characteristics for ideal diode in the circuit (forward biased / reverse biased) is expressed by Shockley diode equation as

$$I_d = I_{sat}[\exp\left(\frac{qV}{n_p K_b T_{cell} A_d}\right) - 1] \tag{2.4}$$

where I_d is the current flowing through diode, V is the voltage across diode (volts), and n is the ideal diode factor.

The maximum voltage of V_{oc} can be given across diode and corresponding current output is observed. The V-I characteristics for the solar cell is obtained from the following equation as

$$I = I_{gen} - I_d - (V + IR_s)/R_{sh} \qquad (2.5)$$

where I is the solar cell output current and R_{sh} is shunt resistance.

Table 2.1 provides the electrical and thermal parameters of solar panel considered for this study. The parameter values for the KC130GT photovoltaic module have been taken from the product catalogue provided by the company.

Table 2.1: Kyocera (KC130GT) photovoltaic module parameters

Symbol	Value	Units	Symbol	Value	Units
A_d	1.2	-	K_0	3.2×10^{-3}	A/°C
E_g	1.12	eV	q	1.6×10^{19}	C
I_{max}	7.39	Amp	T_{ref}	298	K
I_{sc}	8.02	Amp	V_{oc}	21.9	Volts
K_b	1.38×10^{-23}	J/K	n_p	115	-

Air Compressor

A two stage reciprocating air compressor will be investigated in this section. A representative piston-cylinder assembly, shown in Figure 2.7, has been taken into consideration. The mathematical model focuses on the torque variation on the crankshaft due to pressure changes in both low and high pressure cylinders with respect to crank angular rotation (Elhaj *et al.,* 2008, Al-Qattan *et al.,* 2009).

The stroke distance, s, is a function of angular rotation of the crankshaft. The top dead center (TDC) is assumed to be starting location of piston motion such that at TDC,

angular rotation of crankshaft θ = 0 rad, s =0, and piston cylinder volume $V_{cyl} = V_c$ with

V_c denoting the clearance volume.
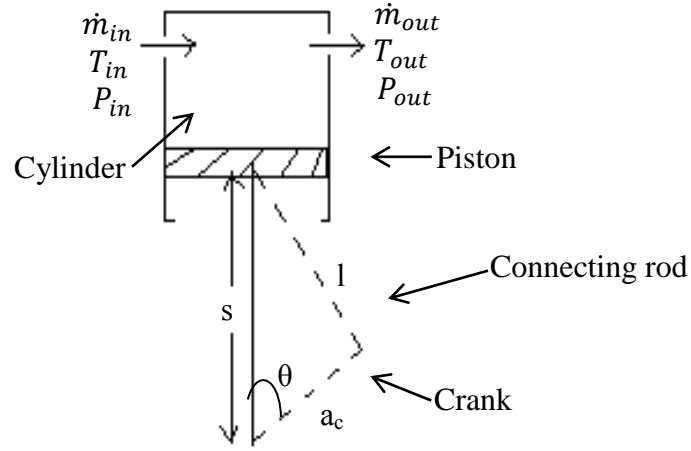
Figure 2.7: Piston-cylinder assembly schematic for the air compressor

At BDC (Bottom Dead Center), θ = 180, s = 2a_c, and the piston cylinder volume V_{cyl}

= V_c with V_c denoting the clearance volume so that

$$V_{cyl} = V_c + \left(\frac{\pi}{4}\right) b_P^2 s \qquad (2.6)$$

where a_c is the crank radius and b_p is the piston diameter.

At any given crank angle, the stroke distance as a function of angular rotation of

crank shaft is given as (Elhaj *et al.,* 2008)

$$s = a_c + l - a_c \cos \theta_c - \sqrt{l^2 - a_c^2 sin^2 \theta_c} \qquad (2.7)$$

where l is the connecting rod length.

The angular acceleration of piston, $\ddot{s}$, may be derived taking second time derivative of

eq. (2.7) so that

$$\ddot{s} = a_c \omega^2 \left(cos\theta_c + \left(\frac{a_c}{l}\right) cos2\theta_c \right) \qquad (2.8)$$

The cylinder discharge temperature, T_{out}, as a result of isentropic temperature rise inside the piston cylinder can be expressed as

$$T_{out} - T_{in} = T_{in} \left[\left(\frac{P_{out}}{P_{in}} \right)^{(\gamma-1)/\gamma\eta_t} - 1 \right] \tag{2.9}$$

where T_{in} is the cylinder inlet temperature, T_{out} is the cylinder outlet temperature, P_{out} is the discharge pressure, P_{in} is the inlet pressure, γ is the heat capacity ration, and η_t is the isentropic efficiency.

The instantaneous pressure, P, can be found using the ideal gas law as

$$PV_{cyl} = nRT \tag{2.10}$$

where n is the number of moles of air, R is the ideal gas constant, and T is the instantaneous temperature.

The compressibility factor, z, of air at given temperature, T, pressure, P, and air density, ρ, may be calculated as

$$z = \frac{P}{\rho R_a T} \tag{2.11}$$

The compressibility factor which is 1.004 for the given temperature and pressure range of the air compressor has been considered as 1.000 to model the air as an ideal gas.

The pressure changes inside both the high and low pressure cylinders exert variable tangential force, f_{tp}, which can be calculated as

$$f_{tp} = PA_P \tag{2.12}$$

where A_P is the piston surface area.

The reciprocating mass of the piston-cylinder assembly also produces a variable tangential force, f_{tm}, which is expressed as

$$f_{tm} = \mathrm{m}_{\mathrm{rec}} \, \ddot{s} \tag{2.13}$$

where $\mathrm{m}_{\mathrm{rec}}$ is the mass of reciprocating assembly.

The force exerted through pressure variations and the force due to reciprocating mass collectively develops the torque on crankshaft, $\mathrm{T_c}$, given as

$$T_c = (f_{tp} + f_{tm})d \tag{2.14}$$

where the distance, d, between the acting force vector and the center of crankshaft rotation can be derived from geometry shown in Figure 2.6 as

$$d = \sin\theta_c + \left[\frac{a\sin\theta_c \cos\theta_c}{\sqrt{l^2 - a^2 \sin\theta_c}}\right] \tag{2.15}$$

Air Storage Tank

The air storage tank is assumed to have a fixed volume of 144 m^3 which is sufficient to operate the microturbine for approximately 60 minutes to generate electric power. The dynamic behavior of this pneumatic system is presented based on known engineering concepts (Ogata, 2004).

In some respects, the air injection into a container can be considered to be a slow process which allows heat to dissipate into the surroundings (isothermal process). The pneumatic capacitance, C, of a container for an ideal gas may be given as

$$C = V_a / R_g T_a \tag{2.16}$$

where V_a is the air accumulator volume, R_g is the ideal gas constant, and T_a is the air temperature inside the tank.

The air mass increase in the container will lead to a pressure rise. The time derivative of the pressure inside the container, p_o, depends on the change in mass flow rate so that

$$C dp_o = \dot{m}_c dt \tag{2.17}$$

28

where $\dot{m}_c$ is the change in air mass flow rate. The air compressor and storage tank model parameters are summarized in Table 2.2.

Table 2.2: Air compressor and storage tank model parameters

Symbol	Value	Units	Symbol	Value	Units
a	30	mm	S	60	mm
b	76.2	mm	T_a	300	K
C	0.0016	kg*m^2/N	T_{in}	288	K
l	150	mm	V_a	144	m^3
m_{rec}	5	kg	V_c	20	cm^3
$\dot{m}_c$	0.0083	kg/s	V_{cyl}	276	cm^3
p_{in}	1	bar	γ	1.4	-
R	8.314	J/mole*K	η_t	0.85	-
R_g	287	N*m/kg*K	ρ	7.7	kg/m^3

Microturbine

The Capstone C30 microturbine available at Clemson University has been investigated for the study. The existing nonlinear thermodynamic models representing the gas turbine characteristics have been adopted to pursue this study (Ailer *et al.,* 2001, Shively *et al.,* 2004, Al-Hamdan *et al.,* 2006, Sekhon *et al.,* 2006) The compressed air will be provided from the air storage tanks, so the built in turbine compressor will be bypassed and the air injected directly into the combustor.

The ideal gas turbine cycle will be considered for the study with the three assumptions listed below:

A.1: Expansion of gases in turbine is reversible and adiabatic.

A.2: The pressure losses in combustion chamber and in ducts are negligible.

A.3: The mass flow rates, $\dot{m}_{g(in)} = \dot{m}_{g(out)} = \dot{m}_f + \dot{m}_a$.

The turbine specific work output, W_t, is given as

$$W_t = \dot{m}_{g(in)} C_{pg} (T_{g(in)} - T_{g(out)}) \tag{2.18}$$

where $\dot{m}_{g(in)}$ is the mass flow rate through the turbine, C_{pg} is the specific heat of combustion gases, $T_{g(in)}$ is the turbine inlet gas temperature, and $T_{g(out)}$ is the turbine exhaust gas temperature.

The work transfer in the turbine due to expansion of combustion gases may be stated in terms of the temperature equivalents as

$$\frac{W_t}{\dot{m}_{g(in)} C_{pg}} = T_{g(in)} - T_{g(out)} = \eta_{tm} T_{g(in)} \left[1 - \left(\frac{p_{g(out)}}{p_{g(in)}} \right)^{(\gamma-1)/\gamma} \right] \tag{2.19}$$

where η_{tm} is the turbine mechanical efficiency, $p_{g(in)}$ is the turbine inlet gas pressure, $p_{g(out)}$ is the turbine exhaust gas pressure, and γ is the heat capacity for the combustion gases.

The gas turbine assembly is considered to be fixed with a non–deforming control volume in which the contents do not change. So, the principle of conservation of mass can be applied such that

$$\frac{d\dot{m}_{g(in)}}{dt} = \dot{m}_{g(in)} - \dot{m}_{g(out)} \tag{2.20}$$

where $d\dot{m}_{g(in)}/dt$ is the change in the system mass flow rate, $\dot{m}_{g(in)}$ is the inlet mass flow rate of the combustion gases, and $\dot{m}_{g(out)}$ is the exhaust gas mass flow rate.

The energy balance equation for the turbine control volume is derived from the first law of thermodynamics. The generalized energy equation for net work output, W_{net}, is given as (Cohen *et al.*, 1996)

$$W_{net} = W_t - W_c \tag{2.21}$$

where W_c represents the energy consumed to run the built in turbine air compressor turbine. The equation (2.20) can be expanded using eq. (2.9) and eq. (2.17) as

$$W_{net} = \dot{m}_{g(in)}C_{pg}T_{g(in)} - \dot{m}_{g(out)}C_{pg}T_{g(out)} - \dot{m}_a C_{pa}(T_{out} - T_{in}) \qquad (2.22)$$

where $\dot{m}_{g(in)}$, $\dot{m}_{g(out)}$ are the turbine inlet and exhaust mass flow rates respectively, $T_{g(in)}$, $T_{g(out)}$ are the turbine inlet and exhaust gas temperatures respectively, C_{pa} is specific heat for air. The net heat transfer in the system will be $Q_{net} = Q_{g(in)} - Q_{g(out)}$, where $Q_{g(in)}$ and $Q_{g(out)}$ are turbine inlet and exhaust heat rates (Shively *et al.,* 2008).

The electrical power generator at the downstream of Capstone C30 microturbine can provide up to 30kW of AC power depending upon load variations. The model parameters for the Capstone C30 microturbine are listed in Table 2.3.

Table 2.3: Capstone C30 microturbine model parameters

Symbol	Value	Units	Symbol	Value	Units
C_{pa}	1.005	KJ/kg*K	$Q_{g(in)}$	554,652	KJ/hr
C_{pg}	1.147	KJ/kg*K	$Q_{g(out)}$	327,000	KJ/hr
$\dot{m}_{g(in)}$	0.31	kg/s	$T_{g(in)}$	690	K
$\dot{m}_{g(out)}$	0.31	kg/s	$T_{g(out)}$	547	K
$P_{g(in)}$	11	bar	γ	1.33	-
$P_{g(out)}$	1.1	bar	η_{tm}	0.90	-

2.4 Numerical Results and Discussion

The presented mathematical models for solar cell, air compressor, air storage, and microturbine have been analyzed based on the system parameter values considered in the study. The results obtained through the Matlab/Simulink models are used as the selection criteria for the successive component in the system (i.e., the air compressor has been selected depending upon the power output provided by solar panel model).

Solar Cell

The solar cell mathematical model has been simulated in Matlab/Simulink to obtain the V-I and V-P characteristics. The maximum voltage and maximum current for the peak power are 17.5 volts and 7.28 amps as shown in Figure 2.8.
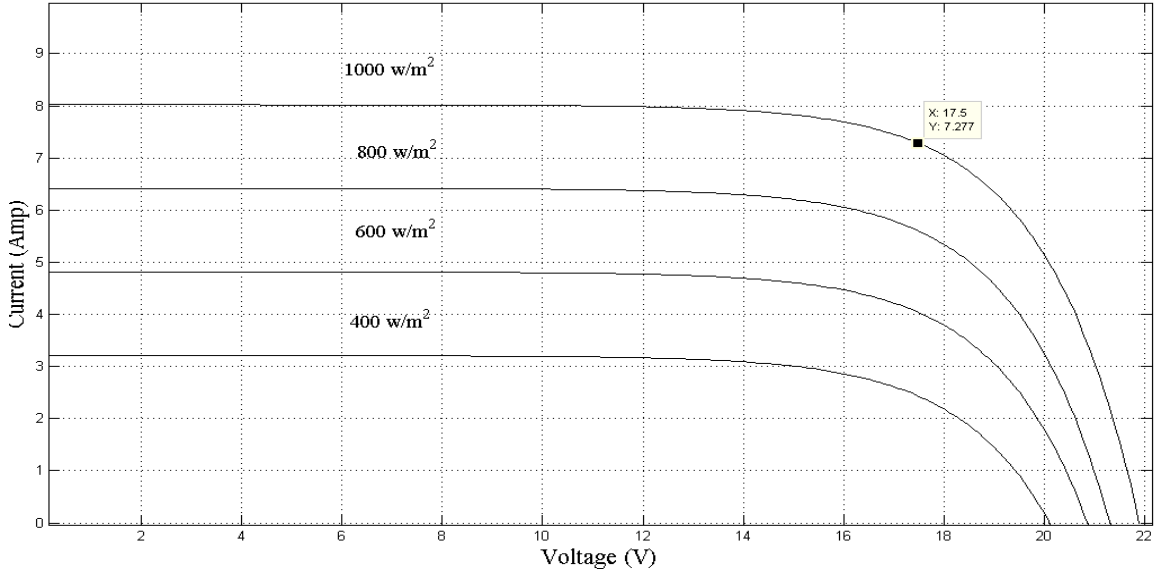
Figure 2.8: Voltage-current characteristics at different solar irradiation for photovoltaic module KC130GT used in study

The results indicate that maximum power at full solar insolation of 1000 w/m^2 is approximately 127 watts per panel as shown in Figure 2.9 which is equivalent to maximum power capacity specified as 130 watts in manufacturer's catalogue. The total of 115 solar panels each creating 130 watts of power are connected in series to produce approximately 15 kW of maximum power.

$$Number\ of\ panels\ (115) \times Each\ panel(130\ watts) = 14.95 kW \qquad (2.23)$$

The output from the KC130GT panels is provided to the inverter (Sunny Boy SB6000U) ultimately yielding 6 kW of AC power in the form of 25A at 208, 240 VAC, or 21.7A at 277VAC.

$$15kW\ DC\ input \times 0.40\ Inverter\ efficiency = 6kW\ AC\ output \qquad (2.24)$$
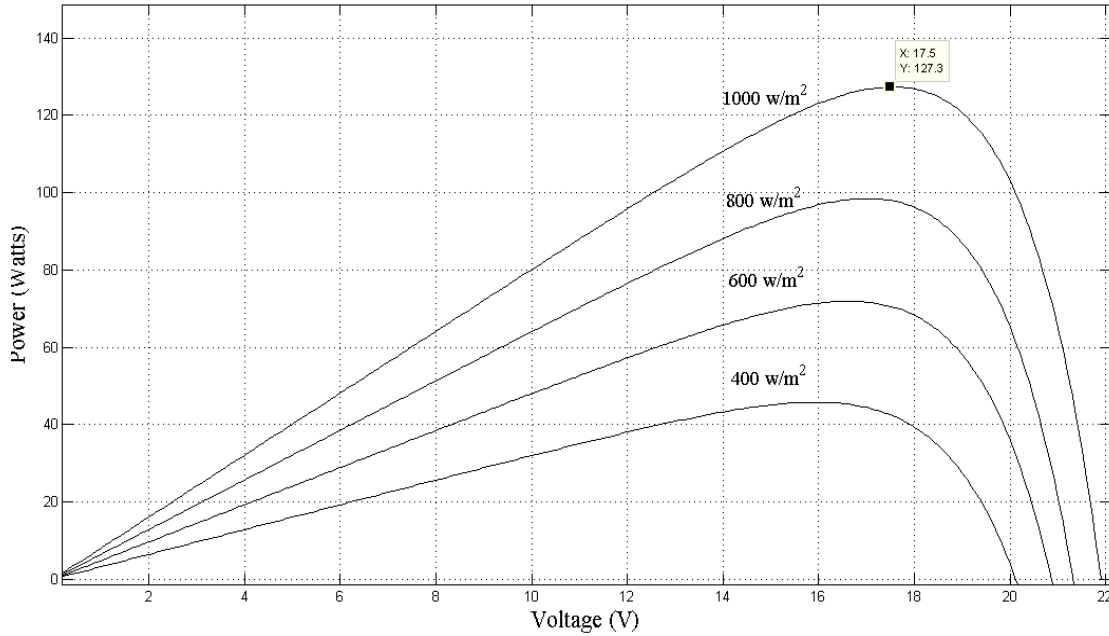
Figure 2.9: Voltage-power characteristics at different solar irradiation for photovoltaic module KC130GT mounted on the Fluor Daniel Engineering Innovation Building at Clemson University

Air Compressor and Air Storage

A two-stage reciprocating air compressor has been considered for the simulation. The major findings of the model are the cylinder pressure variation, crankshaft torque variation, and cylinder swept volume vs. pressure changes. These results help to understand the torque profile requirements from the electric motor to run the air compressor. The low pressure cylinder pressure profile is shown in Figure 2.10. The trapped air pressure from the previous stroke is taken as the starting point. The suction stroke up to an 180^0 crank angle follows the atmospheric pressure. The pressure rise can

be observed between 180^0 and 320^0 of crank angle rotation. The discharge stage has a small pressure drop between 320^0 and 360^0 of crank angle rotation.
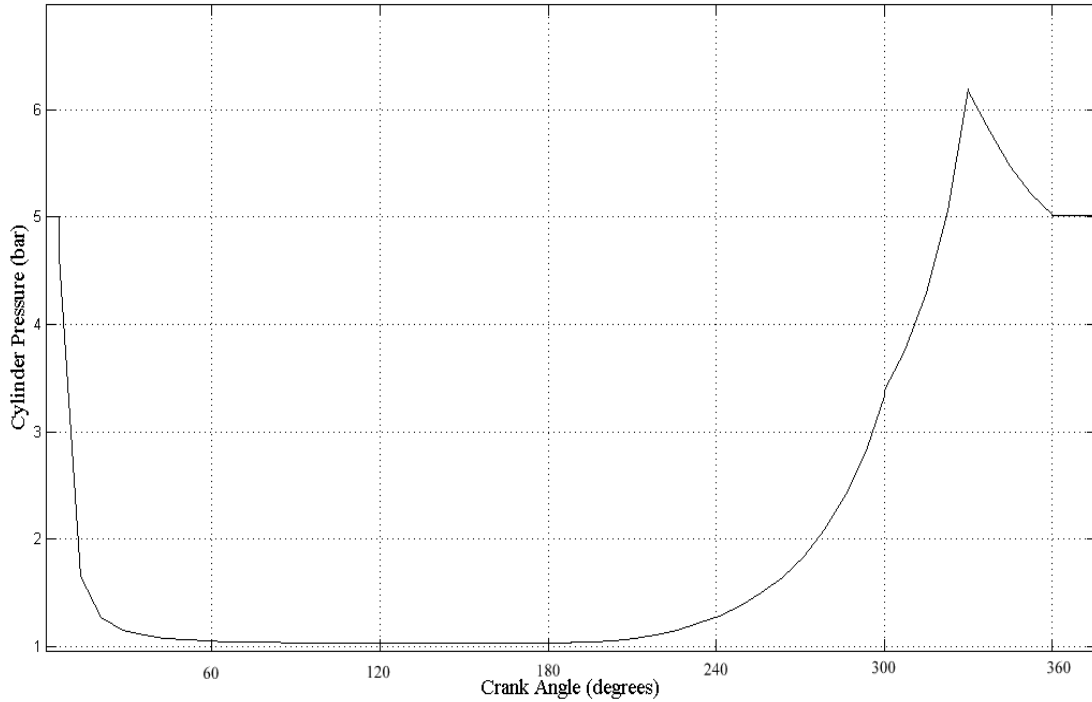
Figure 2.10: Simulated cylinder pressure vs. crankshaft angular rotation for operating condition of 1725 rpm and 17 scfm mass flow rate

The total torque developed by the variable force due to pressure changes and by the variable force due to reciprocating mass of piston cylinder assembly acting on the crankshaft is shown in Figure 2.11. The air pressure inside the piston cylinders creates a dynamic force as a result of the variable torque that is generated on the crankshaft powered by an electrical motor.
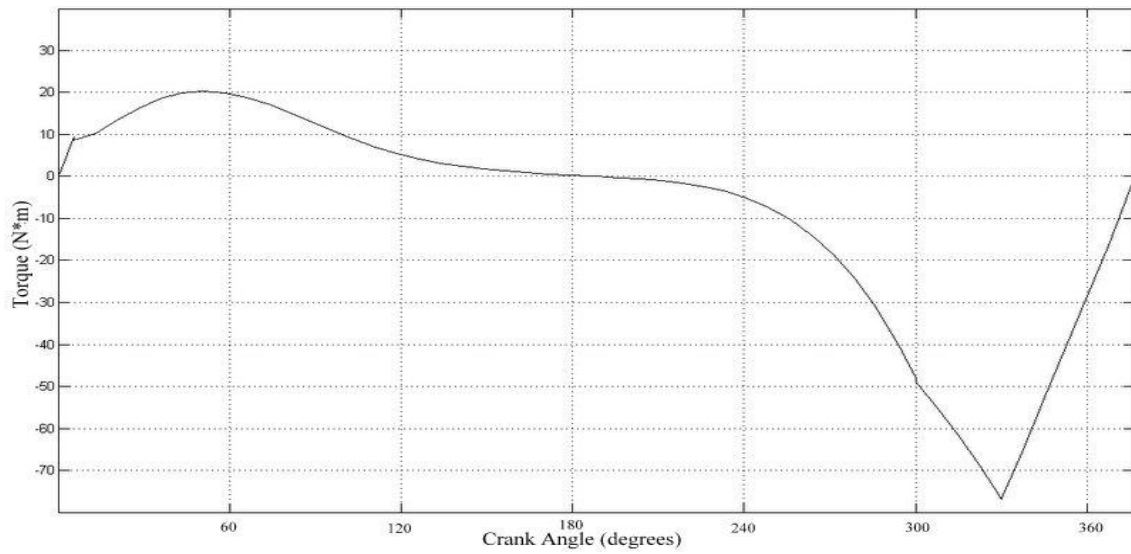
Figure 2.11: Simulated torque vs. crankshaft angular rotation for system operation of 1725 rpm and 17 scfm mass flow rate

Figure 2.12 provides the pressure change in cylinder according to volumetric change in air inside the cylinder. The air compressor with 7HP (5.2kW) electrical motor can be run for approximately 5 hours with the power available from one day operation of the solar panels which will provide 144 m^3 of air for storage at 175 psi (1.2 MPa).
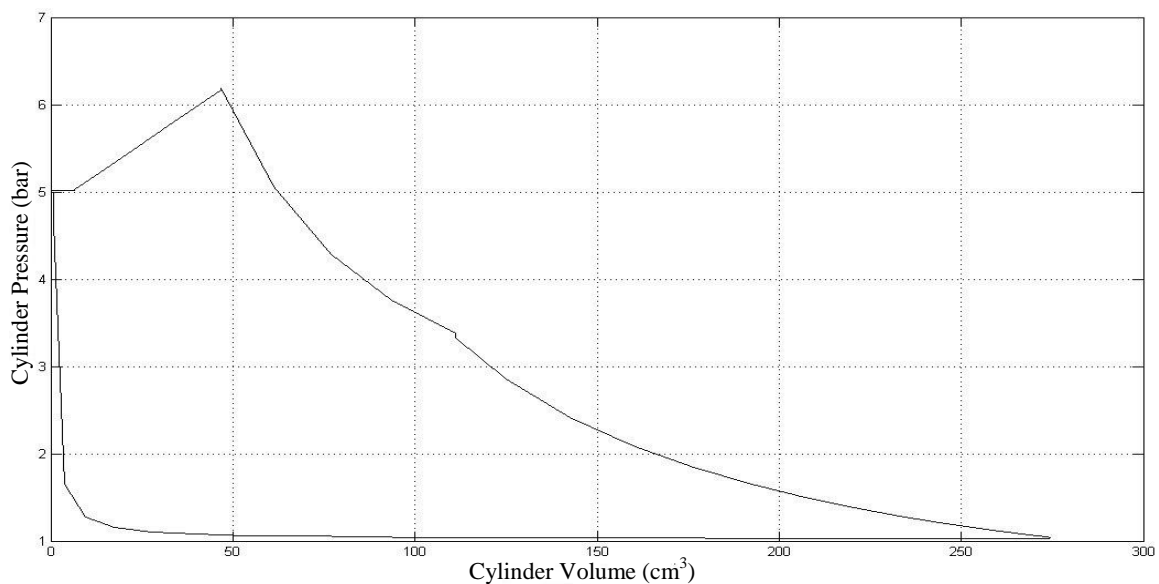
Figure 2.12: Simulated cylinder volume vs. cylinder pressure characteristics at air compressor operating case of 1725 rpm and 17 scfm mass flow rate

A pressure vessel of volume $V_a = 144\text{m}^3$ is considered as an accumulator for the compressed air. The air mass stored in the storage tank is approximately 1108 kg. The air density at 175 psi pressure and 585 K temperature is 7.7 kg/m^3. Figure 2.13 predicts the time required to fill this storage tank at the desired pressure level; approximately t = 4.5 hours to reach a $P_o = 4$ bar tank pressure.
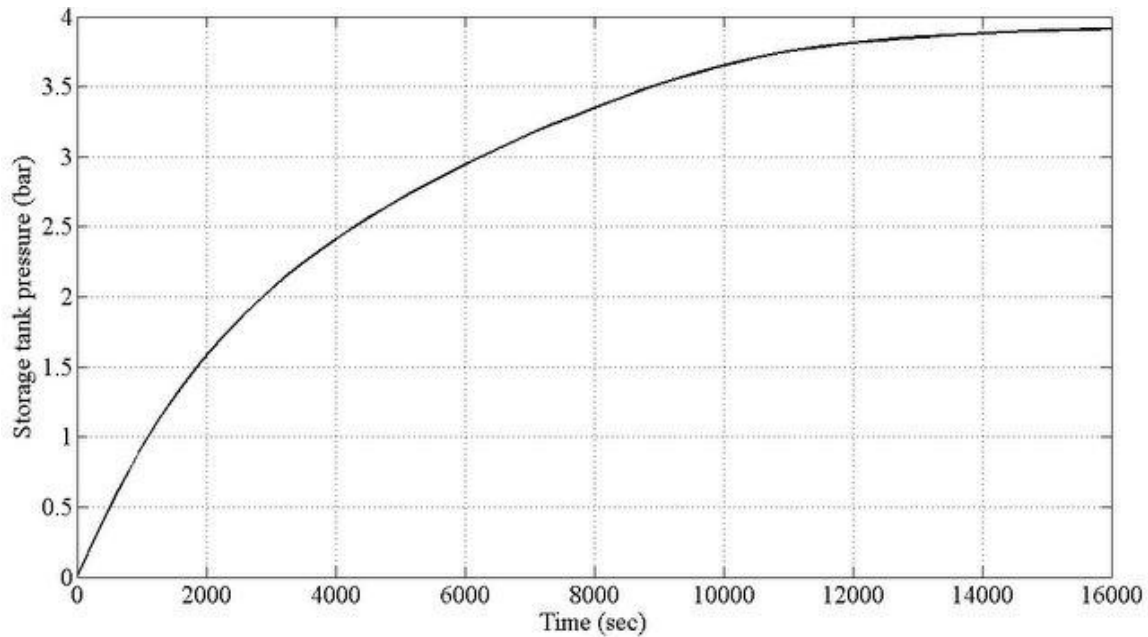
Figure 2.13: Simulated air storage tank pressure rise vs. fill up time for 17 scfm volume flow rate

Microturbine

The power vs. mass flow rate characteristics for a Capstone C30 microturbine fueled with a mixture of gaseous propane and compressed air from the storage tank as displayed in Figure 2.14. The appropriate selection of a mass flow rate and an air/fuel ratio is required to achieve the maximum efficiency for the gas turbine cycle. Three different air/fuel ratios 100, 105.2, and 111.1 have been selected (Cohen *et al.,* 1996, page 59, Figure 2.15, Rahman *et al.,* 2011). As expected, the Capstone C30 microturbine

36

generated approximately $E_e = 50.84$ kW·hr at $\dot{m}_g = 0.31$ kg/s mass flow. The air/fuel ratio

was $A_f = \frac{\dot{m}_a}{\dot{m}_f} = 100$.
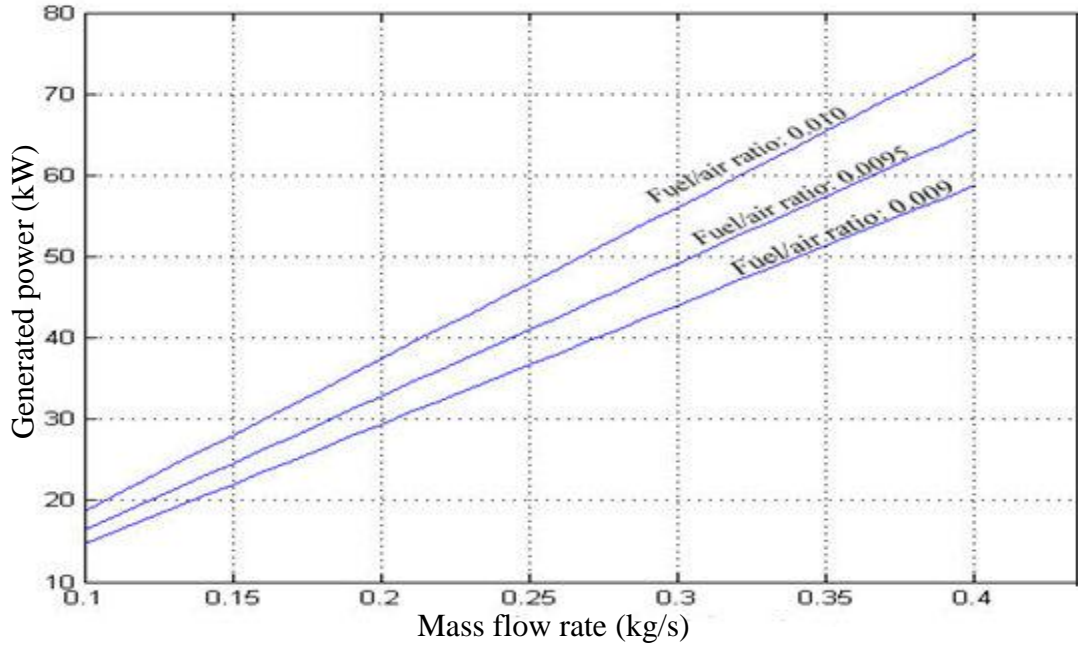
Figure 2:14: Simulated Capstone C30 microturbine generated power vs. mass flow characteristics for three different fuel/air ratios

Case Study

To investigate the feasibility of the energy storage assisted microgrid, different case studies have been conducted as shown in Table 2.4. Assuming an air/fuel ratio of 100, electrical load on turbine shaft of 30 kW, and shaft speed of 96,000 rpm indicated 2.98 N*mm of shaft torque developed in turbine.

Case 1: No energy storage with solar power supplied directly to the electrical grid

Case 2: Microturbine operation for 1 hour without energy storage for electricity

generation

Case 3: Microturbine operation for 1 hour assisted by compressed air energy storage

for electricity generation

Case 4: Solar power generated over 1 day time period is directed to air energy storage

Table 2.4: Comparison of different case studies for microgrid system

Case	System Description	Operating Time (hour)	Turbine Air Flow Rate $\dot{m}_a$ (kg/s)	Turbine Fuel Flow Rate $\dot{m}_f$ (kg/s)	Air Storage Tank Volume (m³)
1	Solar power directly supplied to grid	1.0	Na	Na	Na
2	Microturbine operation (without energy storage) to grid	1.0	0.3069	0.0031	Na
3	Microturbine operation assisted by compressed air energy storage	1.0	0.3069	0.0031	144
4	Solar power to air storage	5.0	0.0603*	Na	144

Case	DC Power Produced (kW)	AC Power Converted (kW)	Electrical Energy Available Over 1 hour (kW·hr)
1	14.95	6.00	6.00
2	na	30.00	30.00
3	na	50.84	50.84
4	14.95	6.00	6.00

*Indicates air mass flow rate for air compressor

* $\dot{m}_{total} = \dot{m}_f + \dot{m}_a$=0.31kg/s

Table 2.5: Comparison of different microgrid components

Component	Power Rating	Time Period	Generated/ Consumed Power
Solar Panels	14.95 kW DC power (≈ 6 kW AC power)	Sunlight available for 5 hours	74.75 kW·hr DC (≈ 30kW·hr AC)
Reciprocating Air Compressor	5.2 kW AC power	5 hours	26 kW·hr AC
Air Storage	5.2 kW AC power	5 hours	26 kW·hr AC
Capstone C30 Microturbine	30 kW AC power	1 hour	30 kW·hr AC

In Case 1, the inconsistency of power availability is a major drawback to use solar power directly without storage. The calculations for Cases 2 and 3 have considered a theoretical fuel/air ration of 0.01, and combustor temperature rise of 410 K. The fuel consumption, F_c, for 1 hour of turbine operation was 11.16 kg for Cases 2 and 3.

$$F_c = \dot{m}_f \times 3600 \text{ sec} \ (\approx 0.0031 \tfrac{kg}{s} \times 3600 \text{ sec} = 11.16 \ kg) \tag{2.25}$$

The air mass flow rate of 0.3069 kg/s could run the turbine for t=3,610 seconds which is approximately 1 hour of turbine operation.

For Case 2, the microturbine provided 30 kW of power using 554,652 KJ/hr (155.3 kW) of fuel energy of gaseous propane. The heat content of gaseous propane is 49,700 KJ/kg so that

$$Q_{g(in)} = 11.16 \tfrac{kg}{hr} \times 49,700 \tfrac{KJ}{kg} = \ 554,652 \ \tfrac{KJ}{hr} \tag{2.26}$$

The energy efficiency of the system for Case 2 can be obtained as 19.3% as shown below.

$$System \ efficiency, \ \eta = \tfrac{Electric \ power \ generated}{Chemical \ power \ input} = \left(\tfrac{30 \ kW}{155.3 \ kW}\right) \times 100\% = 19.3\% \tag{2.27}$$

For Case 3, the microturbine could provide 50.84 kW of power using 554,652 KJ/hr (155.3 kW) of fuel energy because the compressed air stored with the use of solar power helps to bypass the built in air compressor of the microturbine assembly. For Case 3, the proposed system utilized 30 kW of solar power as mentioned in Case 4 for air storage in addition to 155.3 kW provided by fuel. The air storage assisted microturbine operation used total of 185.3 kW of power for system output of 50.84 kW which suggests energy efficiency of the system to be 27.4%.

$$System\ efficiency, \eta = \frac{Electric\ power\ generated}{Chemical\ power + Compressed\ air}$$

$$\eta = \left(\frac{50.84}{185.3}\right) \times 100\% = 27.4\ \% \qquad (2.28)$$

Therefore, energy efficiency improvement for Case 3 was 27.4 - 9.3 = 8.1% when compared to Case 2. The Case 4 indicates that the solar power available for 5 hours over a day period could store 144 m^3 of compressed air to assist microturbine operation.

2.5 Summary

A series of mathematical models for photovoltaic module, an air compressor, air storage, and the microturbine representing an electrical microgrid at Clemson University were developed and simulated. The case study conducted has shown that an electrical microgrid coupled with compressed air energy storage can be considered as an instrumental step towards "green" campus. The storage of solar power in form of compressed air can provide continuous air flow for electric power generation during peak power demands. The micro electrical grid on campus can serve as a supplementary source of power to the main grid. The case study has indicated that lower fuel consumption for Capstone C30 microturbine was required when coupled with compressed air storage so the proposed micro electrical grid can help reduce the carbon footprint of Clemson University. The electrical microgrid study presented in this thesis can be extended for wind energy generation instead of solar. The energy storage methods other than compressed air such as fuel cells, batteries and pumped hydro can also be investigated.

CHAPTER 3

THERMODYNAMIC ANALYSIS OF AN ATMOSPHERIC DRIVEN CLOCK WITH
MECHANICAL ESCAPEMENT CONTROLLER – THEORY AND TEST

The classic Atmos mantle clock operates on daily atmospheric differences to power
the escapement. A delicate gear train and verge, with pallet jewels, turn a torsional
pendulum with minimal frictional losses throughout the system. A pair of hands display
the time on a dial in twelve hour increments. In this chapter, an Atmos 540 clock will be
investigated as it offers vivid insight into a mechanical escapement controller integrated
system components, and a "green" power source. The clock design, operation, and
mathematical model representing the energy flow through the system will be presented.
Representative analytical and experimental results will be discussed to demonstrate the
clock's functionality. Finally, the question of whether this clock meets the definition of a
perpetual motion machine will be examined.

3.1 Introduction

The concept of time keeping has existed for many millenniums with the earliest
clocks based on natural occurrences. The monasteries in Europe were cultural, technical,
agricultural, and spiritual complexes during the 13th century. To synchronize the daily
collective prayer times, mechanical weight-driven clocks were introduced to indicate
ringing the bells for prayers (Burke and Ornstein, 1997). One of the goals since the 18th
century has been a perpetual motion clock which does not require winding in any
manner. An interesting development in 1928 was the creation of a "perpetual" clock by
Jean-Leon Reutter (1899-1971), a Neuchatel, Switzerland engineer who graduated from
the Zurich Federal Institute of Technology in 1921 as a mechanical engineer. Atmos

clock production was principally started by Compagnie Générale de Radio, a French firm in 1929. Jaeger-LeCoultre (Le Sentier, Switzerland), a Swiss watch manufacturer developed variants of the Atmos I clock and began production in 1935 (Lebet, 1997). It receives the energy necessary to maintain time by changes in the local atmospheric temperature. The concept of a perpetual motion machine supports the idea to achieve indefinite output with minimum input; however, the Atmos clock confirms to fundamental thermodynamic laws (Wylen and Sonntag, 1978).

By, using a torsion pendulum, which oscillates very slowly about its center of rotation, the clock requires significantly less energy than a clock with an ordinary pendulum. The torsional pendulum is suspended by a very fine Elinvar wire. Elinvar is a steel alloy which is often used to make watch springs because of its linear elasticity characteristics over wide temperature range. Unlike other torsion pendulum clocks which require outside energy sources to wind the main spring, the Atmos clock is kept wound by the movement of its bellows. The bellows contain a gas called Ethyl Chloride, C_2H_5Cl which is colorless and flammable. It has a boiling temperature of 12.3^oC, so at normal room temperature it remains in vapor condition (Martt, 1998). As the surrounding temperature changes it causes the expansion or the contraction of this gas, which provides total linear movement to bellows. The displacement of bellows stores energy in torsional main spring, unwinding of this spring runs the gear train at constant speed and also provides impulses to run the torsional pendulum through clock escapement. The gear train motion and translation of that motion to pendulum via escapement account for most of the power losses in clock mechanism.

The horology enthusiasts have been involved in research related to time keeping devices since 16th century. The early investigations mostly originated from the European countries. Vacheron *et al.* (2000) provided a repair and maintenance guide for the clock. The company literature provides parts information, the Atmos clock operations, and repair guide (Jaeger Le Coultre, 1993). Von Loessl (1928) studied atmospheric influences on clock operations. Moon and Stiefel (2006) of Cornell University performed experiments on clock escapements to understand non-linear characteristics such as noise and vibrations. Lepschy *et al.* (1992) examined Ktesibios water clock, verge and foliot clock, and the Huygens pendulum clock in order to understand feedback control mechanisms for speed control of clocks. Callaway (2004), Paradiso and Starner (2005) have investigated energy harvesting methods for mobile and wireless devices from atmospheric heat, light and human movements. Gordon and Giauque (1948) studied ethyl chloride properties like vapor pressure, heat capacity, and heat of fusion. They collected lot of experimental data and established property values over different conditions. Moline *et al.* (2012) investigated mathematical model for mechanical clock escapement.

This chapter explores the functional significance of the Atmos clock components and also investigates the energy flow through the system. A nonlinear mathematical model of the clock will be created based on science and engineering concepts and will compare the Matlab/Simulink results to the experimental results taken using the Atmos 540 clock as shown in Figure 3.1. Section 3.2 of this chapter explains the Atmos clock components and their operations in detail. Section 3.3 contains mathematical representation of the clock divided into four mechanical subsystems. The numerical and experimental results

44

have been included in Section 3.4. Section 3.5 contains the summary and future research efforts.

Figure 3.1: Atmos 540 clock investigated in this study from the 1984-1989

3.2 Atmos Clock Components & Operation

An overview of the clock's motion works illustrates the mechanical nature of the device. In Figure 3.2, the key parts of an Atmos clock are labeled based on company literature (Fritz, 1992). Table 3.1 offers a summary of these components. The bellows is the single power source for the clock. When the bellows expands and contracts, it displaces a small chain connected to a pulley on the main spring arbor. The pulley is connected to the clock's mainspring so that a one way ratchet only allows spring winding for tension to operate the clock wheels. The wheels turn the hands of the clock and also power the escapement mechanism. The balance wheel turn gives the periodic back and forth movement to the escapement to keep the wheels advancing in equal segments.

Bellows (1)

Return spring (2)
(inside)

Impulse roller (9)

Pallet fork (7)

Elinvar wire (10)
(inside)

Escapement (8)

Small chain (5)

Gear train (6)

Main spring (4)
(inside)

Winding pulley (3)

Support plate (12)

Front plate (12)

Back plate (12)

Pendulum (11)
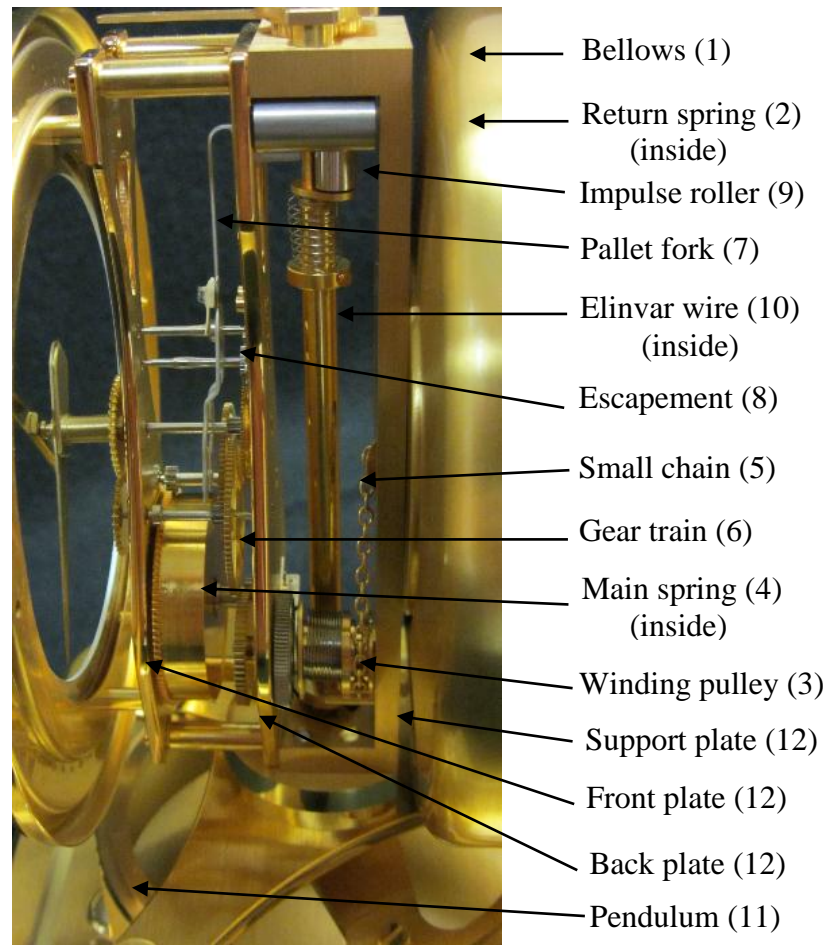
Figure 3.2 Labeled components of the Atmos 540 clock from Figure 3.1

TABLE 3.1
Summary of Atmos 540 clock components and descriptions

No.	Component	Description
1	Bellows	Clock power source with ideal gas
2	Return spring	Spring force opposes bellows expansion; returns to nominal
3	Winding pulley	Converts translational motion into the rotational motion
4	Main spring	Winds itself on bellows contraction; maintains position on expansion
5	Small chain	Chain pulled due to bellows contraction to wind main spring
6	Gear train	Transfers rotational motion from main spring to escape wheel
7	Pallet fork	Impulses balance wheel through impulse roller based on escape wheel
8	Escapement	Converts rotational motion of gear train into pendulum motion
9	Impulse roller	Transfers impulses from escapement to drive Elinvar wire
10	Elinvar wire	Steel alloy wire; hosts pendulum
11	Pendulum	Balance wheel suspended by thin gauge wire
12	Plates	Front, back, and support plates help holding components in place

3.3 Mathematical Model

The mathematical equations which describe the Atmos clock mechanism will be derived using lumped parameter differential equations modeling approach. The energy flow through clock subsystems (Moline *et al.,* 2012) will be examined beginning with the atmospheric changes action as the bellows to the pendulum and clock motion works. Figure 3.3 shows the Atmos clock mechanical system diagram with the subsystems identified that will be modeled.
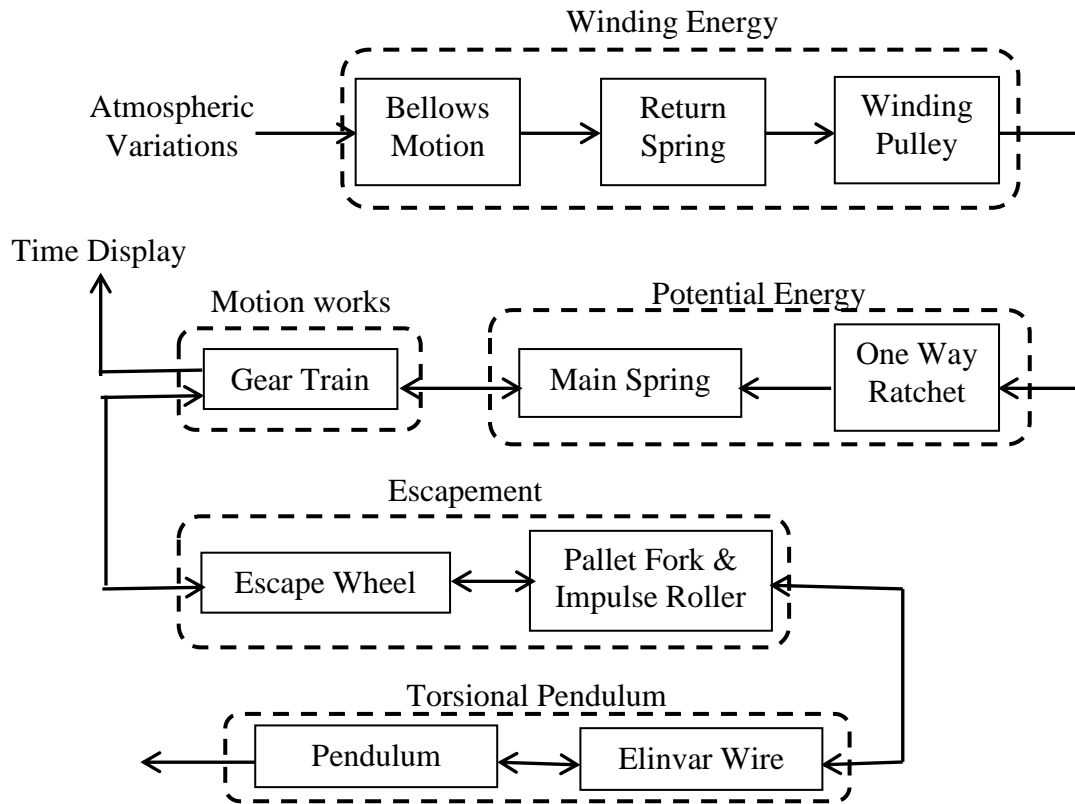
Figure 3.3: Interaction of the five of mechanical subsystems in the Atmos 540 clock to realize uniform characterization of time

Winding Energy Produced by Bellows

The clock harvests the energy needed to wind the mainspring from the thermodynamic behavior of the constrained fluid within the bellows. The ethyl chloride, C_2H_5Cl, has a boiling temperature of 12.3^0C (285.3K) per Figure 3.4. An ambient temperature increase stimulates the evaporation process; above the boiling temperature, the bellows contains both vapor and liquid. When the temperature decreases, the vapor condenses back into a liquid.
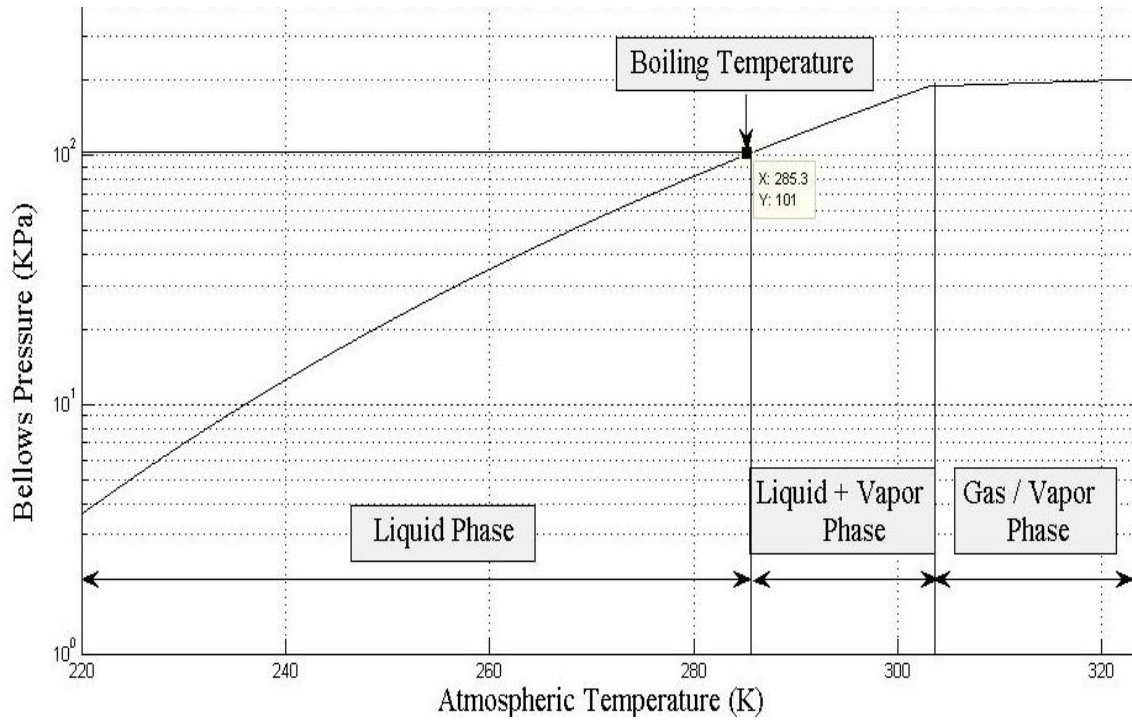
Figure 3.4: Ethyl chloride pressure variation due to ambient temperature change with liquid phase below 285.3K, liquid and vapor phase between 285.3K and 303K, and gas vapor phase above 303K (Gordon and Giauque, 1948)

The vapor pressure inside the bellows due to a change in the atmospheric temperature can be obtained using Antoine's equation (NIST Chemistry, 2012) as

$$\log(p_b) = (a - (b/(T + c)))$$ (3.1)

where p_b is the pressure, a, b, and c are parameters (NIST Chemistry, 2012), T is temperature.

Once all of the liquid is converted into a gas/vapor, the pressure rise inside the bellows can be estimated using the ideal gas law as,

$$p_b v_b = nRT$$ (3.2)

where v_b is the gas volume in the bellows, n is the number of moles of gas found

49

by dividing the gas mass, m_g, by the molecular mass per mole, and R is the ideal gas constant. The term p_b now has units of Pa.

The translational motion of the mechanical bellows is initiated by the expansion of the contained ethyl chloride which produces a driving force, f_b, given as

$$f_b = a_p p_b \tag{3.3}$$

with a_p denoting the bellows end cap surface area.

The bellows driving force will be opposed by the atmospheric pressure acting on bellows surface area, balance spring force, fs, and a spring attached chain force, f_c, which engages the winding pulley and attaches to the one way ratchet as shown in Fig. 3.5. The equation of motion for the bellows end plate, y, can be written using Newton's law as

$$m_b \ddot{y} = f_b - f_a - f_s - f_c \tag{3.4}$$

where m_b is the end plate mass.

The atmospheric force, f_a, acting on bellows surface area can be expressed as

$$f_a = a_p p_a \tag{3.5}$$

where p_a is the local atmospheric pressure.

A stiffer spring return, k_{ec}, acts on the end cap to return the bellows to a contracted position when the temperature decreases so that the spring force becomes

$$f_s = k_{ec} y \tag{3.6}$$

The bellows displacement causes the attached chain to move forward and backward, which rotates the idler pulley and winds the mainspring through the click on the contraction stroke. The force exerted by chain, f_c, can be expressed as

$$f_c = k_c y + f_{click}(\theta_1) \tag{3.7}$$

50

where k_c denotes the small spring attached to the end of the chain and connected to Arbor 1.

The winding pulley is attached to Arbor 0 which also holds the ratchet and main spring. The ratchet is a wheel with saw-shaped teeth that only allows rotation in one direction. A pawl is a pivoted arm that engages the wheel teeth. When the ratchet rotates in one direction, the pawl moves past the ratchet and allows it to rotate. When the ratchet tries to rotate in the other direction, the pawl slips into a tooth on the ratchet wheel preventing motion. For most ratchets, there may be some space between the location of the pawl and the closest tooth of the ratchet. The result is that Arbor 1 may experience a small degree of back spin. The force exerted by the click, f_{click}, will be a function of Arbor 0 angular displacement, θ_0, such that

$$f_{click}(\theta_0) = \left\{ \begin{array}{c} \frac{1}{r_r} \tau_{11};\ \theta_0 > 0 \\ 0\ ;\ \theta_0 \leq 0 \end{array} \right\} \tag{3.8}$$

where $\theta_0 = y/r_p$ with r_p and r_r denoting the winding pulley radius and ratchet wheel radius, respectively. The variable τ_{11} represents the main spring torque
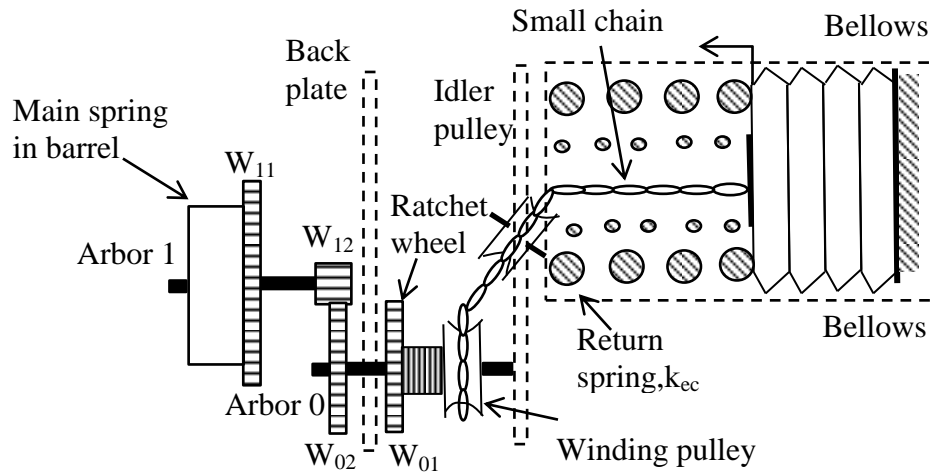
Figure 3.5: Transformation of bellows end cap motion into main spring rotational winding for power generation

Potential Energy of Mainspring

The mainspring in the Atmos clock is a torsion spring composed of thin gauge coiled steel. The inner end of the mainspring is affixed to Arbor 1 which it is wound by the bellows motion induced chain displacement. The outer end of the spring is attached to the barrel wall which houses the spring. The mainspring is maintained by the ratchet and pawl mechanism which keeps the spring from unwinding in an uncontrolled manner. A wound mainspring stores energy which is then slowly released to operate the clock mechanism through the escapement. The drive torque, τ_{11}, produced by the mainspring may be expressed as (Norton, 2000)

$$\tau_{11} = \frac{Eb_{ms}t_{ms}^3(\theta_1 - \theta_{10})}{12L} \tag{3.9}$$

where E is the modulus of elasticity for spring material, b_{ms} is the main spring width, t_{ms} is the main spring thickness, L is the spring length, θ_1 is the angular rotation of Arbor 1, and θ_{10} is the initial angular displacement of this Arbor.

Motion Works

A gear train changes the speed, torque, and/or the direction of rotation for two interfaced rotating shafts with wheels. The gear ratio, R_f, between two intermeshed gears is the ratio of their angular velocities, ω, diameter, D, number of teeth, N, and torque, τ, so that

$$R_f = \frac{\omega_{in}}{\omega_{out}} = \frac{D_{out}}{D_{in}} = \frac{N_{out}}{N_{in}} = \frac{\tau_{out}}{\tau_{in}} \tag{3.10}$$

where the subscripts, in, and out, denote input and output motions. For this application, Figure 3.6 offers a representation of the gear train in the timekeeping mechanism with the six arbors supported by two metal plates.
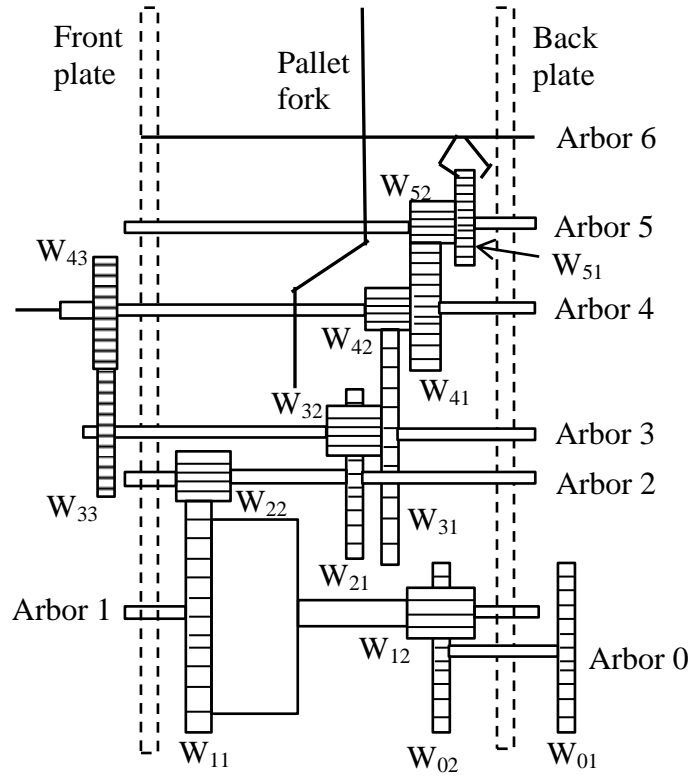
Figure 3.6: Atmos 540 clock motion works with labeled arbors and wheels

Gears which share the same arbor will have the same angular velocity. The exception to this statement is the hour gear which rotates around the same axis as the minute gear on Arbor 4, but the hour gear receives its input from the gear below it on Arbor 3. The number of teeth for each wheel and pinion is listed in Table 3.2. The overall gear ratio for the escapement, R_e, the hour hand, R_h, and the minute hand, R_m, can be calculated as,

$$R_e = \left(\frac{N_{22}}{N_{11}}\right)\left(\frac{N_{32}}{N_{21}}\right)\left(\frac{N_{42}}{N_{31}}\right)\left(\frac{N_{52}}{N_{41}}\right)\left(\frac{1}{N_{51}}\right) \tag{3.11}$$

$$R_h = \left(\frac{N_{22}}{N_{11}}\right)\left(\frac{N_{32}}{N_{21}}\right)\left(\frac{N_{43}}{N_{33}}\right) \tag{3.12}$$

$$R_m = \left(\frac{N_{22}}{N_{11}}\right)\left(\frac{N_{32}}{N_{21}}\right)\left(\frac{N_{42}}{N_{31}}\right) \tag{3.13}$$

As expected, a 12:1 ratio exists between the minute and hour hands (i.e. minute hand rotates 12 times for one full rotation of hour hand). Similarly, the 60:1 ration between the escapement and minute hand reflects the fact that the pendulum period is 60 seconds so it makes 60 revolutions per hour. If the twin pallets are considered, then this rate will be halved.

TABLE 3.2
Summary of Atmos 540 clock motion works

Arbor	Wheel	Symbol	N	D (mm)	Weight (gm)
0	1	W_{01}	84	18.90	-
	2	W_{02}	55	18.50	
1	1	W_{11}	103	37.03	16.0
	2	W_{12}	18	6.20	
2	1	W_{21}	87	25.07	2.1
	2	W_{22}	11	4.28	
3	1	W_{31}	87	25.07	2.6
	2	W_{32}	10	3.07	
	3	W_{33}	29	12.40	
4	1	W_{41}	80	18.21	3.6
	2	W_{42}	10	3.09	
	3	W_{41}	40	16.75	
5	1	W_{51}	15	8.95	0.3
	2	W_{52}	20	4.70	

Escapement

The rotational motion from the gear train is transferred to the pendulum's oscillatory motion by the escapement. The pallet fork keeps the escape wheel from rotating uncontrollably; the twin pallets interact with the escape wheel teeth and transfer the force to the impulse roller.

The force exerted on the Arbor 6 pallets can be determined, refer to Figure 3.7(a), as

$$f_{pallet} = f_{tooth}/\tan\theta \tag{3.14}$$

where f_{pallet} is the force exerted by pallets, $f_{tooth}=\tau_{51}/r_{51}$ with $\tau_{51} = R_e\tau_{11}$ is the escape wheel tooth generated force on the pallet jewels, and θ is the angle between the pallet force vector and the normal force, f_n, at the point of contact.

The force transferred to the impulse roller from pallets, f_{roller}, can be given as

$$f_{roller} = \left(\frac{r_{61}}{r_{62}}\right)f_{pallet} \tag{3.15}$$

where r_{61} is radius of rotation for pallets, and r_{62} is distance from the center of Arbor 6 (point P) to point Q in Figure 3.7(b).

The position vector $\bar{r}_{62}$ from P to Q may be denoted as

$$\bar{r}_{62} = a_1\hat{\imath} + b_1\hat{\jmath} + c_1\hat{k}, \ |r_{62}|=\sqrt{a_1^2 + b_1^2 + c_1^2} \tag{3.16}$$

where a_1, b_1, and c_1 are the x, y, z coordinates of the pallet fork or lever arm.

The roller torque, τ_{roller}, exerted on the pendulum through the impulse roller can be expressed as

$$\tau_{roller} = (r_7\cos\theta_{iR})f_{roller} \tag{3.17}$$

where r_7 is the impulse roller rotation radius and θ_{iR} is the angle of the impulse roller rotation.

The last equation may be rewritten by substituting (3.14) and (3.15) into (3.17) so that

$$\tau_{roller} = \frac{r_{61}r_7\cos\theta}{r_{51}r_{62}\tan\theta_{iR}}\tau_{51} \tag{3.18}$$

where $\theta_{iR} = \begin{cases} \theta_p & ;|\theta_p| < 120° \\ 120sgn(\theta_p) & ;|\theta_p| \geq 120° \end{cases}$ with θ_p representing the pendulum angle rotation.
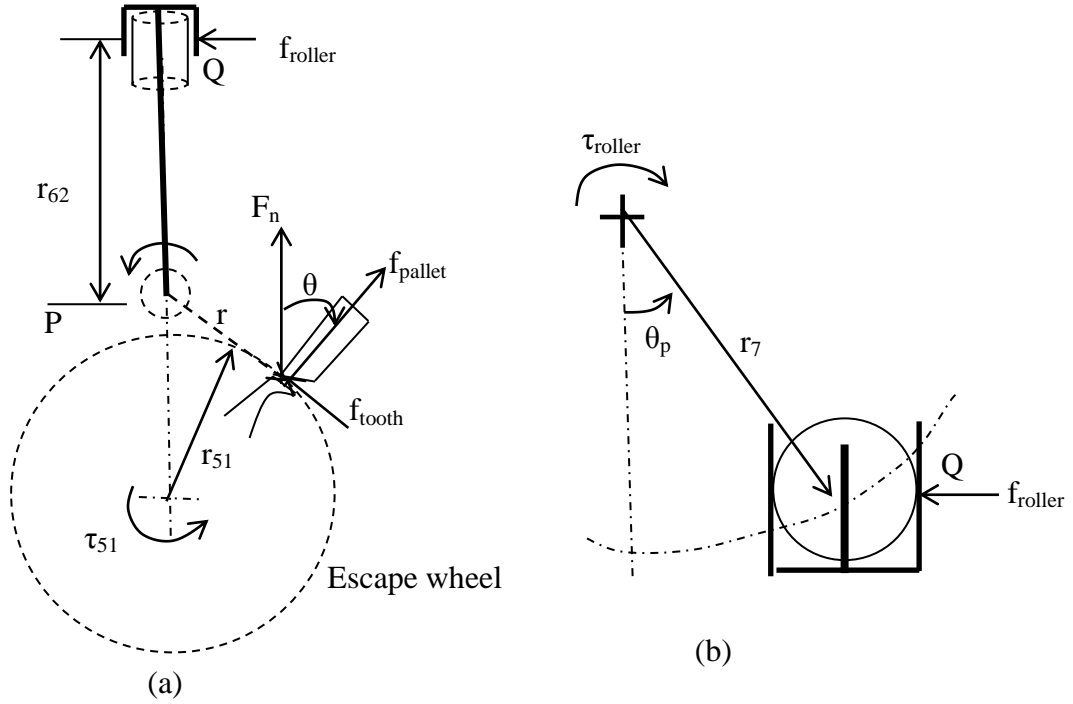
Figure 3.7: Escapement and impulse roller geometry (a) front, and (b) top views for two different rotational positions

Torsional Pendulum

The pendulum in the Atmos clock is a torsion pendulum. A torsion pendulum vibrates by rotating back and forth about its axis. The impulse roller receives two torque impulses in opposite directions from the crutch at interval of every 30 seconds. The differential equation of motion for the torsion pendulum becomes

$$
J\frac{d^2\theta_p}{dt^2} + B\frac{d\theta_p}{dt} + C\theta_p = \left\{ \begin{array}{l} \tau = +\ \tau_{\text{roller}}\ ;\ 90° < \theta < 120° \\[2mm] \tau = 0 \qquad ;\ \text{otherwise} \\[2mm] \tau = -\ \tau_{\text{roller}}\ ;\ -90° < \theta < -120° \end{array} \right\} \tag{3.19}
$$

where J is torsional pendulum inertia given by $J = \frac{1}{2}mr_{tp}{}^2$, B is the damping coefficient, and C is the Elinvar wire stiffness.

3.4 Numerical and Experimental Results

The real time data has been gathered using two attached sensors and Labview hardware instrumentation. The Labview environment as shown in Figure 3.8 monitors pendulum, crutches and clock hand motion under controlled atmospheric conditions in mechatronics laboratory. The numerical results are obtained with Matlab/Simulink models for the clock subsystems of Figure 3.3. Table 3.3 lists the model parameters used to simulate the clock mechanism.

Clock Instrumentation

The linear output magnetic field (Hall Effect) sensor AD22151 was used to observe the crutch motion. A high resolution magnetic angular position sensor, APS00B, captured the pendulum motion and minute hand motions. The sensor outputs were collected and displayed in LABVIEW using a simultaneous sampling multifunction DAQ (NI PCI-6143) kit.
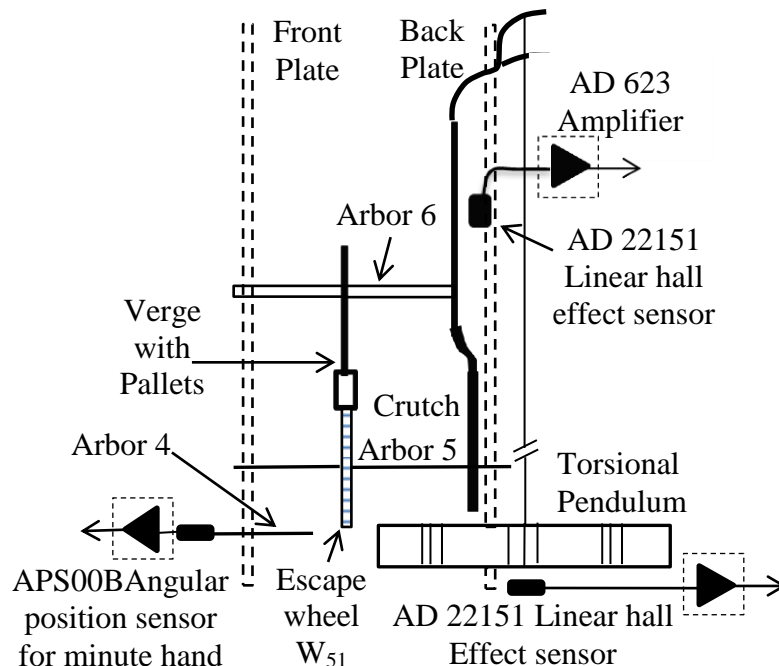
Figure 3.8: Side view of clock escapement with attached instrumentation to measure the hand and pendulum motions

TABLE 3.3
Summary of Atmos clock model parameters

Symbol	Value	Units	Symbol	Value	Units
a	4.1618	bar	p_a	1	atm
a_p	28.3	cm^2	r_p	4	mm
a_1	28	mm	r_r	9.45	mm
b	1052.82	bar*K	r_{tp}	40	mm
b_{ms}	5.97	mm	r_{51}	4.48	mm
b_1	3.6	mm	r_{61}	2.39	mm
B	15	N*s/mm	r_{62}	31.6	mm
c	-32.078	K	r_7	4.355	mm
c_1	14.2	mm	R	8.314	J/mole*K
C	2	N/mm	R_e	1/42,524	-
E	206,843	MPa	R_h	1/59.06	-
J	400	$N*mm^2$	R_m	1/708.73	-
k_c	0.1	N*mm	t_{ms}	0.08	mm
k_{ec}	162.79	N*mm	v_b	0.00027	m^3
L	1,100	mm	θ_p	$\pi/4$	rad
m_b	0.2039	kg	θ_{10}	0	rad
m_g	1.39	g	τ_{11}	0.0594	N*mm
M	64.514	g/mole	τ_{51}	1.4×10^{-6}	N*mm
n	0.0288	-			

Discussion of Results

The bellows response to the surrounding temperature changes was measured experimentaly. The temperature range for both the experiment and simulation was 272 - 295K over a 20 minutes time period. No external loading was applied except from the weight of a thin metal plate to improve vertical position viewing. The experimental and simulated results show close proximity to each other as shown in Figure 3.9.
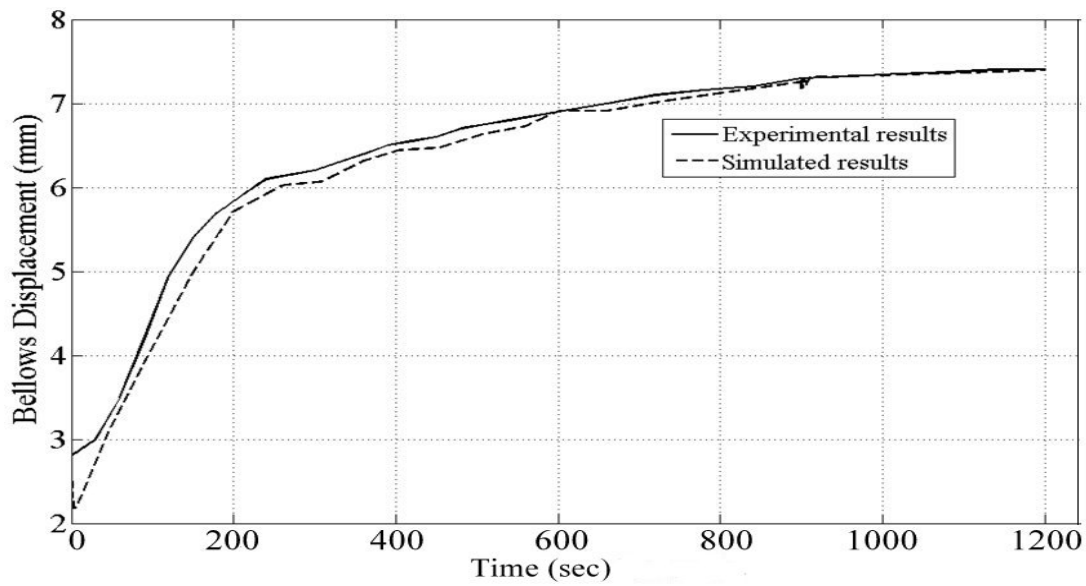
Figure 3.9: Experimental and simulated bellows displacement response

Figure 3.10 shows gradual increment in minute hand angular position calibrated in terms of voltages. The minute hand ticks two times per minute providing 3° of rotation for each tick of the clock. Notice that each tick of the minute hand is of equal magnitude which indicates high accuracy.
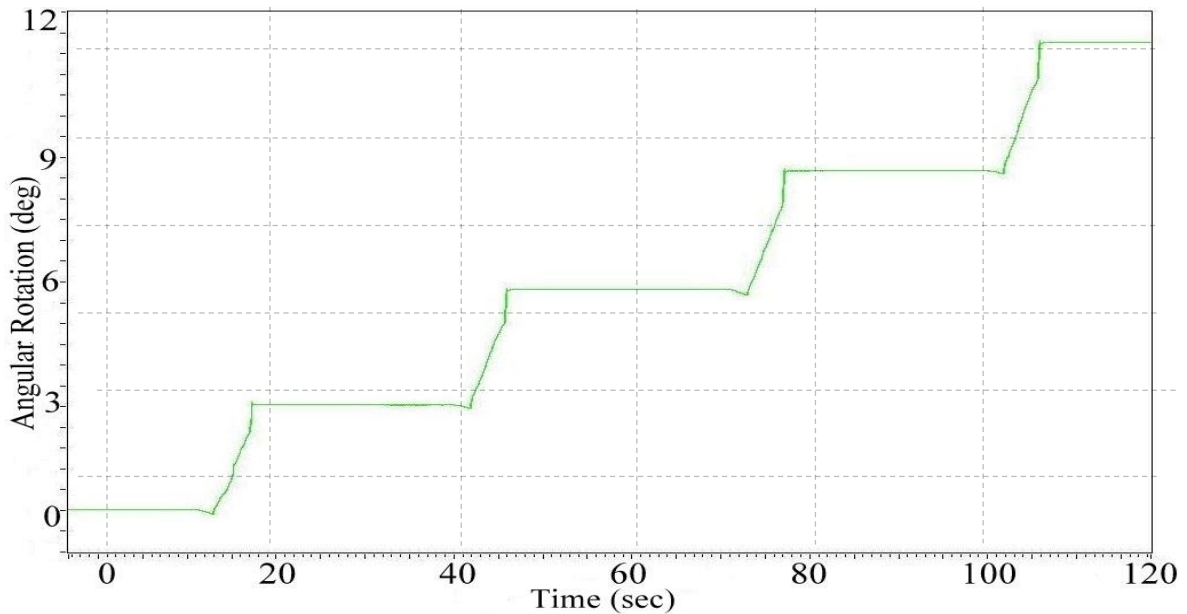
Figure 3.10: Experimental minute hand angular motion captured by the angular position sensor for Atmos 540 clock

The crutch motion captured with high resolution magnetic angular position sensor has been shown in Figure 3.11. The crutch remains on 'hold' position for significant portion of time and moves in one direction for small span of time every 30 seconds which is evident in Figure 3.11 and it can also be derived from the gear ratio values presented in Table 3.2. This event occurs twice per minute, the crutch moves in opposite direction on second time as shown in Figure 3.11. Notice the recoil of the minute hand (which is geared directly to the escape wheel) just as the crutch starts to move, then the jump of almost equal magnitude at the start of the impulse and finally the large jump (free spin) just before the crutch stops.
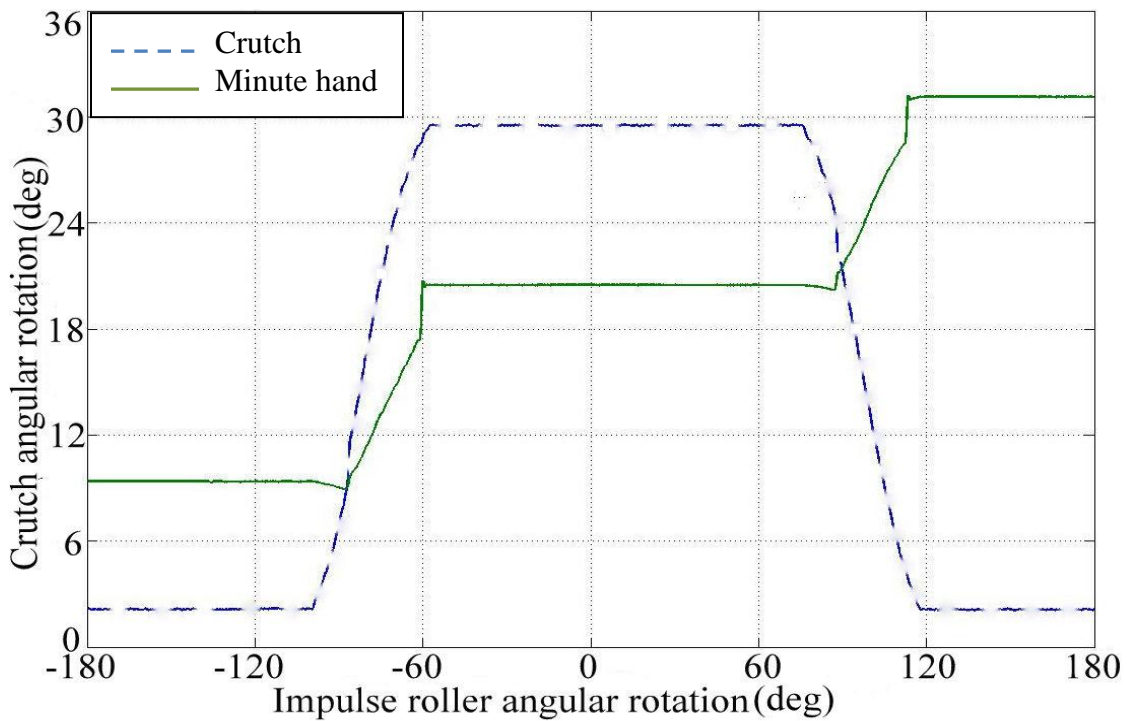
Figure 3.11: Experimental crutch and minute hand angular displacement measured over a one minute time period

The crutch provides two torque impulses in opposite direction to the impulse roller in order to rotate torsional pendulum as shown in Figure 3.11. The torsional pendulum rotational motion was obtained with the use of similar angular position sensor used to capture minute hand motion. The pendulum completes two rotations per minute as shown in Figure 3.12. It is apparent that simulated results closely follow experimental data.
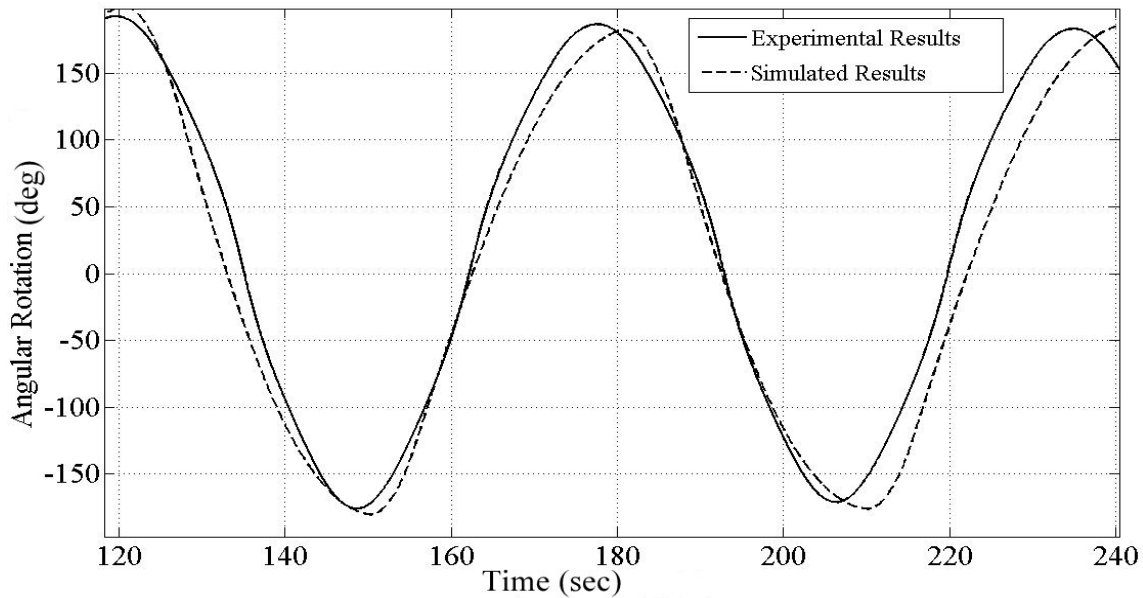
Figure 3.12: Torsional pendulum motion experimental and simulated data

3.5 Summary

The simulated data indicated the total linear movement of approximately 6 mm for the bellows over a 24 hour time period. The temperature variations were provided randomly in the range of 290-292K (refer Figure F.10) which are very close to the real time room temperature fluctuations. The displacement of the bellows could store nearly 57e-03J or 0.67e-06 watts of potential energy in the clock main spring. The volume of the Ethyl Chloride gas contained in the bellows was 27e-05 m^3, and the energy density value for the Atmos clock bellows was 2.48e-03 w/m^3.

The mathematical model developed in paper can be useful to understand clock operation. System power losses due to friction and uncertainty have been minimized with the use of delicate and carefully manufactured gear train. The escapement mechanism can be investigated in more detail for further studies. Torsional pendulum used is more efficient than simple vertical hung pendulum which helps to minimize power consumption. The movement is approximately 75 years (1935-2012) old so it attributes good design. The Atmos clock provides lessons for capturing mechanical power from atmospheric changes using gas to drive mechanical system. The Atmos 540 clock can be classified as "pseudo perpetual motion" machine rather than perfectly perpetual motion machine.

CHAPTER FOUR

CONCLUSION AND RECOMMENDATIONS

A major challenge for contemporary society is to harness alternative energy in a cheap and efficient manner. This chapter presents a succinct review of the outcomes and the recommendations for two alternative energy based technologies: an electrical microgrid, and an Atmos clock. The growing demand for clean electrical and mechanical power can be countered with the help of a localized power generation facility, also known as an electrical microgrid. In this research thesis, the electrical and mechanical subsystems of a microgrid have been mathematically modeled and analyzed numerically for successful electrical microgrid establishment at Clemson University. A comparative case study for three different operating conditions has been conducted to identify feasibility and fuel consumption savings for the project. Similarly, the Atmos clock has been studied to understand energy flow through its subsystems. The representative mathematical model for each subsystem is created, simulated, and compared with experimental outcomes. The commonality of both research projects is usage of clean energy for power production. The microgrid generates power to be utilized by external loads while the atmospheric driven clock fulfills its own power requirement.

4.1 Electrical Microgrid Study

A hypothetical electrical microgrid featuring Kyocera solar modules, a two stage reciprocating air compressor with air storage, and a Capstone C30 microturbine was proposed for Clemson University. The first component of the proposed microgrid was photovoltaics module KC130GT installed on Fluor Daniel Engineering Innovation

Building. The generalized and simplified mathematical models have been developed with the help of previous works to determine the electrical characteristics such as voltage-current and voltage-power for the solar panels. The maximum power point (MPP) can be estimated from these characteristics by drawing a rectangle from a point on the curve, the rectangle with maximum area would provide peak power value with corresponding current and voltage values. The studied photovoltaic module has shown a capability of producing 15 kW of DC power at full solar insolation of 1000 w/m^2. The Sunny Boy (SB6000U) electrical inverter has been coupled with the panels, which provided up to 6 kW of AC power. The maximum voltage and current values for the solar module were observed to be 17.5 volts and 7.3 Amps respectively. The numerical simulations were prepared according to the mathematical equations to analyze a variety of photovoltaic modules with different operating parameters. It is important to mention that PV characteristics observed here were based on standard operating conditions, so they may vary somewhat for real world operations.

The electrical motor (5.2 kW) operated, double stage reciprocating air compressor, was the second component of the microgrid following solar panel. The mathematical model, based on prevalent dynamic equations, has been presented and simulated in Matlab/Simulink to analyze the inter-stage pressures for a multistage compression process and to predict the pressure ripples during different stages of compression. The model also calculated the force generated in each piston cylinder and the resultant torque acting on the compressor shaft. Based on the swept volume and revolutions of the cylinders, the air mass flow rate was derived. The flow rate and pressure values helped in

the selection and sizing of the air receiver (storage tank). The results have shown that using 30 kW of AC solar power, 1108 kg of air at 1.2 MPa pressure can be stored for subsequent turbine operation. The proposed model can be improved by considering the air humidity which was ignored.

In the last segment, the Capstone C30 microturbine system has been modeled to analyze the power output and specific fuel consumption. The nonlinear thermodynamic mathematical equations have been used from the gas turbine literatures, and a Matlab/Simulink model has been prepared. The comparison between gas turbine operation with compressed air storage and without air storage has shown that use of pre-compressed air eliminates power utilized to run the built in microturbine compressor. This study has indicated that a Capstone C30 microturbine, capable of delivering 30 kW of power, required 11.16 kg of gaseous propane to produce 30 kW·hr of energy when operated without compressed air storage. On the other hand, the same microturbine assisted by compressed air storage could produce 50.84 kW·hr of energy for same amount of fuel consumption. The Capstone C30 microturbine used a lower fuel/air ratio of 0.01 as it promotes lean combustion.

Several suggestions related to the microgrid may be proposed:

- An electrical microgrid has been investigated based on simulated results for this thesis. An experimental system might be build which integrates the solar power, air compressor, pneumatic storage, and turbine generation to explore system behavior.

- Compressed Air Energy Storage (CAES) technology was selected for this thesis. Other energy storage technologies such as pumped hydro storage, fuel cells, batteries, and flywheels can be investigated in conjunction with solar and/or wind power to identify the best possible combination of technologies.

- Clean energy sources other than solar such as wind or geothermal might be investigated for electric power generation.

- A double stage reciprocating air compressor has been studied for this thesis. Other types of air compressors such as a centrifugal and rotary screw can be investigated for efficiency improvements.

- The electrical microgrid study conducted for this can be extended to quantify the emission reductions using technologies capable of modeling air pollution or carbon footprint.

4.2 Atmospheric Driven Thermodynamic Mechanical Clock Study

In this thesis, a classic Atmos 540 mantle clock has been investigated as it represents an excellent example of atmospheric energy scavenging. A detailed review has been provided to understand the functionality of the clock components. The mathematical equations describing the Atmos clock mechanism and operations have been derived using a lumped parameter modeling approach. To investigate energy flow in the system, the Atmos clock mechanism has been divided into five subsystems: the winding energy produced by bellows, potential energy of the mainspring, motion works, escapement mechanism, and torsional pendulum. The derived mathematical models for each of the subsystems were simulated using the Matlab/Simulink tool set. The simulated results

have been validated with the experimental results collected using three sensors synchronized in the LabVIEW environment of National Instruments.

The first subsystem for the Atmos clock was identified as the winding energy produced by the bellows filled with Ethyl Chloride gas. To simulate the bellows, the physical properties and the characteristics of Ethyl Chloride were studied. The study revealed interesting facts about Ethyl Chloride including a boiling temperature of 12.3°C, so it can be found in liquid, vapor, or liquid and vapor phase over a normal room temperature range. Ethyl Chloride vapor pressure changes were studied over a temperature range of 220-320K; below 292K, the pressure inside the bellows changes significantly for a small change in atmospheric temperature which provides linear bellows movement. For temperatures above 292K, less bellows motion was observed due to the vapor pressure inside. The results have shown that the total linear motion of the bellows wound the mainspring nearly 6 mm over 24 hour time period for a temperature range of 290-292K which could store 57e-03 J of energy in the clock main spring. The bellows physical measurements were collected manually and presented in Appendices C and D.

The second atmos clock subsystem was identified as the potential energy produced by the torsional mainspring. The bellows linear movement provided winding of this mainspring through a small chain attached to the winding pulley. A pawl and ratchet mechanism was identified and simulated as a one-way clutch as it stops the mainspring from unwinding. The maximum potential energy of the mainspring was 57.5e-03J or 0.67e-06 watts over a 24-hour time period. The torsional mainspring measurements were

collected and the modulus of elasticity for the spring was considered assuming that the sparing material was stainless steel. The clock motion works was identified and investigated in detail as the third subsystem of the Atmos clock. The measurements for the wheels such as number of teeth, diameters, and weights were collected. The gear ratios for minute hand, hour hand, and escapement were 1.41e-03, 1.69e-02, and 2.35e-05 respectively. The gathered data has shown a 12:1 ratio between the minute and hour hands and a 60:1 ratio between the escapement and the minute hand as expected.

The escapement mechanism, the fourth subsystem, acts as a torque transferring link between the motion works and the torsional pendulum. The crutch motion was observed using a high resolution magnetic angular position sensor which indicated a movement of the crutch every 30 seconds in opposite directions; the crutch remains in a 'hold' position for a large portion of time (22 sec). Representative mathematical equations were derived which established relationships between torque available at the impulse roller and the torque at Arbor 5 of the motion works. Finally, the torsional pendulum was the last subsystem for energy flow. The differential equation for torsional pendulum motion was simulated using Simulink. The experimental and simulated results were in close agreements with two complete rotations for the pendulum per minute. This research has indicated that the Atmos 540 clock is an exceptional example of thermodynamic, self-winding, mechanically controlled, energy harvesting device.

Several suggestions related to the Atmos clock study may be proposed:

- Those gases with high vapor pressures and suitable temperature range other than Ethyl Chloride (C_2H_5Cl) might be used to fill the Atmos clock bellows, and the linear motion can be observed for improvement in energy output.

- An experimental platform can be fabricated to investigate the displacement of the bellows under different temperature and pressure operating conditions to characterize the bellows movement.

- The Atmos clock study, which is a thermo-mechanical way of energy scavenging, can be extended to other alternative mechanical energy technologies such as piezoelectric (PZT) energy harvesting.

- An evaluation can be performed for the role of friction with mechanical systems and the limitations associated with motion.

- The mathematical models presented here for the different subsystems of the Atmos clock can be refined.

APPENDICES

Appendix A: Microgrid Subsystems Simulink Models

Appendix A contains the Simulink models for the microgrid subsystems: solar module, reciprocating air compressor, air storage tank, and microturbine as represented in Figures A.1 to A.4.
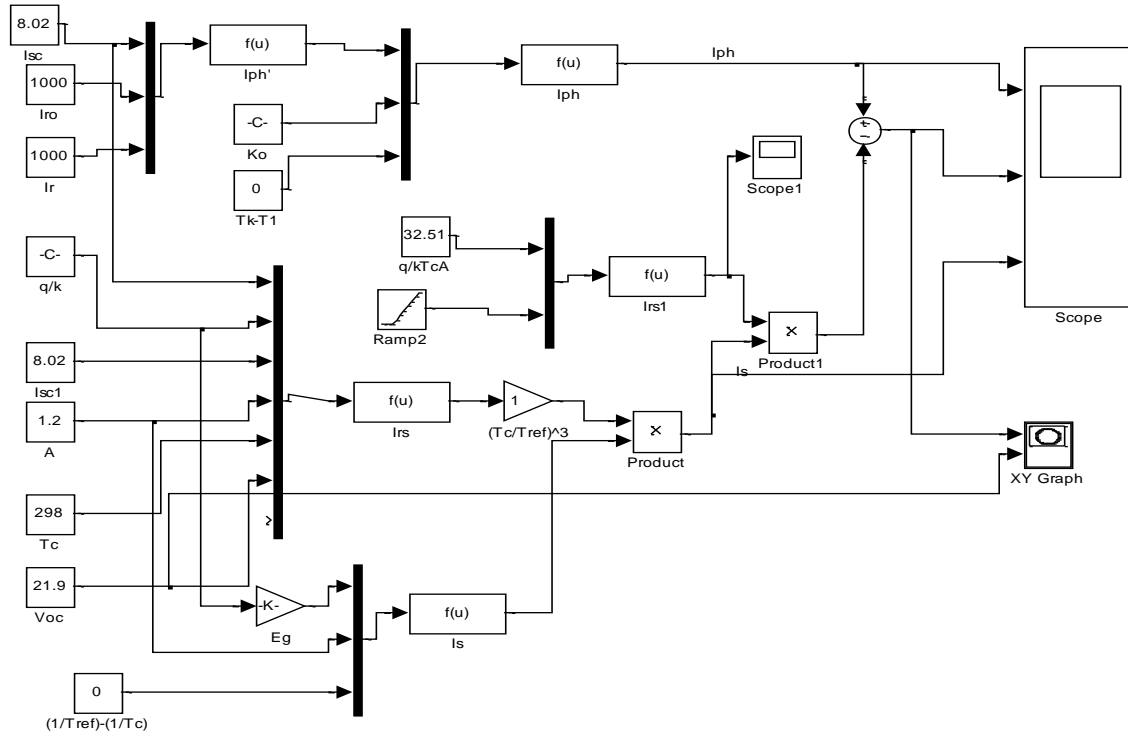

Figure A.1: Simulink model for solar cell module KC130GT

Figure A.2: Simulink model for reciprocating air compressor

Figure A.3: Simulink model for air storage tank

Figure A.4: Simulink model for Capstone C30 microturbine

Appendix B: Microgrid Matlab Codes for Data Plotting

Appendix B provides the Matlab codes for data plotting with parameter values used

for some of the microgrid simulations.

%%%%%%%%Solar cell current and voltage values calculations%%%%%%%%%

```
k = 1.381e-23; % Boltzmann constant, (J/K)
q=1.602e-19;   % Electronic charge, (C)
A= 1.2; % Diode quality facror
Eg=1.12;%Band gap voltage,(V)
Tc= 320;% TaC Temperature for which values have to be found (K)
Voc=21.9; %Open circuit voltage, (V)
Isc=8.02;%Short circuit current, (Amp)
Ir0=1000;% Irradiance, (W/m^2)
Tref=298; %Reference temperature (K)
Ir=1000;%Actual Irradiance (W/m^2)

a=(q/k)/A;
N=115;% no. of panels
V=0:0.1:21.9;
% Calculation of Iph
Iph=Isc.*(Ir0/Ir)+(Ki.*(Tc-Tref));

% Calculation of reverse saturation current
Irs=Isc/ (exp(Voc.*a/Tc)-1);

% Calculation of I

I=Iph-1.*(Isc.*(exp(V.*a./Tc./N)-1)./ (exp(Voc.*a/Tc./N)-1));
P=V.*I;
Pmax=max(P)

% Calculation of Saturation cuurent

Is=(Irs.*(Tc./Tref).^3)*(a*Eg*((1./Tref)-(1./Tc)));

% Results
figure(1),plot(V,I,'black');
grid;
hold on;
figure(2),plot(V,P,'black');
grid;
```

```matlab
hold on;

Ir=800;
Iph=Isc.*(Ir/Ir0)+(Ki.*(Tc-Tref));
I=Iph-1.1.*(Isc.*(exp(V.*a./Tc./N)-1)./ (exp(Voc.*a/Tc./N)-1));
P=V.*I;
figure(1),plot(V,I,'black');
hold on;
figure(2),plot(V,P,'black');
hold on;

Ir=600;
Iph=Isc.*(Ir/Ir0)+(Ki.*(Tc-Tref));
I=Iph-1.05.*(Isc.*(exp(V.*a./Tc./N)-1)./ (exp(Voc.*a/Tc./N)-1));
P=V.*I;
figure(1),plot(V,I,'black');
figure(2),plot(V,P,'black');

Ir=400;
Iph=Isc.*(Ir/Ir0)+(Ki.*(Tc-Tref));
I=Iph-1.05.*(Isc.*(exp(V.*a./Tc./N)-1)./ (exp(Voc.*a/Tc./N)-1));
P=V.*I;
figure(1),plot(V,I,'black');
figure(2),plot(V,P,'black');


%%%%%Capstone C30 microturbine mass flow rate vs. fuel/air ratio plotting %%%%%

% The microturbine C30 plots for fuel/air ratios 0.010, 0.012, and 0.014.
% the mass flow rate varies from 0.1 to 0.4 kg/s
% a=y-1/y %specific heat ratio
%x=t3-t4 (turbine work formula)

% case 1: Af=0.01, combustor temp. rise :408K
a=0.25;
p3=4; % turbine inlet pressure (bar)
p4=1; % turbine exhaust pressure (bar)
b=4; %p3/p4
t3=708; % inlet temp (K)
nt=0.95; % isrntropic eff.
Cpg =1.147; %specific heat
mf = 0.1:0.01:0.4; % mass fuel rate
x= nt*Cpg*t3*(1-((1/b).^a))*mf;
```

```
plot(mf,x)
hold on;

% case 2: Af=0.01, combustor temp. rise :408K
a=0.25;
p3=4; % turbine inlet pressure (bar)
p4=1; % turbine exhaust pressure (bar)
b=4; %p3/p4
t3=785; % inlet temp (K)
nt=0.95; % isrntropic eff.
Cpg =1.147; %specific heat
mf = 0.1:0.01:0.4; % mass fuel rate (kg/s)
x= nt*Cpg*t3*(1-((1/b).^a))*mf;
plot(mf,x)
hold on;

% case 3: Af=0.01, combustor temp. rise :408K
a=0.25;
p3=4; % turbine inlet pressure (bar)
p4=1; % turbine exhaust pressure (bar)
b=4; %p3/p4
t3=855; % inlet temp (K)
nt=0.95; % isrntropic eff.
Cpg =1.147; %specific heat
mf = 0.1:0.01:0.4; % mass fuel rate
x= nt*Cpg*t3*(1-((1/b).^a))*mf;
plot(mf,x)
hold on;
```

Appendix C: Atmos Clock Components Measurements with Solidworks Models

Appendix C lists the Atmos clock gear train details with Solidworks models and photographs as presented in Figures C.1 to C.10 and Tables C.1 through C.8. The volume, surface area and moment of inertia about rotational axis for the components have been calculated using Solidworks. The materials used are brass or steel depending upon the component color.
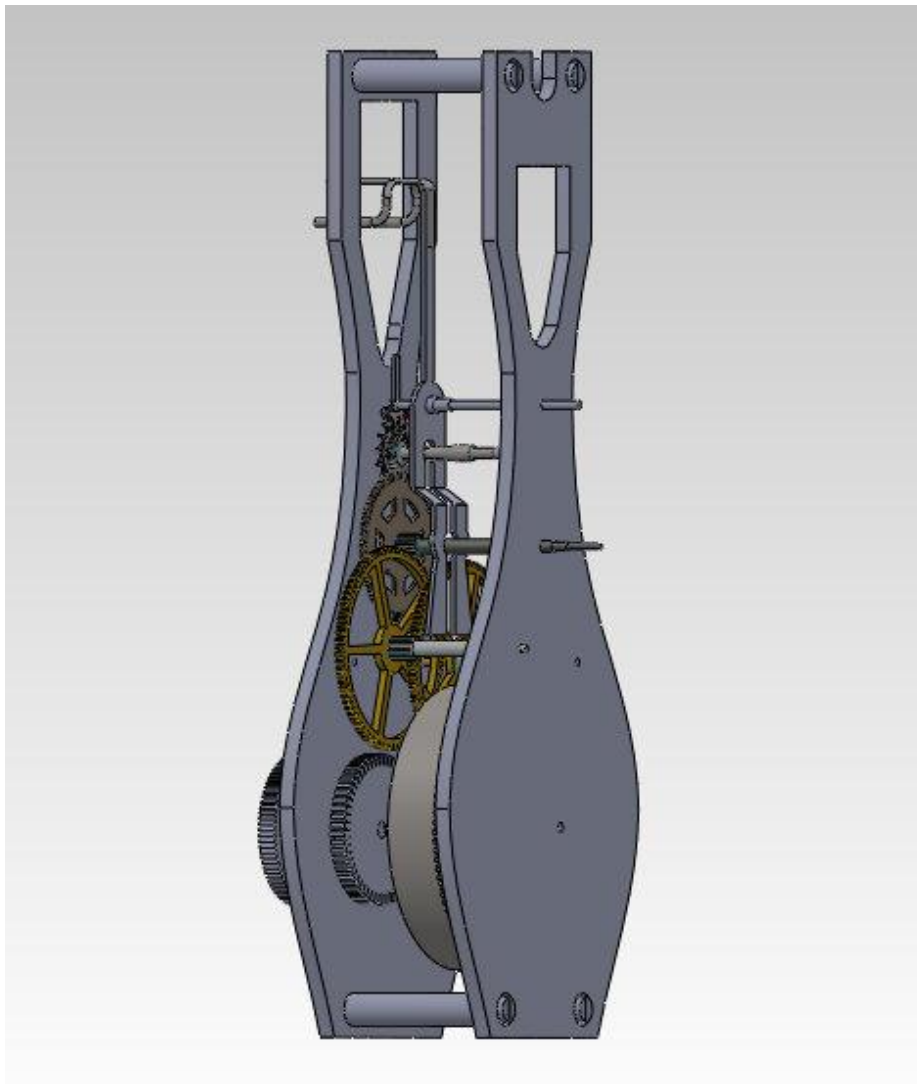
Figure C.1: Atmos clock gear train model created in Solidworks

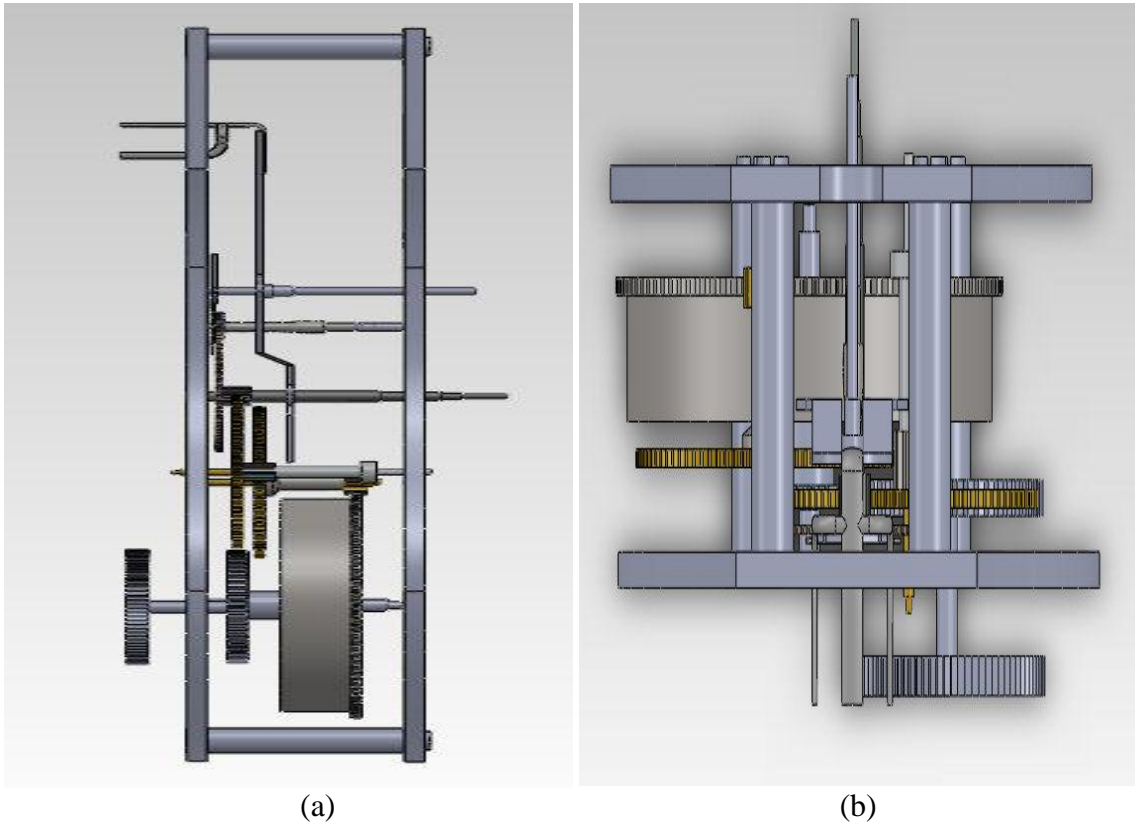(a)   (b)

Figure C.2: Atmos clock gear train model with (a) side, and (b) top views in Solidworks

Click wheel   Wheel, W_{02}

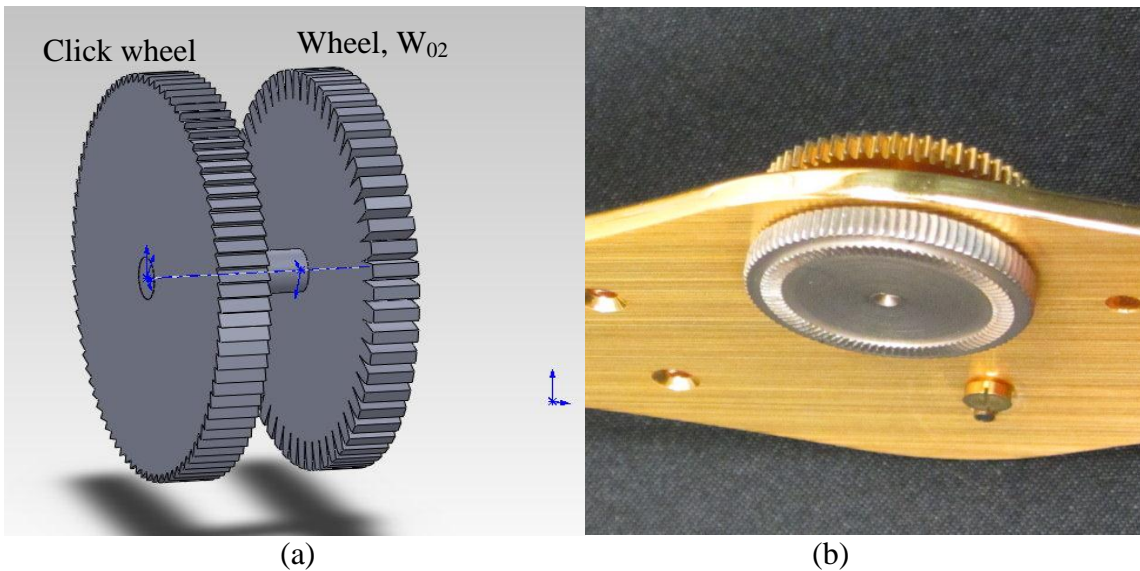(a)   (b)

Figure C.3: Click wheel, W_{01}, and wheel, W_{02}, assembly of the gear train with (a) Solidworks view, and (b) photograph of component mounted on plate

Table C.1: Click wheel, W_{01}, and wheel, W_{02}, assembly parameters

Description	Value	Units
Volume of assembly	1.10	cm^3
Mass of assembly	1.10	gm
Surface area of assembly	16.86	cm^2
Moment of inertia about rotational axis	0.43	$gm*cm^2$
Click wheel (W_{01}) diameter	18.9	Mm
Click wheel (W_{01}) thickness	2.2	Mm
Wheel (W_{02}) diameter	18.5	Mm
Wheel (W_{02}) thickness	2.0	Mm
Shaft diameter connecting wheels	1.96	Mm
Shaft length connecting wheels	9.75	Mm

(a)   (b)
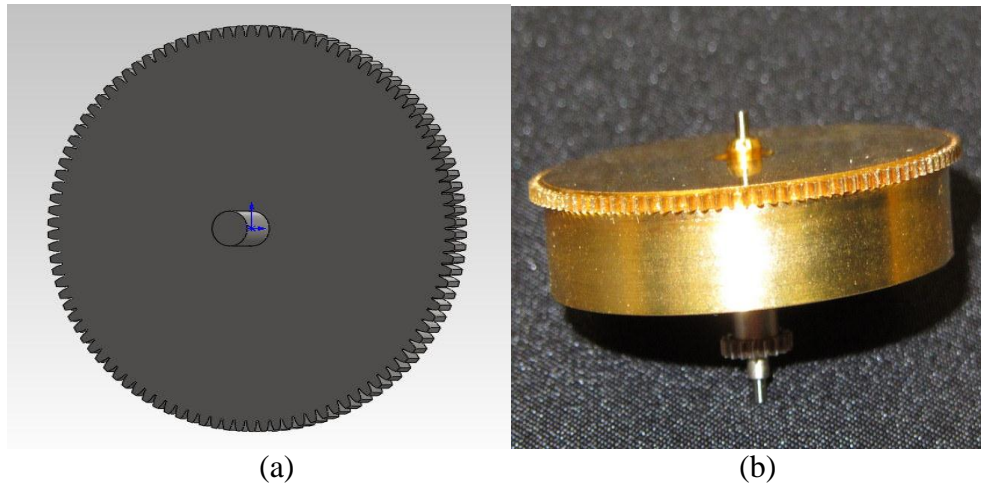
Figure C.4: Great wheel, W_{11}, of the gear train (a) Solidworks view, and (b) canister with attached ring and fitted with winding arbor driven by the click wheel assembly

Table C.2: Great wheel, W_{11}, parameters

Description	Value	Units
Volume of wheel	1.073	cm^3
Mass of wheel	7.83	gm
Surface area of wheel	23.90	cm^2
Moment of inertia about rotational axis	12.61	$gm*cm^2$
Diameter	37.03	mm
Thickness	1.02	mm

(a)   (b)

Figure C.5: Third wheel, W_{31}, and wheel, W_{32}, of the gear train with (a) Solidworks view, and (b) photograph of third wheel assembly

Table C.3: Third wheel, W_{31}, and wheel, W_{32}, parameters

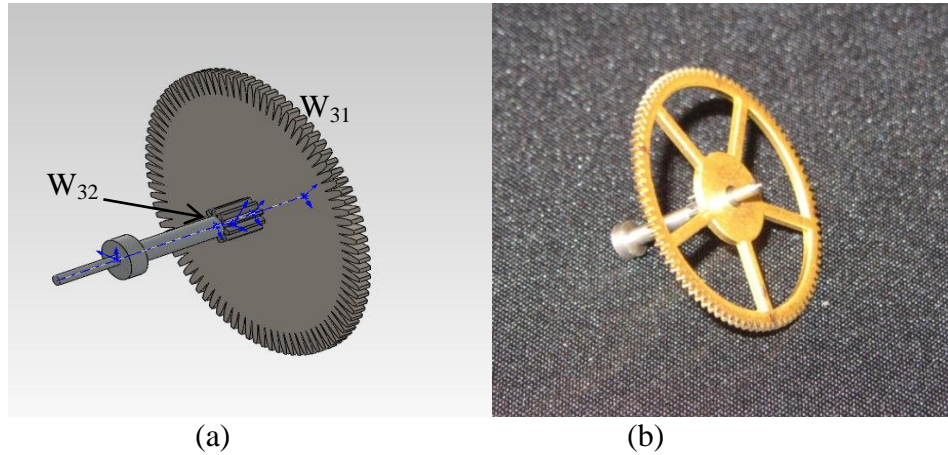| Description	Value	Units
Volume of assembly	0.51	cm^3
Mass of assembly	1.79	gm
Surface area of assembly	14.85	cm^2
Moment of inertia about rotational axis	1.08	$gm*cm^2$
Wheel (W_{31}) diameter	25.07	mm
Wheel (W_{31}) thickness	1.0	mm
Wheel (W_{32}) diameter	3.07	mm
Wheel (W_{32}) thickness	3.25	mm
Shaft diameter	1.75	mm
Shaft length	11.79	mm

(a)   (b)

Figure C.6: Second wheel, W_{21}, and wheel, W_{22}, of the gear train with (a) Solidworks view, and (b) photograph of second wheel assembly

Table C.4: Second wheel, W_{21}, and wheel, W_{22}, parameters

Description	Value	Units
Volume	0.23	cm^3
Mass	2.1	gm
Surface area	8.01	cm^2
Moment of inertia about rotational axis	1.14	gm*cm^2
Wheel (W_{21}) diameter	25.07	mm
Wheel (W_{21}) thickness	1.0	mm
Wheel (W_{22}) diameter	4.28	mm
Wheel (W_{22}) thickness	2.16	mm
Shaft diameter	2.42	mm
Shaft length	8.7	mm

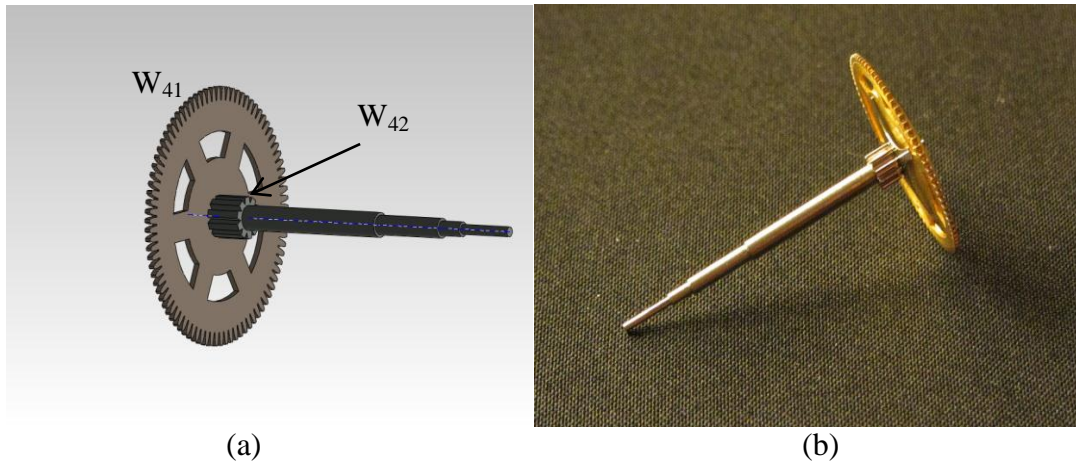(a)   (b)

Figure C.7: Fourth wheel, W_{41}, and wheel, W_{42}, of the gear train with (a) Solidworks view, and (b) photograph of the fourth wheel assembly

Table C.5: Fourth wheel, W_{41}, and wheel, W_{42}, parameters

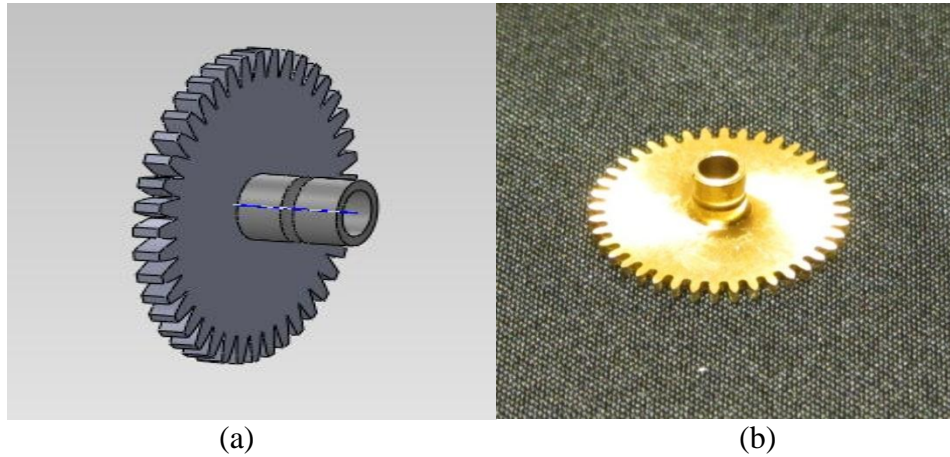| Description	Value	Units
Volume of assembly	0.16	cm^3
Mass of assembly	1.85	gm
Surface area of assembly	7.06	cm^2
Moment of inertia about rotational axis	0.84	gm*cm^2
Wheel (W_{41}) diameter	18.21	mm
Wheel (W_{41}) thickness	0.46	mm
Wheel (W_{42}) diameter	3.09	mm
Wheel (W_{42}) thickness	2.87	mm
Shaft diameter (max)	1.75	mm
Shaft length	25.31	mm

(a)   (b)

Figure C.8: Hour wheel, W_{43}, with canon of the gear train with (a) Solidworks view, and (b) photograph

Table C.6: Hour wheel, W_{43}, with canon parameters

Description	Value	Units
Volume of assembly	0.21	cm^3
Mass of assembly	1.77	gm
Surface area of assembly	6.20	cm^2
Moment of inertia about rotational axis	0.59	$gm*cm^2$
Wheel (W_{43}) diameter	16.75	mm
Wheel (W_{43}) thickness	1.0	mm
Canon outside diameter	3.49	mm
Canon inside diameter	2.4	mm
Canon length	3.9	mm

W_{52}

W_{51}

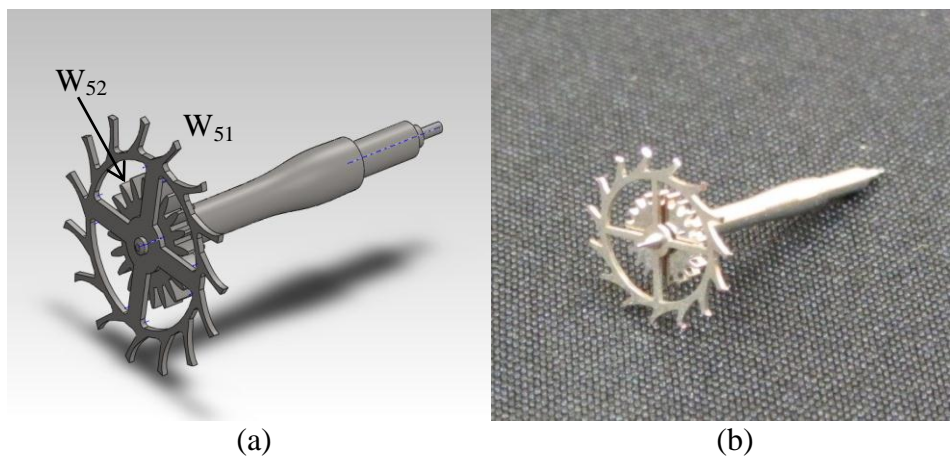(a)   (b)

Figure C.9: Escape wheel, W_{51}, and wheel, W_{52}, of the gear train with (a) Solidworks view, and (b) photograph of escape wheel assembly

Table C.7: Escape wheel, W_{51}, and wheel, W_{52}, parameters

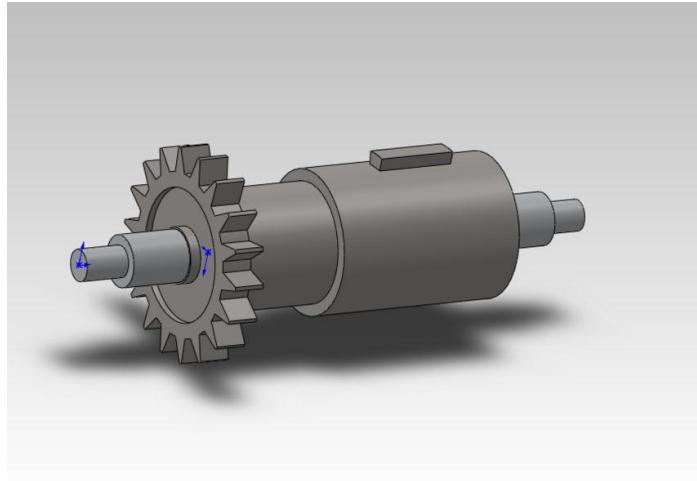| Description	Value	Units
Volume of assembly	0.004	cm^3
Mass of assembly	0.280	gm
Surface area of assembly	1.890	cm^2
Moment of inertia about rotational axis	0.060	$gm*cm^2$
Wheel (W_{51}) diameter	8.95	mm
Wheel (W_{51}) thickness	0.26	mm
Wheel (W_{52}) diameter	4.7	mm
Wheel (W_{52}) thickness	0.9	mm
Shaft diameter (max)	1.86	mm
Shaft length	14.39	mm

Figure C.10: Solidworks view of the great wheel winding stem of the gear train

Table C.8: Great wheel winding stem details

Description	Value	Units
Volume of assembly	0.21	cm^3
Mass of assembly	1.34	gm
Surface area of assembly	6.38	cm^2
Moment of inertia about rotational axis	0.06	$gm*cm^2$
Wheel (W_{12}) diameter	6.20	Mm
Wheel (W_{12}) thickness	1.0	Mm
Shaft diameter (max)	4.05	Mm
Shaft length	21.26	Mm

Appendix D: Atmos Clock Components Measurements with Calculated Spring Stiffnesses

The measured data for the various components of the Atmos clock are presented in Tables D.1 to D.13 with respective photographs in Figures D.1 to D.10

Figure D.1: Pallet with twin jeweled pallet and staff shown as photograph and solidworks model; rotational axis located about arbor 6

Table D.1: Pallet with twin jeweled pallet and staff measurements

Description	Value	Units
Volume of assembly	1.68	cm^3
Mass of assembly	0.7	gm
Surface area of assembly	9.22	cm^2
Moment of inertia about rotational axis	1.49	$gm*cm^2$
Total height	5.60	cm
Maximum width	1.14	cm
Maximum depth	1.40	cm
Weight	0.7	gm

Figure D.2: Idler pulley for chain mount photograph

Table D.2: Idler pulley for chain mount measurements

Description	Value	Units
Outside diameter	1.300	cm
Shaft diameter	0.094	cm
Pulley width	0.403	cm
Weight	3.500	gm
Arbor length	1.000	cm

Figure D.3: Atmos bellows photograph (top view) with US dime for size comparison

Table D.3: Bellows measurements listed to identify system parameters

Description	Value	Units
Outside diameter	11.3	cm
Inside diameter	8.7	cm
Height at room temperature	6.8	cm
Curved profile diameter for top surface	5.8	cm
Weight	204	gm

Figure D.4: Bellows spring photograph

Table D.4: Bellows spring measurements

Description	Value	Units
Outside diameter	7.11	cm
Inside diameter	6.04	cm
Wire diameter	0.59	cm
No. of turns	4	-
Axial length (uncompressed)	5.58	cm
Weight	138.60	gm

Table D.5: Bellows spring stiffness k_{ec}=16.6 kg/mm (162.79 N/mm) calculation data

Applied load (lbs)	Applied load (kg)	Displacement (mm)	Stiffness (kg/mm)
2	0.907	0.10	9.072
5	2.268	0.20	11.340
10	4.536	0.30	15.120
12	5.443	0.45	12.096
15	6.804	0.55	12.371
20	9.072	0.70	12.960
68	30.844	1.70	18.144

Figure D.5: Main torsional spring (inside barrel) photograph

Table D.6: Main torsional spring (inside barrel) measurements for a flat cross section

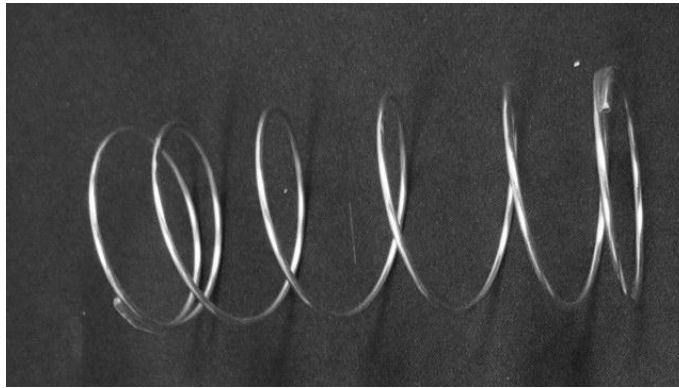| Description	Value	Units
Length (unwound)	115.6	cm
Width	0.597	cm
Thickness	0.008	cm
Weight	4.8	gm

Figure D.6: Coil spring (parallel to bellows spring) photograph

Table D.7: Coil spring (parallel to bellows spring) measurements

Description	Value	Units
Outside diameter	4.80	cm
Inside diameter	4.54	cm
Wire diameter	0.13	cm
No. of turns	7	-
Length (uncompressed)	7.93	cm
Weight	7.5	gm

Table D.8: Coil spring stiffness k_c=18.11gm/mm (0.178 N/mm) calculation data

Applied load (gm)	Displacement (mm)	Stiffness (gm/mm)
224.0	11.3	19.82
427.8	24.3	17.60
648.2	38.3	16.92

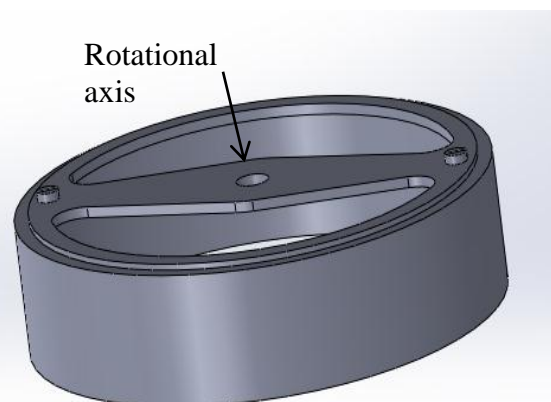

Figure D.7: Torsional pendulum photograph and Solidworks model; rotational axis is vertical

Table D.9: Torsional pendulum measurements

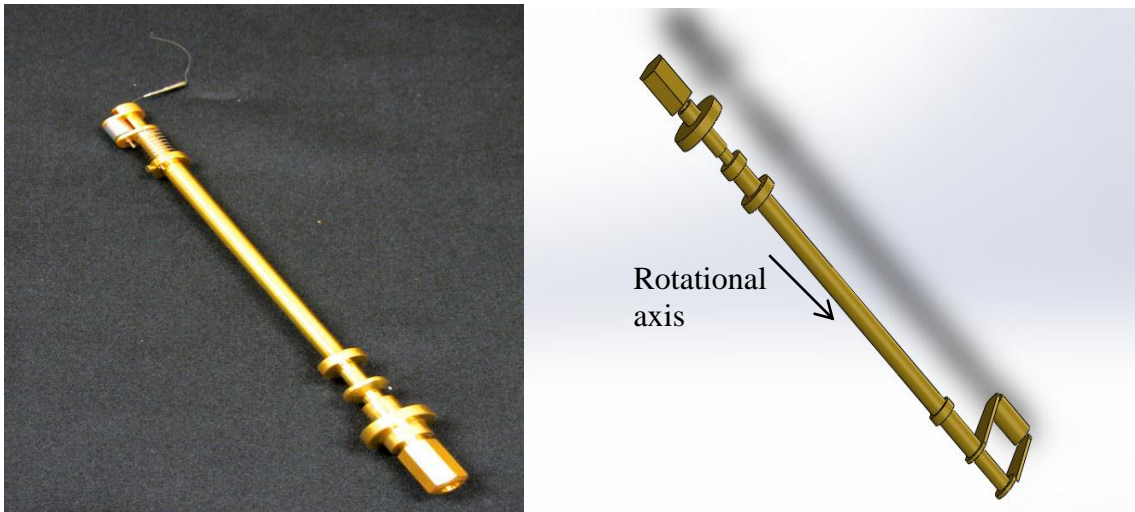| Description	Value	Units
Volume of assembly	22.13	cm^3
Mass of assembly	208.0	Gm
Surface area of assembly	182.6	cm^2
Moment of inertia about rotational axis	1675	gm*cm^2
Outside diameter	8.86	Cm
Inside diameter	7.81	Cm
Height	2.33	Cm
Weight	208.0	Gm
Cross bridge thickness	0.278	Cm
Cross bridge width (max)	2.19	Cm

Figure D.8: Torsional pendulum rod photograph and Solidworks model with rotational axis along length of pendulum rod

Table D.10: Torsional pendulum rod measurements

Description	Value	Units
Volume of assembly	4.38	cm^3
Mass of assembly	37.02	gm
Surface area of assembly	40.56	cm^2
Moment of inertia about rotational axis	921	gm*cm^2
Length	14.0	cm
Weight	28.9	gm
Diameter	0.50	cm

Figure D.9: Impulse roller photograph

Table D.11: Impulse roller measurements

Description	Value	Units
Diameter	0.564	cm
Height	0.575	cm

Figure D.10: Carrier pulley and chain with spring

Table D.12: Carrier pulley and chain measurements

Description	Value	Units
Outside diameter of pulley	1.397	cm
Width of pulley	0.480	cm
Chain length	8.000	cm
Total weight	8.500	gm

Table D.13: Carrier pulley spring measurements

Description	Value	Units
Wire diameter	0.034	cm
No. of turns	11	-

Appendix E: Experimental Data Collected for Bellows

The bellows displacement response to the temperature change with respect to time measured in controlled conditions is presented in Tables E.1 to E.3. The figures E.1 to E.3 characterize the bellows' motion.

The experimental conditions can be summarized as

E1. Ambient temperature $T_a = 72^0F$.

E2. Maximum height of bellows y = 7.44 mm with a thin metal tray on top.

E3. Weight of thin metal tray is $m_b = 0.227$ lbs (0.103kg).

Case E1: Bellows contraction from y = 7.0 mm due to temperature fall measured over 1 minute time period. No external loading was applied. The curve fit as shown in Figure. E.1 is represented as y= - 1E - $05x^2$ - 0.0384x + 0.7625, $R^2 = 0.9044$.

Table E.1: Bellows contraction data

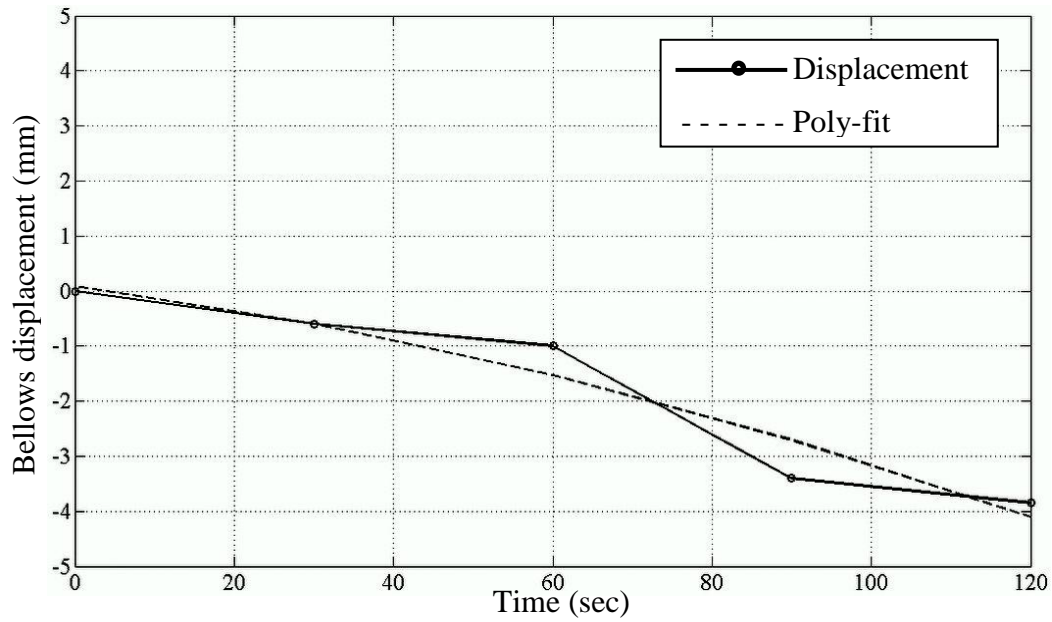| Time (sec)	y (mm)	dy (mm)
0	7.00	0.00
30	6.40	-0.60
60	5.00	-1.00
90	3.60	-3.40
120	3.15	-3.85

Figure E.1: Experimental bellows contraction vs. time characteristics showing displacement data and corresponding curve fit

Case E2: The bellows expansion with 5lbs (2.27kg) external weight was measured over 6 min time period. The weight of thin metal tray $m_b = 0.227$lbs (0.103kg) was additional. The curve fit as shown in Figure E.2 is represented as y= - 1E - 07x^3 - 9E - 05x^2 + 0.0303x + 2.6707, $R^2 = 0.9044$.

Table: E.2: Bellows expansion response measured over 6 minute time period

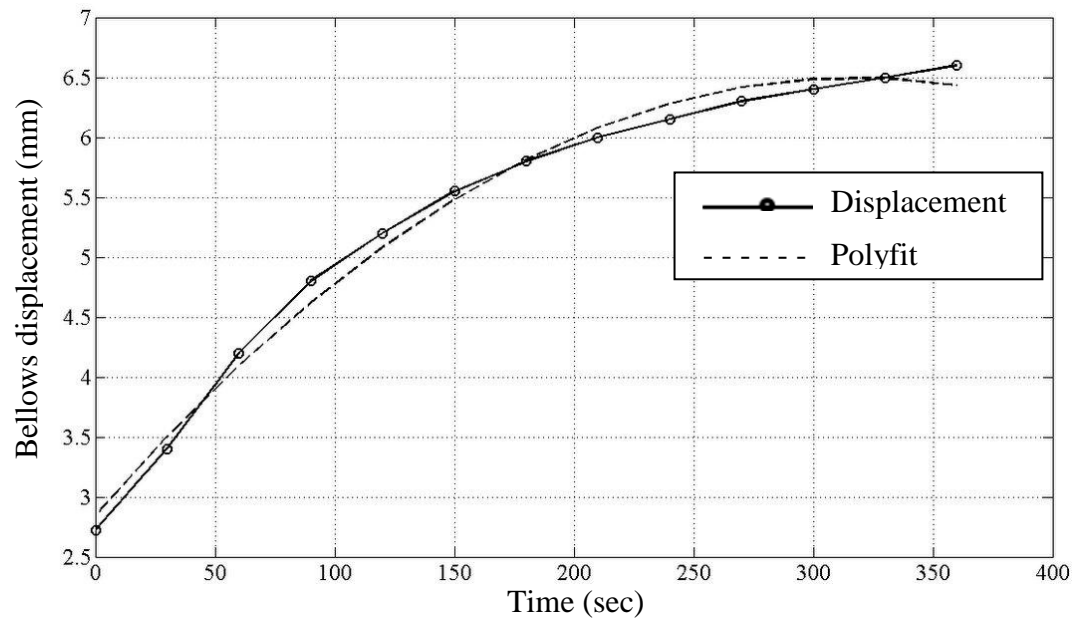| Time (sec)	y (mm)
0	2.72
30	3.40
60	4.20
90	4.80
120	5.20
150	5.55
180	5.80
210	6.00
240	6.15
270	6.30
300	6.40
330	6.50
360	6.60

Figure E.2: Experimental bellows expansion vs. time characteristics with external loading showing displacement data with corresponding curve fit

Case E3: The bellows expansion without any external loading was measured over 20 minute time period. Only thin metal tray weight m_b= 0.227lbs (0.103kg) was applied. The curve fit as shown in Figure E.3 is represented as y= - 2E - $14x^5$ - 7E - $11x^4$ + 1E-$07x^3$ – 8E-$05x^2$+0.0278x+2.4482, R^2 = 0.9904.

Table E.3: Bellows expansion response measured over a 20 minute time period

Time (sec)	y (mm)	Time (sec)	y (mm)
0	2.80	480	6.70
30	3.00	510	6.75
60	3.50	540	6.80
90	4.20	570	6.85
120	4.95	600	6.90
150	5.40	660	7.00
180	5.70	720	7.10
210	5.90	780	7.16
240	6.10	840	7.20
300	6.20	900	7.30
330	6.30	960	7.30
360	6.40	1020	7.32
390	6.50	1080	7.35
420	6.55	1140	7.37
450	6.60	1200	7.40
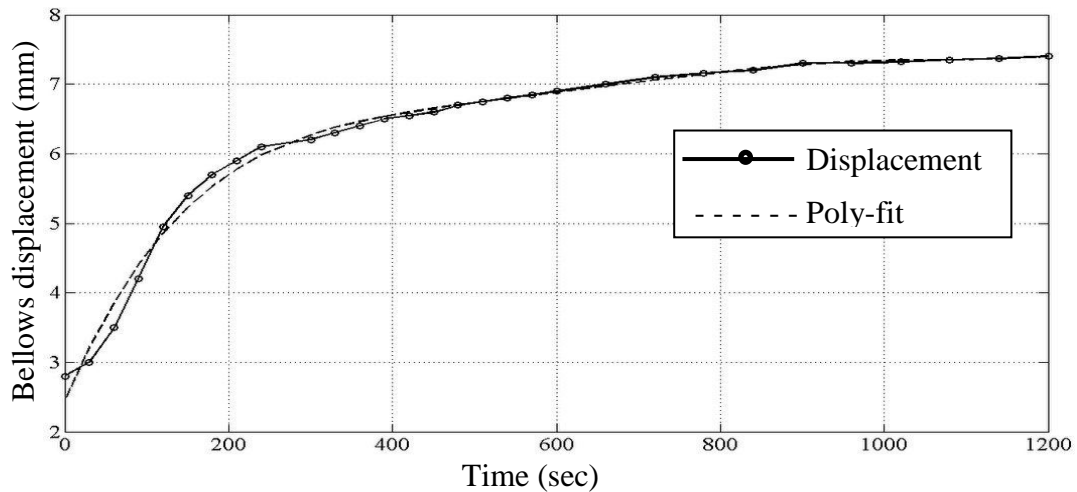
Figure E.3: Experimental bellows expansion vs. time characteristics without external loading showing displacement data with corresponding curve fit

Appendix F: Atmos Clock Simulink Models and Results

The Figures F.1 to F.11 present the Matlab/Simulink block diagrams with simulated and experimental results for the Atmos 540 clock.
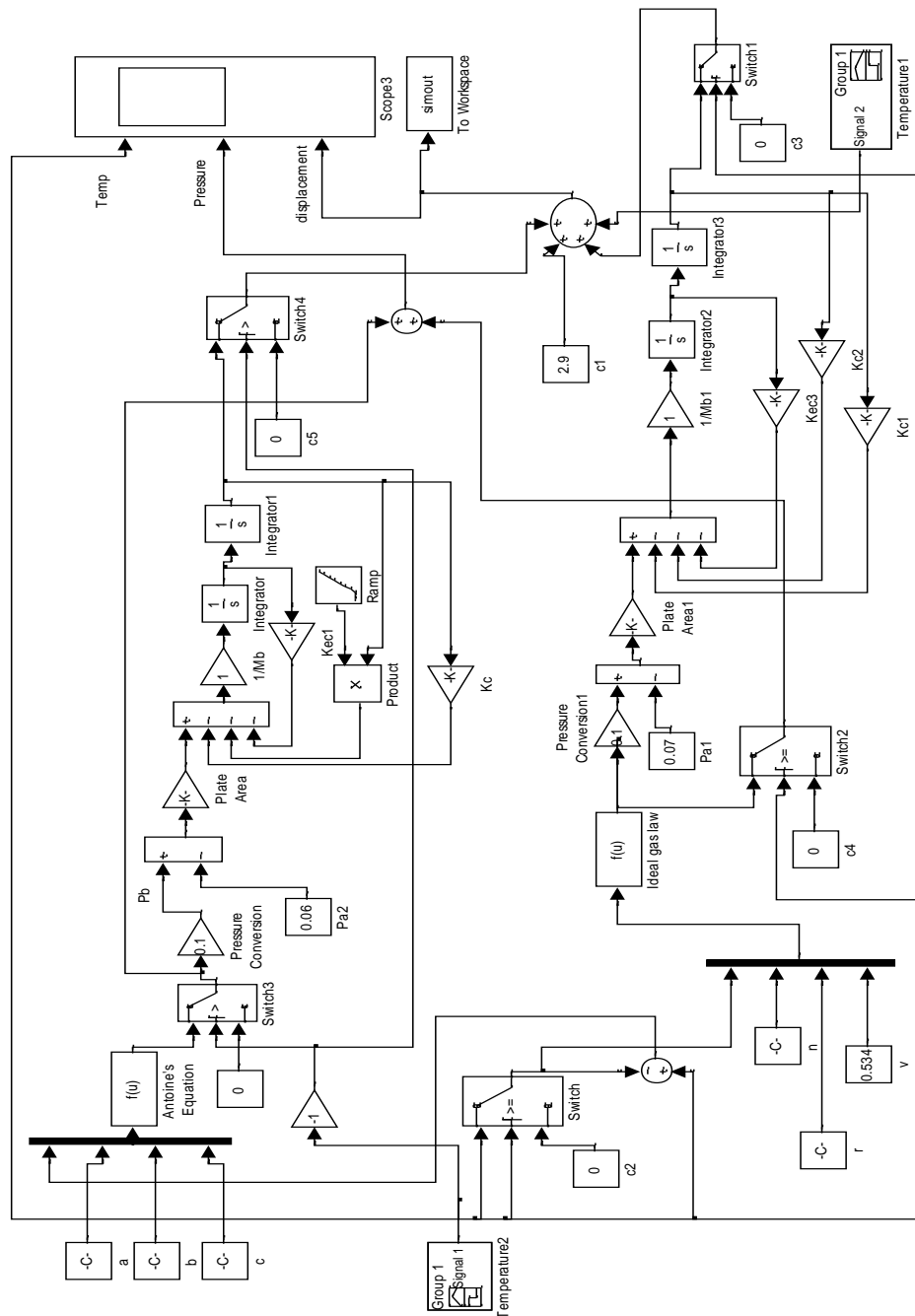

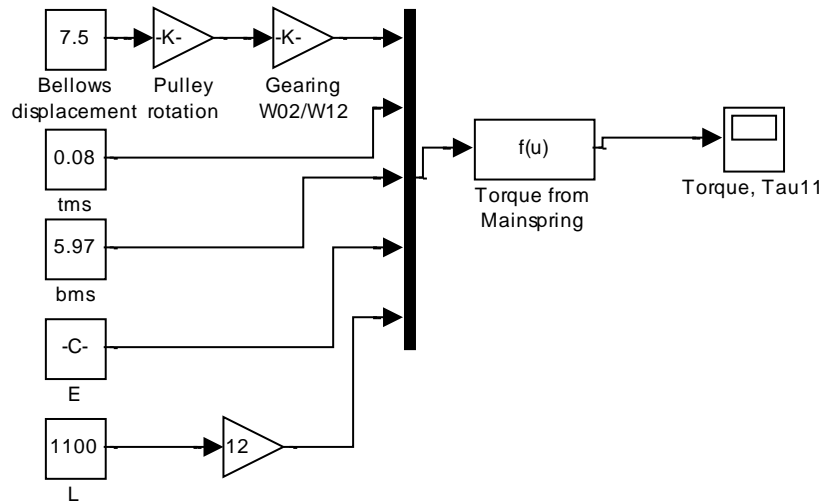Figure F.1: Simulation block diagram for Atmos clock bellows operation

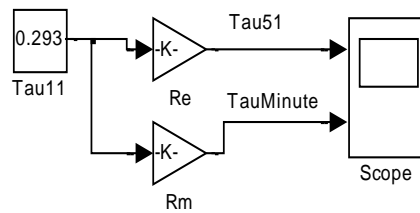Figure F.2: Mainspring energy storage and torque generation simulink model

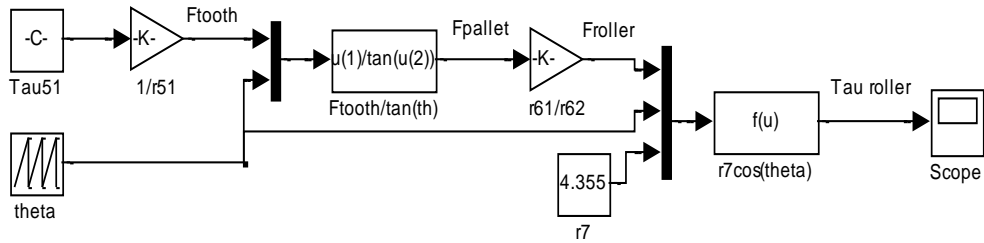Figure F.3: Motion works simulink model

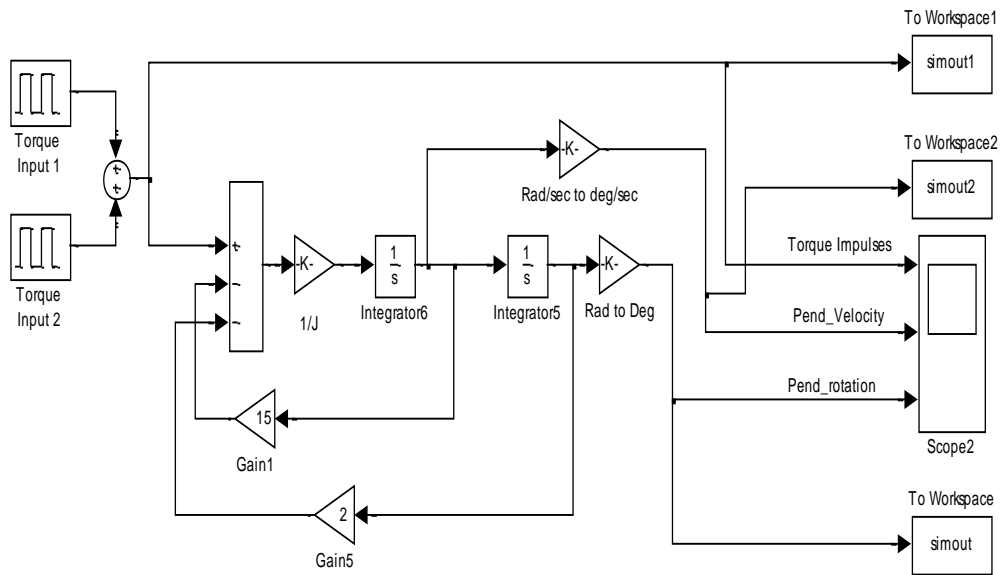Figure F.4: Escapement torque transmission simulink model

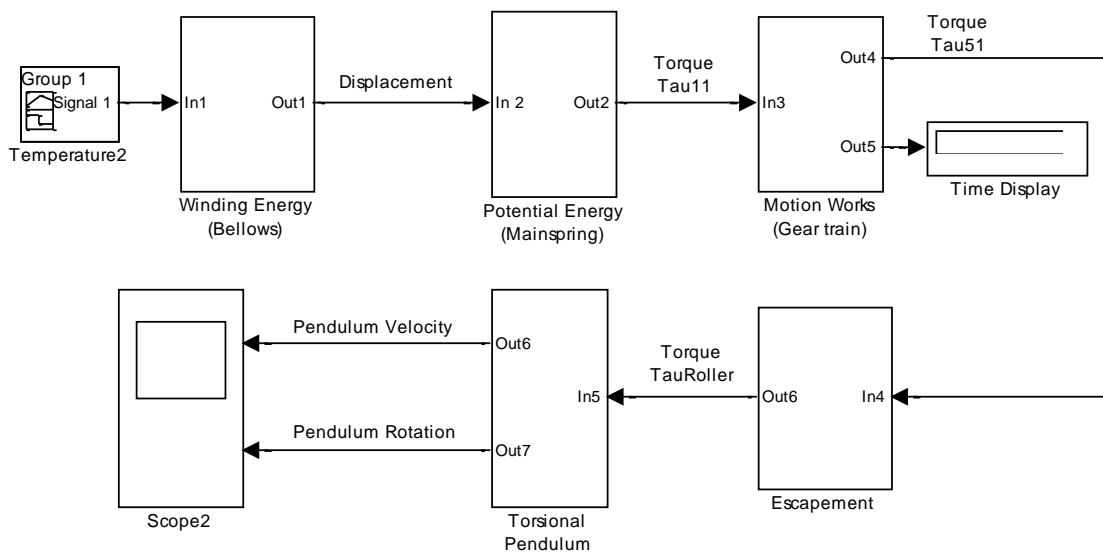Figure F.5: Torsional Pendulum dynamics simulink model

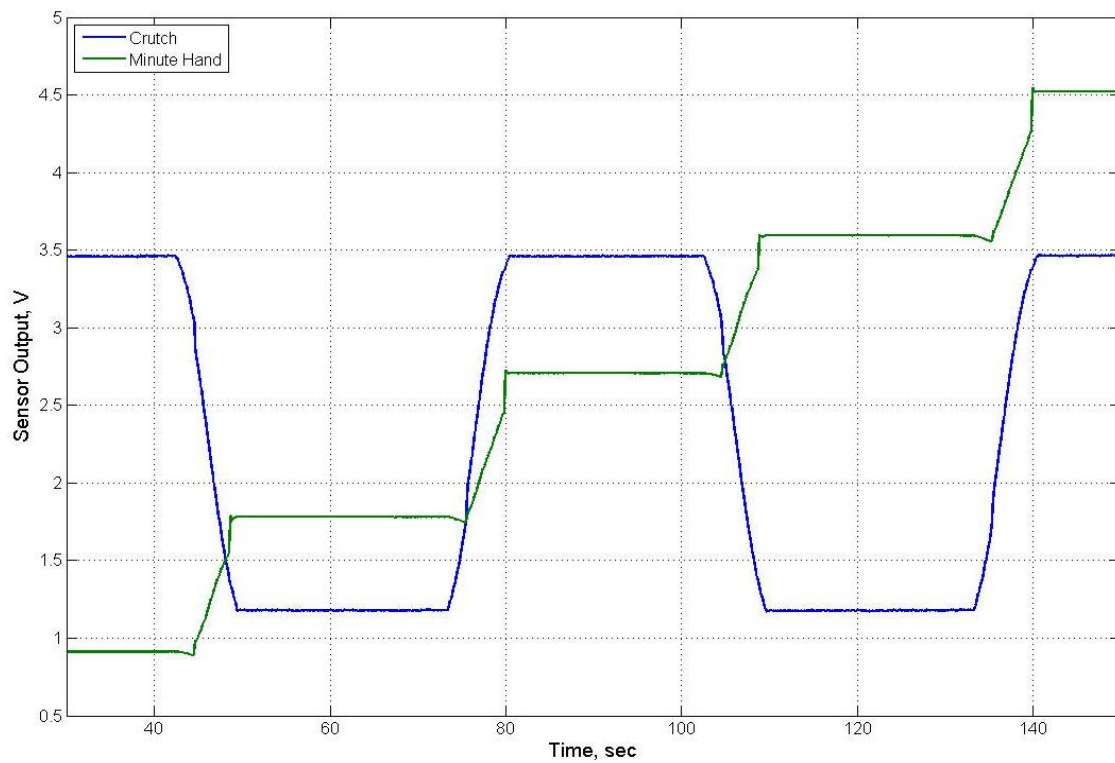Figure F.6: Simulink model for energy flow through Atmos 540 clock subsystems

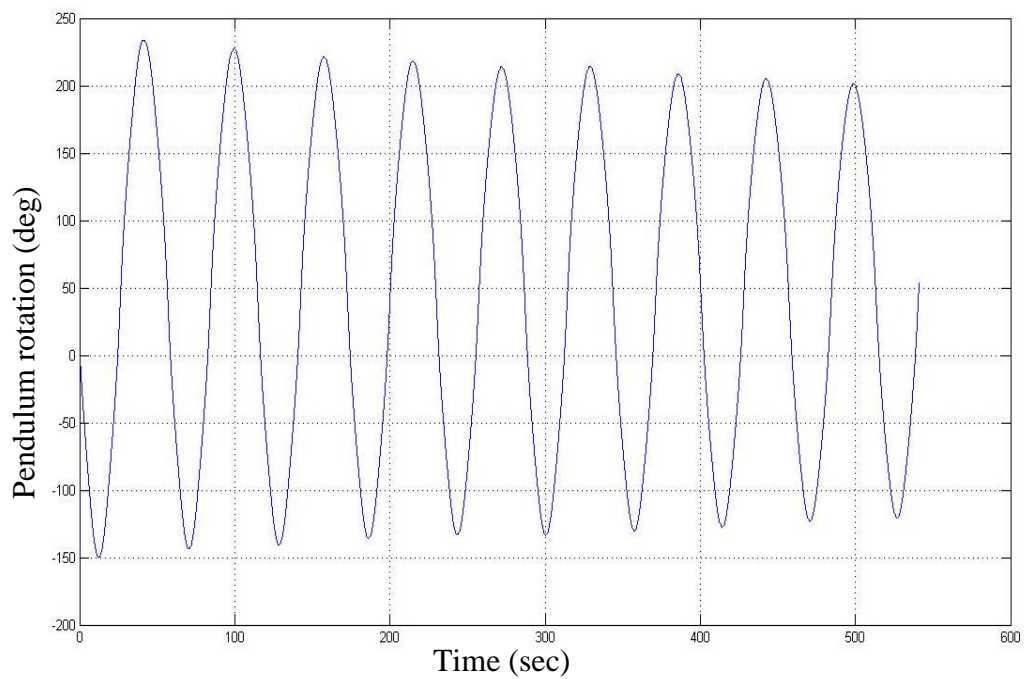Figure F.7: Experimental crutch and minute hand motion observed for two minutes time period

Figure F.8: Experimental torsional pendulum motion observed

99
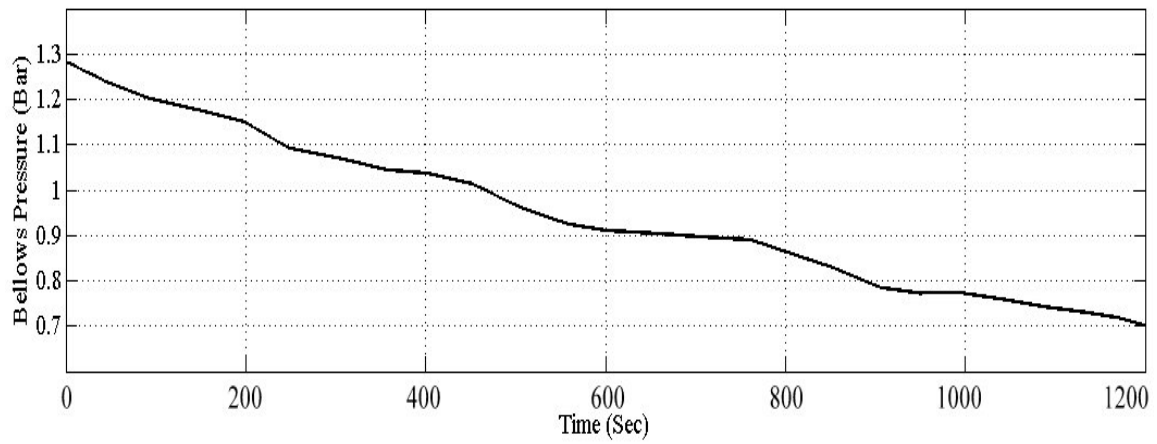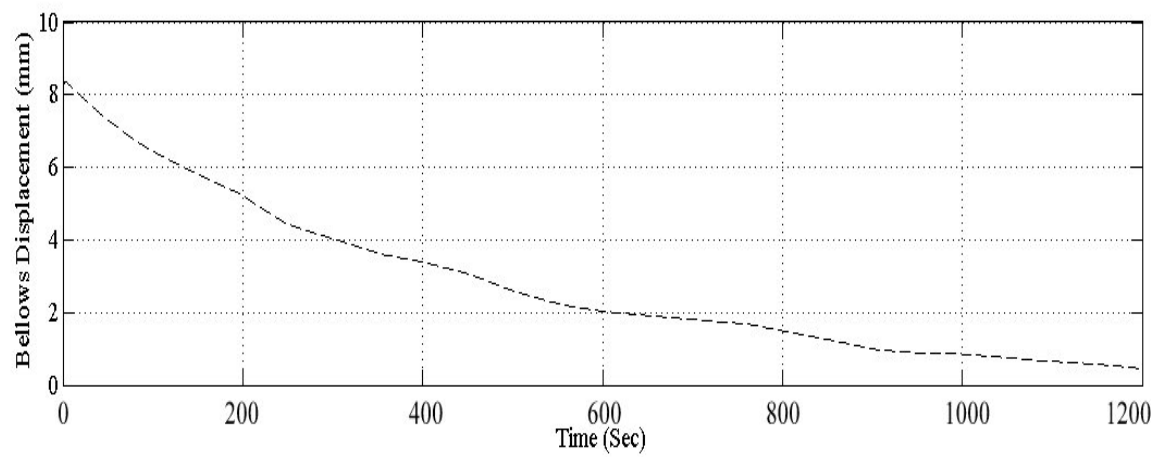
Figure F.9: Simulated bellows response for temperature range 295-283K over twenty minutes time period
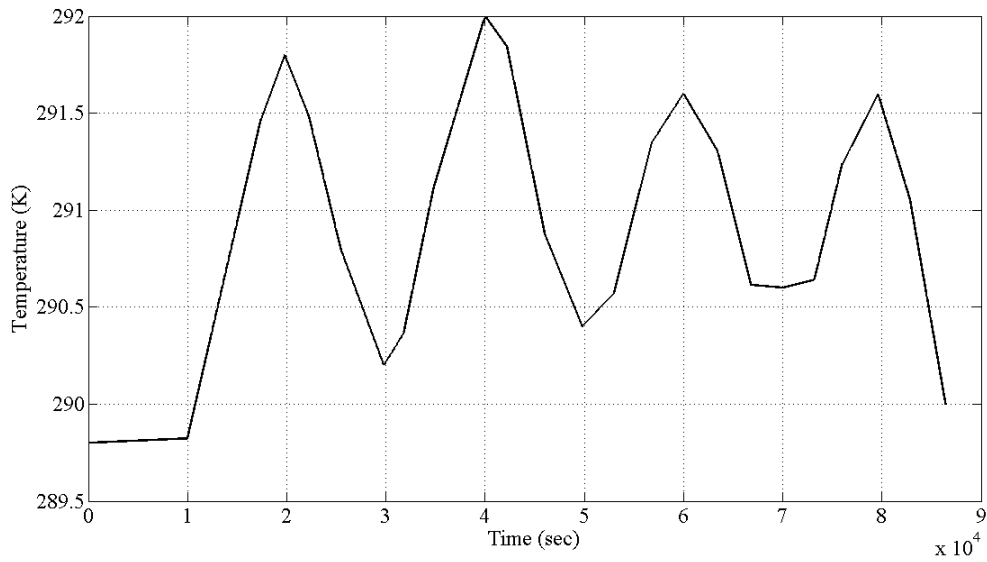
Figure F.10: Random temperature variations within 2°C provided over a 24 hour time period to observe bellows response
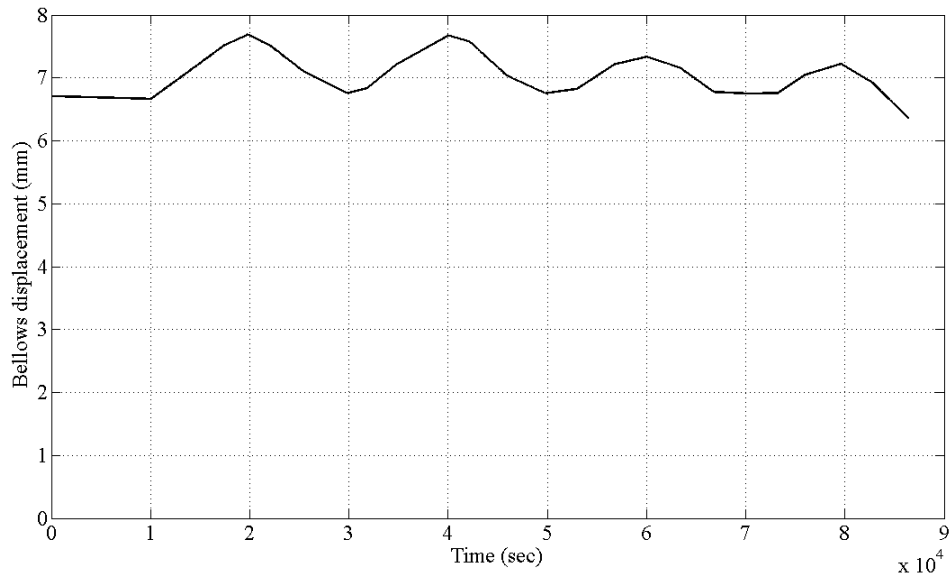
Figure F.11: Bellows displacement response simulated over a 24 hour period for temperature variations in a range of 2°C

The bellows responded with expected back and forth linear movement providing approximately 6mm of displacement for given temperature variations.

101

Appendix G: Atmos Clock Matlab Codes for Data Plotting

    Appendix G provides the Matlab codes with parameter values used for the Atmos

clock study as data plotting tools.

```
%%%%%%Code to generate Matlab plots for experimental data collected using
various sensors and LabVIEW for crutch, minute hand and pendulum motion%%%%%

dat=load('shreyas_1.lvm'); % data file was obtained from LabVIEW software
 t=dat(:,1);
 %figure(1)
% plot(t,dat(:,2:end)), figure(gcf), grid
  % X_Value pendulum_2 (Filtered)  crutch_motion (Filtered)   minute_hand (Filtered)
pendulum_1 (Filtered)   Comment
%legend pend_2 crutch minute pend_1
 pend_2=dat(:,2); % pendulum motion data from LabVIEW file
 crutch=dat(:,3); % crutch motion data from LabVIEW file
 minute=dat(:,4); % minute hand motion data from LabVIEW file
 pend_1=dat(:,5); % pendulum motion data from LabVIEW file


 pend_2=(pend_2-mean(pend_2))/(max(pend_2)-min(pend_2));
 pend_2=(pend_2-mean(pend_2))/((.347)-(-.512));
 pend_1=(pend_1-mean(pend_1))/(max(pend_1)-min(pend_1));
 pend_1=(pend_1-mean(pend_1))/((.3785)-(-.4085));
 pend=unwrap(atan2(pend_2,pend_1))/2*180/pi; % generates pendulum motion data
load shreyas_1.lvm
figure(2)
plot(t+20,pend-35,simout.time,simout.signals.values+20,'--'),grid
legend('Experimental Results','Simulated Results')
%figure(3)
% plot(t,minute-pend/50/500),grid
%plot(t,minute,t,pend/50),grid
figure(4)
subplot(2,1,1),plot(simout1.time,simout1.signals.values),grid
subplot(2,1,2),plot(simout2.time,simout2.signals.values),grid
```

%%%%% Code to plot experimental data collected for bellows linear motion%%%%%

```
%% case 1
t1=[0,30,60,90,120];  % time (sec)
dy1=[0,-0.6,-1,-3.4,-3.85];  %displacement (mm)
p1=polyfit(t1,dy1,2); % curve fit command
f1=polyval (p1,t1); % provides curve fit values
plot(t1,f1);
axis([0 120 -5 5])
hold on;
plot(t1,dy1) % data plotting for case 1

%% case 2
t2=[0,30,60,90,120,150,180,210,240,270,300,330,360]; %time
dy2=[2.72,3.4,4.2,4.8,5.2,5.55,5.8,6,6.15,6.3,6.4,6.5,6.6]; %displacement
p2=polyfit(t2,dy2,2); % curve fit command
f2=polyval (p2,t2); % provides curve fit values
figure(2),plot(t2,f2);
hold on;
figure(2),plot(t2,dy2) % data plotting for case 2

%% case 3
t3=[0,30,60,90,120,150,180,210,240,300,330,360,390,420,450,480,510,540,570,600,660,
720,780,840,900,960,1020,1080,1140,1200]; %time
dy3=[2.8,3,3.5,4.2,4.95,5.4,5.7,5.9,6.1,6.2,6.3,6.4,6.5,6.55,6.6,6.7,6.75,6.8,6.85,6.9,7,7.1,
7.16,7.2,7.3,7.3,7.32,7.35,7.37,7.4]; %displacement
p3=polyfit(t3,dy3,5); % curve fit command
f3=polyval (p3,t3); % provides curve fit values
figure(3),plot(t3,f3);
hold on;
figure(3),plot(t3,dy3) % data plotting for case 3
```

%%%%% Matlab code for Pressure variation of Ethyl chloride due to ambiant temperature change %%%%%%

```
a=4.16181; %equation parameter
b=1052.821; % equation parameter
c=-32.078; %equation parameter
n=0.014; %no. of moles
R=8.31; %gas constant (J/mol*K)
V=0.275; % volume of bellows
T=[220:.1:323]; %temperature range (K)
T1=[220:0.1:290] %temperature range (K)
T2=[290.1:0.1:323] %temperature range (K)

P =100.*[10.^(a-(b./(T1+c))) n*R*T2./V ] % Antoine's equation
 figure(1),plot(T,P,'black'),grid
 figure(2),semilogy(T,P,'black'),grid
```

REFERENCES

Ackermann, T., Andersson, T., and Soder, L., "Distributed Generation: A Definition", *Journal of Electrical Power Systems Research,* vol. 57, no. 3, pp. 195-204, April 2001.

Ailer, P., Sánta, I., Szederkenyi, G., and Hangos, K., "Nonlinear Model-Building of a Low-Power Gas Turbine", *Journal of Periodica, Politechnica, Ser. Transport Engineering,* vol. 29, no. 1-2, pp. 117-135, 2001.

Al-Hamdan, Q. and Ebaid, M., " Modeling and Simulation of a Gas Turbine Engine for Power Generation", *Journal of Engineering for Gas Turbine and Power*, vol. 128, no. 2, pp. 302-311, 2006.

Al-Qattan, M., Al-Juwayhel, F., Ball, A., Elhaj, M., and Gu, F., "Instantaneous Angular Speed and Power for the Diagnosis of Single-stage, Double-acting Reciprocating Compressor*", Institution of Mechanical Engineers, Part J: Journal of Engineering Tribology*, vol. 223, no. 1, pp. 95-114, 2009.

Armand, M. and Tarascon, J., "Building Better Batteries", *Journal of Nature*, vol. 451, no. 7179, pp. 652-657, February 2008.

Armannsson, H., Fridriksson, T., and Kristjansson, B., "CO_2 Emissions from Geothermal Power Plants and Natural Geothermal Activity", *Journal of Geothermics,* vol. 34, no. 3, pp. 286-296, 2005.

Azab, M., "Improved Circuit Model of Photovoltaic Array", *International Journal of Electrical Power and Energy Systems Engineering*, vol. 2, no. 3, pp. 185-188, 2009.

Barnham, K., Mazzer, M., and Clive, B., "Resolving the Energy Crisis: Nuclear or Photovoltaics?", *Journal of Nature Materials,* vol. 5, no. 3, pp. 161-164, March 2006.

Bueno, C. and Carta, J., "Wind Powered Pumped Hydro Storage Systems, A Means of Increasing the Penetration of Renewable Energy in the Canary Islands", vol. 10, no. 4, pp. 312-340, August 2006.

Burke, J. and Ornstein, R., "The Axemaker's Gift", Tarcher/Penguin: New York, NY, 1997.

Callaway, E., "Wireless Sensor Networks – Architecture and Protocols", Auerbach Publications: Boca Raton, FL, 2004.

Carrette, L., Friedrich, K., and Stimming, U., "Fuel Cells: Principles, Types, Fuels, and Applications", *Journal of Chemphyschem*, vol. 1, no. 4, pp. 162-193, December 2000.

Cavallo, A., "Controllable and Affordable Utility-Scale Electricity from Intermittent Wind Resources and Compressed Air Energy Storage", *Journal of Energy,* vol. 32, no. 2, pp. 120-127, February 2007.

Chevron, http://www.chron.com/business/article/Chevron-works-with-Calif-jail-on-microgrid-3428306.php#photo-2727391, accessed 2012.

Cohen, H., Rogers, G., and Saravanamuttoo, H., "Gas Turbine Theory", 4th Edition, Longman House: Essex, 1996.

Elhaj, M., Gu, F., Ball, A., Albarbar A., Al-Qattan M., and Naid A., "Numerical Simulation and Experimental Study of a Two-stage Reciprocating Compressor for Condition Monitoring", *Journal of Mechanical Systems and Signal Processing*, vol. 22, no. 2, pp. 374-389, 2008.

El-Khattam, W. and Salama, M., "Distributed Generation Technologies, Definitions, Benefits", *Journal of Electric Power Systems Research,* vol. 71, no. 2, pp. 119-128, October 2004.

Facilities, http://www.clemson.edu/facilities/energy-awareness/consumption.html, accessed August 2012.

Fatspaniel, http://view2.fatspaniel.net/SunDance/clemson/HostedEndUserView.html?&eid=66624, accessed March 2012.

Friedrichs, J., "Global Energy Crunch: How Different Parts of the World Would React to a Peak Oil Scenario", *Journal of Energy Policy,* vol. 38, no. 8, pp. 4562-4569, August 2010.

Fritz, M., "Reverso – The Living Legend", Braus: Berlin, Germany, 1992.

Gordon, J., and Giauque, W., "The Entropy of Ethyl Chloride. Heat Capacity from 13 to 287K. Vapor Pressure. Heats of Fusion and Vaporization", *Journal of the American Chemical Society*, vol. 70, no. 4, pp. 1506-1510, April 1948.

Ibrahim, H., Ilinca, A., and Perron, J., "Energy Storage Systems – Characteristics and Comparisons", *Journal of Renewable & Sustainable Energy Reviews*, vol. 12, no. 5, pp. 1221-1250, June 2008.

Jaeger Le Coultre, "Atmos 540 Repair Guide", Jaeger Le Coultre: Le Sentier, Switzerland, April 1993.

Lasseter, R., and Paigi, P., "Microgrid: A Conceptual Solution", Proceedings of 35th Annual IEEE Power Electronics Specialists Conference, Aachen, Germany, vol. 6, pp. 4285-4290, 2004.

Lebet, J., "Living on Air: History of the Atmos Clock", Jaeger Le Coultre: Le Sentier, Switzerland, 1997.

Lepschy, A., Mian, G., and Viaro, U., "Feedback Control in Ancient Water and Mechanical Clocks", *IEEE Transactions of Education*, vol. 35, no. 1, pp. 3-10, February 1992.

Martt, E., "The Atmos Clock Ethyl Chloride as the Bellows Gas", National Association of Watch and Clock Collectors, Horological Science Chapter #161, Horological Science Newsletter, Issue 3, pp. 16, May 1998.

Moline, D., Wagner, J., and Volk, E., "Model of a Mechanical Clock Escapement", *American Journal of Physics,* vol. 80, no. 7, pp. 599-606, July 2012.

Moon, F., and Stiefel, P., "Coexisting Chaotic and Periodic Dynamics in Clock Escapements", *Journal of Philosophical Transactions of the Royal Society A Mathematical, Physical and Engineering Sciences*, vol. 364, no. 1846, pp. 2539-2564, September 2006.

NIST Chemistry, National Institute of Standards and Technology Web Book – NIST Standard Reference Database Number 69, Accessed April 2012. (http://webbook.nist.gov/cgi/cbook.cgi?ID=C75003&Units=SI&Mask=1EFF)

Norton, R. "Machine Design – An Integrated Approach", Prentice Hall: Upper Saddle River, NJ, 2000.

Ogata, K., "System Dynamics", 4th Edition, Pearson Prentice Hall: Upper Saddle River, NJ, 2004.

Paradiso, J., and Starner, T., "Energy Scavenging for Mobile and Wireless Electronics", *IEEE Journal of Pervasive Computing,* vol. 4, no. 1, pp. 18-27, March 2005.

Pepermans, G., Driesen, J., Haeseldonckx, D., Belmans, R., and D'haeseleer, W., "Distributed Generation: Definition, Benefits and Issues", *Journal of Energy Policy,* vol. 33, no. 6, pp. 787-798, 2005.

Rahman, M., Ibrahim, T., and Abdalla, A., "Thermodynamic Performance Analysis of Gas-Turbine Power-Plant", *International Journal of the Physical Sciences*, vol. 6, no. 14, pp.3539-3550, July 2011.

Sekhon, R., Bassily, H., Wagner J., and Gaddis J., "Stationary Gas Turbines – A Real Time Dynamic Model with Experimental Validation", Proceedings of the American Control Conference, pp. 1838-1844, Minneapolis, MN, 2006.

Shively, D., Gardner, J., Haynes, T., and Ferguson, J., "Energy Storage Methods for Renewable Energy Integration and Grid Support", Energy 2030 conference, IEEE, pp. 1-6, Atlanta, GA, 2008.

Solar Group, http://www.my-solar.net/aboutus.htm, accessed August, 2012.

Suryanarayanan, S., Mancilla-David, F., Mitra, J., and Li, Y., "Achieving the Smart Grid Through Customer-Driven Microgrids Supported by Energy Storage", IEEE, International Conference on Industrial Technology, pp. 884-890, Viña del Mar – Valparaiso, Chile, March 2010.

Tsai, F., Tu, C., and Su, Y., "Development of Generalized Photovoltaic Model Using MATLAB/SIMULINK", Proceedings of the World Congress on Engineering and Computer Science, pp. 846-854, San Francisco, October 2008.

Vacheron, M., Constantin, M., and Pierson, J., "How to Repair Atmos: The Perpetual Motion Clock", Le Coultre Watches, Incorporated, Clockworks Press: Sacramento, CA, 2000.

Venkatesan, J., Nagarajan, G., Seeniraj, R., and Kumar, S., "Mathematical Modeling of Water Cooled Automotive Air Compressor", *International Journal of Engineering and Technology,* vol. 1, no. 1, pp. 1793-8236, April 2009.

Von Loessl, F., "Horloges a Remontage Automatique Par Les Influences Atmospheriques (Clocks with Automatic Winding by Atmospheric Influences*)", Journal Suisse d'Horlogerie*, pp. 45-47, February 1928.

Wylen, G., Sonntag, R., and Borgnakke, C., "Fundamentals of Classical Thermodynamics", Wiley & Sons: New York, 1978.